

**LEAKAGE PERFORMANCE EVALUATION OF CLOTH SEAL**

**by**

**ERDEM GÖRGÜN**

**Submitted to the Graduate School of Engineering and Natural Sciences**

**in partial fulfillment of**

**the requirements for the degree of**

**Doctor of Philosophy**

**SABANCI UNIVERSITY**

**December 2020**

**LEAKAGE PERFORMANCE EVALUATION OF CLOTH SEAL**

APPROVED BY:

[Blank lines for signature]

DATE OF APPROVAL:

© Erdem Görgün 2020  
All Rights Reserved

# **LEAKAGE PERFORMANCE EVALUATION OF CLOTH SEAL**

Erdem Görgün

Mechatronic Engineering, Ph.D. Dissertation, 2020

Thesis Advisor: Prof. Mahmut Faruk AKŞİT

Keywords: Cloth Seal, Cloth Seal Leakage Performance, Cloth Weave, Static Seal, Cloth Seal CFD Analysis, Box-Behnken Design, Gas Turbine Efficiency, Porous Medium Approach

## **ABSTRACT**

Turbomachinery sealing technology is concerned with the crucial tasks of maintaining pressurized regions, leakage control, cooling control, purge flow, and axial force balance. Thus, advances in sealing technology have considerable impact on overall turbomachinery performance, decreasing operational costs, fuel consumption, and NO<sub>x</sub> emissions. Cloth seals as a new stationary seal have been used as an alternative to thick metal shim seals to reduce leakage rate and increase wear life. The cloth seal includes one or more metallic-cloth fibers (cloth weave) and a thin metal shim.

Measuring actual cloth seal leakage proves difficult with challenging turbine operating conditions. Modeling the flow through the complex weave voids among each warp and shute fiber involves a very complex flow structure, extensive effort, and high CPU time. Therefore, a bulk porous medium flow model with flow resistance coefficients is applied to the model cloth seal weave fibers. CFD analyses need leakage data depending on the pressure load to calibrate flow resistance coefficients. A test rig is built to measure leakage of cloth weave with respect to the pressure load and weave orientation in four directions. The Sutherland-ideal gas approach is utilized to determine the flow resistance coefficients for Dutch twill

metallic-cloth fibers as a function of pressure load. Moreover, equations to calculate the porosity of plain and twill weave are developed and compared with available data.

Literature reviews indicate that available published data about cloth seal leakage performance are not adequately detailed to derive a closed-form equation defining the relationship between seal design parameters and cloth seal leakage performance. In an effort to fill this gap, the effect of geometric parameters under varying pressure load on the cloth seal leakage performance has been investigated in this study. In order to reduce the number of parameters to a manageable size, some of the parameters are fixed and excluded from the experimental design based on the studies in the literature. The remaining eight parameters are included in the screening experiments. Their levels are determined to cover typical application ranges. Parameters, which have a major impact on leakage rate, are determined in the screening experiments, and analyzed in the main experiments. A closed-form equation is derived based on the data and presented in this study. Leakage rate trends with respect to levels of each parameter are examined. In order to conduct leakage tests of screening and main experiment designs, several cloth seal designs are manufactured, and another custom test rig has been designed.

# ÖRGÜ KEÇELERİN SIZDIRMAZLIK PERFORMANSININ İNCELENMESİ

Erdem Görgün

Mekatronik Mühendisliği, Doktora Tezi, 2020

Tez Danışmanı: Prof. Dr. Mahmut F. AKŞİT

Anahtar kelimeler: Örgü Keçe, Örgü Keçe Sızdırmazlık Performansı, Örgü Metal, Statik Keçe, Örgü Keçe HAD Analizi, Box-Behnken Tasarımı, Gaz Türbin Verimliliği, Gözenekli Ortam Yaklaşımı

## ÖZET

Turbomakinalarda sızdırmazlık teknolojileri basınçlı alanların korunması, sızdırmazlık ve soğutma kontrolü ve aksenal kuvvetlerin dengelenmesi ile ilişkilidir. Bu sebeple sızdırmazlık teknolojisindeki gelişmeler toplam turbomakina verimliliği, operasyonel giderler, yakıt tüketimi ve NO<sub>x</sub> emisyonu açısından oldukça önemlidir. Örgü keçeler sızdırmazlık performansını iyileştirmek ve aşınma ömrünü uzatmak amacıyla geleneksel katı dolgu keçelere yeni bir alternatif olarak kullanılmaktadır. Örgü keçeler bir veya birden fazla metalik örgü katmanı ile ince bir metal dolgudan oluşmaktadır.

Çok yüksek sıcaklık ve basınç sebebiyle türbin çalışma koşullarında örgü keçenin sızdırmazlık performansının incelenmesi oldukça zordur. Fiberler arasından geçen akış oldukça kompleks bir yapıya sahiptir. Bu sebeple bu akışın modellenmesi için aşırı uğraş ve çok yüksek CPU zamanı gerekmektedir. Fiberler arasındaki akışın modellenmesi için gözenekli ortam akış modeli ve bu modelde tanımlanan akış direnç katsayıları kullanılmıştır. Bu modeldeki akış direnç katsayılarının farklı basınç yükü altında Hesaplamalı Akışkanlar Dinamiği (HAD) analizlerinde korelasyonunun

sağlanması gerekmektedir. Bu sebeple farklı basınç yükü altında ve farklı örgü yönlerinde fiberler arasındaki debi miktarının incelenmesi için bir test sistemi inşa edilmiştir. Dutch twill örgü tipindeki fiberlerin akış direnç katsayılarının farklı basınç yükleri altında belirlenmesi için Sutherland-ideal gaz yaklaşımı oluşturulmuştur. Ayrıca farklı örgü çeşitleri üzerinde gözenekliliği hesaplayan denklemler bulunmuştur.

Hali hazırda bulunan veriler tasarım parametreleri ile sızdırmazlık performansı arasında bir kapalı-form denklem elde edilmesi için yeterli olmamaktadır. Bu eksikliğin giderilmesi amacıyla bu çalışmada geometrik parametrelerin değişken basınç yükü altında statik keçe sızdırmazlık performansı üzerindeki etkisi araştırılmıştır. Parametre sayısının inceleme yapılabilecek uygun seviyeye azaltılması için çeşitli parametreler literatürdeki çalışmalar göz önünde bulundurularak sabitlenmiştir. İncelenmek için seçilen sekiz parametre tarama deney tasarımına dahil edilmiştir. Parametrelerin seviye aralıkları tipik uygulama aralıklarına göre seçilmiştir. Sızdırmazlık üzerinde önemli etkisi olan parametreler tarama deney tasarımında belirlenmiş ve bu parametreler ana deney tasarımında analiz edilmiştir. Deneyler sonucunda bir kapalı-form denklem elde edilmiştir. Parametre seviyelerine göre sızdırmazlık miktarındaki değişimler ortaya çıkarılmıştır. Tarama ve ana deney tasarımlarının gerçekleştirilmesi için ayrıca bir test düzeneği tasarlanmış ve birçok örgü keçe tasarımı üretilmiştir.

## ACKNOWLEDGEMENTS

I want to express my special thanks to my advisor Professor Mahmut Faruk Akşit for his support, encouragement, advices, and guidance for my thesis study. He is my role model as an incredible supervisor, lecturer and wise person.

I would also like to thank my committee members Professor Yahya Doğu for his precious support in Computational Fluid Dynamics; Professor Ali Koşar for his spectacular guidance, Professor İlyas Kandemir for his significant recommendations, and Professor Kemalettin Erbatur for his precious interest in this study.

I would like to thank my colleagues Utku Ünlü for his support, Ali Ihsan Yurddaş and Serhan Güler for guidance in manufacturing; Ercan Akcan, Eray Erdaş, Abdullah Çar and Mehmet Bulun for their support and assistance on experimental setup; Serdar Taze and Bora Yazgan for discussions in CFD.

I would like to acknowledge that The Scientific & Technological Research Council of Turkey (TÜBİTAK) provides financial support during my Ph.D. period. This thesis is supported by SDM Research&Engineering.

I want to convey my thanks to each member of Sabanci University Mechatronic Engineering Graduate program. I would like to extend my thanks to Mehmet Emre Kara, Ali Ihsan Tezel and Kerem Aydemir for their amusing friendship and valuable support.

I am very thankful to have the love of my life, my spectacular wife Menekşe Gizem Görgün. Her constant love, care, endless support, and patience provide wonderful motivation and energy to me during my Ph.D journey.

Last but not least, special thanks to my family, who make me feel peace of mind. I always feel their support and best wishes.

## TABLE OF CONTENTS

1	INTRODUCTION .....	1
1.1	Cloth Seal Structure .....	4
1.2	Main Issues in Cloth Seals .....	9
1.2.1	Relative Displacement .....	9
1.2.2	Wear .....	11
1.2.3	Stress .....	13
1.2.4	Leakage .....	13
1.3	Problem Statement .....	14
2	BACKGROUND AND LITERATURE REVIEW .....	16
2.1	Static Seal Designs .....	16
2.2	Cloth Seal Designs .....	17
2.3	Leakage Analysis of Cloth Seals .....	19
3	MATHEMATICAL MODELLING .....	20
3.1	Navier-Stokes Equations for Porous Medium Flow .....	21
3.2	Porous Media Resistance Coefficients .....	23
3.2.1	Bernoulli Equation Approach .....	23
3.2.2	Pressure Drop – Velocity .....	26
3.2.3	Sutherland-Ideal Gas Approach .....	27
3.2.4	Ergun’s Equation .....	28
3.3	Cloth Weave Properties .....	29
3.3.1	Porosity .....	29
3.3.2	Tortuosity & Surface Area to Unit Volume Ratio .....	32
3.4	Equivalent Gap Calculation .....	33
3.5	Uncertainty Analysis .....	34
3.6	Reynolds Averaged Navier-Stokes Equations with Standard K-Epsilon Model 35	
3.7	Navier-Stokes Equations with Derived Equations for Porous Medium Flow ..	37
3.8	Equations of State .....	38
4	EXPERIMENTAL SETUP .....	40
4.1	Cloth Weave Test Rig .....	40
4.1.1	In-plane Cloth Weave Test Setup .....	42

4.1.2	Out-of-plane Cloth Weave Test Setup .....	43
4.2	Cloth Weave Leakage Measurements Results.....	44
4.2.1	Shute Direction.....	44
4.2.2	Warp Direction.....	46
4.2.3	Diagonal Direction .....	48
4.2.4	Cross Direction.....	50
4.2.5	Comparison of Cloth Weave Tests with Literature.....	52
4.3	Cloth Seal Test Rig.....	54
4.4	Uncertainty Analysis of Leakage Test Results.....	56
4.4.1	Cloth Weave.....	56
4.4.2	Cloth Seal .....	57
5	CLOTH WEAVE AND CLOTH SEAL CFD MODEL ANALYSIS .....	59
5.1	Cloth Weave CFD Analyses and Correlation with Experiments .....	59
5.1.1	Comparison of Pressure Drop-Velocity & Sutherland-Ideal Gas Approach 63	
5.1.2	Sutherland-Ideal Gas Approach CFD Analysis of Cloth Weave .....	66
5.2	Cloth Seal Benchmark CFD Study with Conjugate Heat Transfer Model.....	75
5.3	Cloth Seal CFD Analyses .....	80
5.3.1	Cloth Seal CFD Analysis in Test Conditions.....	81
5.3.2	Cloth Seal CFD Analysis in Turbine Conditions .....	85
6	DESIGN OF EXPERIMENTS.....	90
	Cloth Seal Leakage Performance Parameters .....	90
6.1	Screening Experiment Design .....	91
6.2	Main Experiment Design.....	98
7	CONCLUSION .....	105
7.1	Cloth Weave .....	105
7.2	Cloth Seal .....	107
7.3	Contributions .....	109
7.4	Future Work.....	112
8	REFERENCES.....	114
	Appendix A: Cloth Seal Geometric Gap vs Pressure Ratio.....	120
	Appendix B: Preload Force and Tightening Torque.....	120
	Appendix C: Compressibility Factors for Air.....	121
	Appendix D: Gas Turbine System Level Secondary Flow/Performance Analysis .....	122

## LIST OF FIGURES

<b>Figure 1.1: Typical seal types and groups in the turbomachinery industry [2].....</b>	<b>1</b>
<b>Figure 1.2: Cloth seal applications in a gas turbine.....</b>	<b>2</b>
<b>Figure 1.3: Cloth seal applications at Transition Duct – First Stage Nozzle Junction [3].....</b>	<b>2</b>
<b>Figure 1.4: Normalized equivalent gap of different Nozzle-Shroud intersegment seals (rigid seal versus cloth seal) [10].....</b>	<b>4</b>
<b>Figure 1.5: Cloth weave options a) Plain Weave b) Plain Dutch Weave c) Twill Dutch Weave d) Stranded Weave .....</b>	<b>5</b>
<b>Figure 1.6: Perspective view of a Twill Dutch metallic cloth weave [12].....</b>	<b>5</b>
<b>Figure 1.7: Cloth weave and cloth seal structure [14], [15] .....</b>	<b>7</b>
<b>Figure 1.8: Equivalent gap comparison (normalized with cloth thickness) of various mesh densities in diagonal direction at 206.8 kPad (30 psid) [10].....</b>	<b>7</b>
<b>Figure 1.9: A cloth seal lay-up [9] .....</b>	<b>8</b>
<b>Figure 1.10: Cloth seal design used in the present study. ....</b>	<b>8</b>
<b>Figure 1.11: Fluid flow through the cloth seal. ....</b>	<b>9</b>
<b>Figure 1.12: Turbine segments relative displacement conditions a) gap condition b) offset condition .....</b>	<b>10</b>
<b>Figure 1.13: Turbine segments relative displacement: mismatch condition.....</b>	<b>11</b>
<b>Figure 1.14: General Electric 7F gas turbine combustor cloth seal wear investigation after 12600 hours of service a) Floating cloth seal b) Mesh integrity with local cuts c) Inner seal d) Side seal [3] .....</b>	<b>12</b>
<b>Figure 3.1: Selected points in choking line (point 1) and downstream of cloth seal (point 2).....</b>	<b>24</b>
<b>Figure 3.2: An example of curve fitting between pressure drop and velocity [53].</b>	<b>26</b>
<b>Figure 3.3: Shute wire length calculations for plain weave .....</b>	<b>30</b>
<b>Figure 3.4: Shute wire length calculations.....</b>	<b>31</b>
<b>Figure 3.5: A representation of tortuous flow path .....</b>	<b>32</b>
<b>Figure 3.6: Cross-sectional views of Dutch twill weave [63].....</b>	<b>32</b>
<b>Figure 4.1: Connections and components of the in-plane test rig .....</b>	<b>41</b>
<b>Figure 4.2: Schematic and connections of the out-of-plane test rig .....</b>	<b>42</b>

<b>Figure 4.3: Shute direction cloth weave leakage test results – Cycle#1</b> .....	44
<b>Figure 4.4: Shute direction cloth weave leakage test results – Cycle#2</b> .....	45
<b>Figure 4.5: Shute direction cloth weave leakage test results – Cycle#3</b> .....	45
<b>Figure 4.6: Shute direction cloth weave leakage test results – All results</b> .....	46
<b>Figure 4.7: Warp direction cloth weave leakage test results – Cycle#1</b> .....	46
<b>Figure 4.8: Warp direction cloth weave leakage test results – Cycle#2</b> .....	47
<b>Figure 4.9: Warp direction cloth weave leakage test results – Cycle#3</b> .....	47
<b>Figure 4.10: Warp direction cloth weave leakage test results – All results</b> .....	48
<b>Figure 4.11: Diagonal direction cloth weave leakage test results – Cycle#1</b> .....	48
<b>Figure 4.12: Diagonal direction cloth weave leakage test results – Cycle#2</b> .....	49
<b>Figure 4.13: Diagonal direction cloth weave leakage test results – Cycle#3</b> .....	49
<b>Figure 4.14: Diagonal direction cloth weave leakage test results – All results</b> .....	50
<b>Figure 4.15: Cross direction cloth weave leakage test results – Cycle#1</b> .....	50
<b>Figure 4.16: Cross direction cloth weave leakage test results – Cycle#2</b> .....	51
<b>Figure 4.17: Cross direction cloth weave leakage test results – Cycle#3</b> .....	51
<b>Figure 4.18: Cross direction cloth weave leakage test results – All results</b> .....	52
<b>Figure 4.19: Comparison of cloth weave flow performance for all directions of warp, shute, diagonal and cross.</b> .....	53
<b>Figure 4.20: Schematic and connections of the cloth seal test system.</b> .....	54
<b>Figure 4.21: Pressure chamber and leakage test rig design a) CAD design of pressure chamber and test rig with control apparatus b) manufactured and assembled picture</b> .....	55
<b>Figure 4.22: Leakage test rig dimensions (the units are in mm).</b> .....	56
<b>Figure 4.23: Uncertainty analyses for cloth weave leakage tests: (a) warp direction, (b) shute direction, (c) diagonal direction, and (d) cross direction.</b> .....	57
<b>Figure 4.24: Uncertainty analyses for screening experiments.</b> .....	58
<b>Figure 4.25: Uncertainty analyses for main experiments.</b> .....	58
<b>Figure 5.1: CFD model domain and boundary conditions for in-plane directions of warp, shute, and diagonal.</b> .....	61
<b>Figure 5.2: CFD model domain and boundary conditions for out-of-plane direction of cross.</b> .....	62
<b>Figure 5.3: Mesh views for in-plane directions of warp, shute, and diagonal.</b> .....	62
<b>Figure 5.4: Mesh views for cross direction.</b> .....	63

<b>Figure 5.5: Flowchart describes the steps for CFD analyses of Sutherland-ideal gas approach (a) base point and (b) calibration process for different pressure loads.</b>	67
<b>Figure 5.6: Comparison of CFD and test results for various pressure constant (<math>C_{down}</math>) values: (a) warp direction, (b) shute direction, (c) diagonal direction, and (d) cross direction</b>	68
<b>Figure 5.7: CFD results for warp direction (<math>C_{down}=0.9</math>, <math>\Delta P=137.9</math> kPad)</b>	70
<b>Figure 5.8: CFD results for shute direction (<math>C_{down}=0.9</math>, <math>\Delta P=137.9</math> kPad)</b>	71
<b>Figure 5.9: CFD results for diagonal direction (<math>C_{down}=0.7</math>, <math>\Delta P=137.9</math> kPad)</b>	72
<b>Figure 5.10: CFD results of cross direction (<math>C_{down}=0.0</math>, <math>\Delta P=137.9</math> kPad)</b>	73
<b>Figure 5.11: Normalized pressure within the porous metallic-cloth fibers in the flow direction (normalized weave thickness (<math>z^*</math>) vs normalized pressure (<math>p^*</math>)).</b>	75
<b>Figure 5.12: CFD analysis geometry and boundary conditions for the benchmark study</b>	76
<b>Figure 5.13: Velocity vector plots of AIAA paper (left) [1] and benchmark study (right)</b>	78
<b>Figure 5.14: Velocity streamlines of AIAA paper (left) [1] and benchmark study (right)</b>	78
<b>Figure 5.15: Temperature contour plots of AIAA paper (left) [1] and benchmark study (right)</b>	79
<b>Figure 5.16: Pressure profile of benchmark study</b>	79
<b>Figure 5.17: Temperature profile of the benchmark study</b>	80
<b>Figure 5.18: Cloth seal CFD model mesh details</b>	81
<b>Figure 5.19: Normalized pressure distribution of cloth seal design in test conditions a) baseline position b) offset position</b>	82
<b>Figure 5.20: Normalized velocity vectors of cloth seal design in test conditions a) baseline position b) offset position</b>	83
<b>Figure 5.21: Normalized velocity streamlines of cloth seal design in test conditions a) baseline position b) offset position</b>	84
<b>Figure 5.22: Normalized density distribution of cloth seal design in test conditions a) baseline position b) offset position</b>	85
<b>Figure 5.23: Normalized pressure distribution of cloth seal design in turbine operating conditions a) baseline position b) offset position</b>	86

<b>Figure 5.24: Normalized velocity vectors of cloth seal design in turbine operating conditions</b>	
a) baseline position b) offset position.....	87
<b>Figure 5.25: Normalized velocity streamlines of cloth seal design in turbine operating conditions</b>	
a) baseline position b) offset position .....	88
<b>Figure 5.26: Normalized density distribution of cloth seal design in turbine operating conditions</b>	
a) baseline position b) offset position .....	89
<b>Figure 6.1: Cloth seal geometric parameters.</b>	91
<b>Figure 6.2: Pareto Chart for Screening Experiments</b>	94
<b>Figure 6.3: The effect plots for normalized leakage rate (screening experiments).</b>	94
<b>Figure 6.4: Diagrams for dimensional changes, (a) slot depth; (b) cloth width; (c) gap; (d) shim thickness.</b>	95
<b>Figure 6.5: Normalized leakage rate of experiments (screening experiments).</b>	96
<b>Figure 6.6: Normalized equivalent gap data (baseline condition).</b>	97
<b>Figure 6.7: Normalized equivalent gap data (offset and mismatch condition).</b>	97
<b>Figure 6.8: The effect plots for normalized leakage rate (Box-Behnken designs with four outliers)</b>	104

## LIST OF TABLES

<b>Table 1.1: Specifications of Haynes 25 material at room temperature [13]</b> .....	6
<b>Table 5.1: Boundary conditions and model details for In-Plane and Out-of-Plane CFD analyses</b> .....	61
<b>Table 5.2: Error between experimental and CFD leakage rate results (Pressure Drop – Velocity approach)</b> .....	64
<b>Table 5.3: the leakage difference between the test and CFD in warp direction (Sutherland-ideal gas approach for resistance coefficients)</b> .....	65
<b>Table 5.4: CFD analysis boundary conditions and leakage result for the benchmark study</b> .....	77
<b>Table 5.5: Properties of material used in the CFD model</b> .....	77
<b>Table 5.6: Boundary conditions and results of CFD analysis of cloth seal (leakage test condition)</b> .....	81
<b>Table 5.7: Boundary conditions and results of CFD analysis of cloth seal (turbine condition)</b> .....	85
<b>Table 6.1: Candidate parameters for cloth seal leakage performance study</b> .....	91
<b>Table 6.2: Parameters of screening experiments with levels</b> .....	92
<b>Table 6.3: Screening experiments</b> .....	93
<b>Table 6.4: The parameters of the main experiments with levels</b> .....	99
<b>Table 6.5: Main experiments</b> .....	100
<b>Table 6.6: Leakage rate error between experiments and closed-form equation</b> .	102
<b>Table 6.7: Leakage rate error between confirmation experiments and closed-form equation</b> .....	103
<b>Table 6.8: Leakage rate error between additional confirmation experiments and closed-form equation</b> .....	103

## NOMENCLATURE

$C_{\text{down}}$	=	Pressure constant
$C_p$	=	Specific heat at constant pressure
$D_p$	=	Particle diameter
$D_s$	=	Shute diameter
$D_w$	=	Warp diameter
Eq. Gap	=	Equivalent gap
$g$	=	Gap
$g_c$	=	Gravitational constant for British units
$H$	=	Hardness
$H$	=	Enthalpy
$K$	=	Permeability
$k$	=	Coverage factor for uncertainty
$\Delta L$	=	Length of porous domain
$\dot{m}$	=	Mass flow rate
$n_s$	=	Number of shute fibers per inch length
$n_w$	=	Number of warp fibers per inch length
$P$	=	Pressure
$P_{\text{atm}}$	=	Atmospheric pressure
$P_d$	=	Downstream pressure
$P_u$	=	Upstream pressure
$p^*$	=	Normalized pressure
$\Delta P$	=	Pressure load
$R_c$	=	Specific Gas Constant
$R_0$	=	Universal Gas Constant
$S$	=	Sutherland Temperature
$S_M$	=	External momentum source or sink
$T$	=	Temperature
$t_{\text{total}}$	=	Total wear thickness
$u$	=	Velocity
$u_a$	=	Type A uncertainty
$u_b$	=	Type B uncertainty
$u_c$	=	Combined uncertainty
$u_e$	=	Expanded uncertainty
$u_i$	=	Superficial velocity
$w$	=	molecular weight
$x$	=	x-coordinate
$y$	=	y-coordinate
$z$	=	z-coordinate

$z^*$  = Normalized weave thickness

***Greek Symbols***

$\alpha$  = Inertial quadratic resistance

$\beta$  = Linear viscous resistance

$\gamma$  = Specific ratio of heats

$\varepsilon$  = Porosity

$\mu$  = Dynamic viscosity

$\rho$  = Density

***Abbreviations***

AIAA = American Institute of Aeronautics and Astronautics

ANSYS = A commercial software

CAD = Computer Aided Design

CFD = Computational Fluid Dynamics

CFX = A commercial software

FF = Flow Function

# 1 INTRODUCTION

Gas turbines operate with high pressure and temperature for higher power. The efficiency demands for gas turbine technology require detailed research on understanding and development for any piece of the turbine. The efficiency is increased by lower leakage rate of flows, new manufacturing methods, new material technology, superior cooling systems, etc. Secondary leakage flows have huge impact on overall turbine performance. Seals are applied to decrease leakage flows in turbines, and they are also important for controlling rotor dynamic stability in transient conditions. Therefore, high-performance seals are required to meet efficiency demands. Inefficient sealing results in more power consumption by the compressor, and reduces the temperature of the main hot gas flow due to cold parasitic leakage flow [1]. Advances in sealing technology have a considerable impact on decreasing operational costs, fuel consumption and emissions.

The types of seals in turbomachines are grouped in Figure 1.1. Turbomachinery sealing takes place not only between rotating and stationary components but also between stationary components. Leakage mass flow reduction between stationary components is one of the key objectives for gas turbine performance studies. Some static seal locations are shown in Figure 1.2 and Figure 1.3. Static seal are applied between can-annular transition ducts, nozzles, shrouds etc.

<b>TYPES OF SEALS</b>		
<b>STATIC SEALS</b>	<b>DYNAMIC SEALS</b>	<b>ADVANCED SEALS</b>
<ol style="list-style-type: none"> <li>1. Metallic seals</li> <li>2. Metallic cloth seals</li> <li>3. Cloth and rope seals</li> </ol>	<ol style="list-style-type: none"> <li>1. Tip sealing</li> <li>2. Abradables</li> <li>3. Labyrinth seals</li> <li>4. Brush seals</li> <li>5. Face seals</li> <li>6. Oil seals</li> <li>7. Buffer sealing</li> <li>8. Honeycomb seals</li> <li>9. Rim sealing</li> </ol>	<ol style="list-style-type: none"> <li>1. Finger seal</li> <li>2. Non-contacting finger seal</li> <li>3. Leaf and wafer seals</li> <li>4. Hybrid brush seals</li> <li>5. Aspirating brush seals</li> <li>6. Micro-dimple</li> <li>7. Wave interfaces</li> <li>8. Seal bearing</li> </ol>

**Figure 1.1: Typical seal types and groups in the turbomachinery industry [2]**

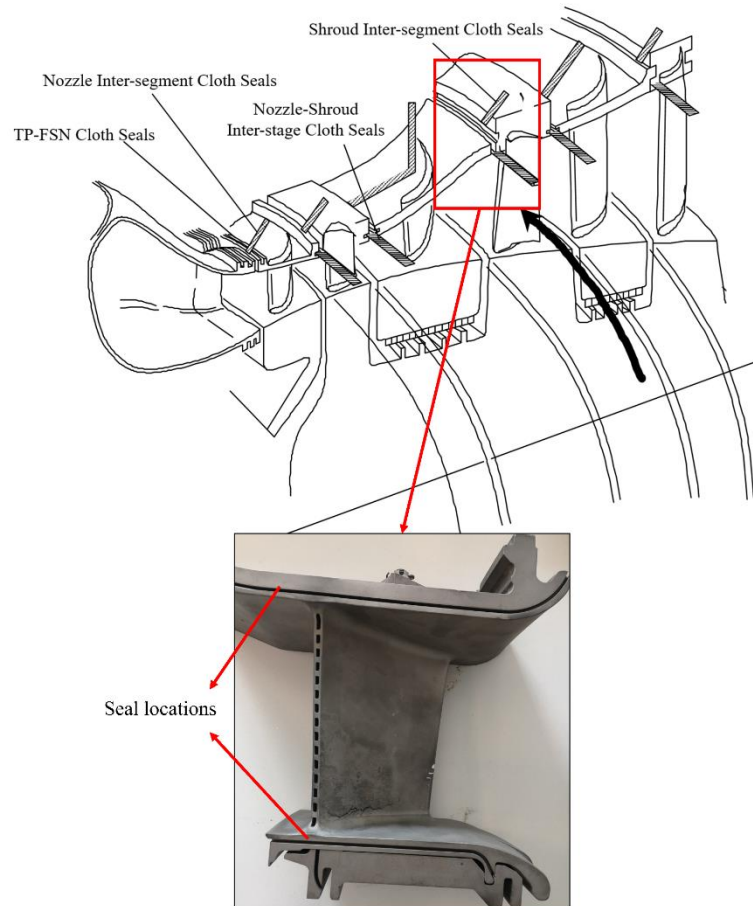


**Figure 1.2: Cloth seal applications in a gas turbine**

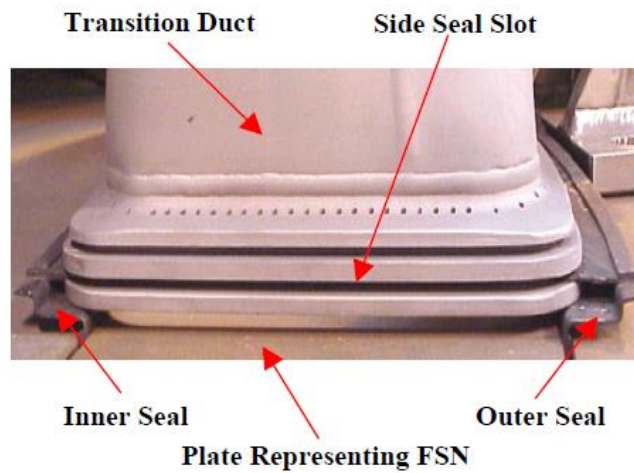


**Figure 1.3: Cloth seal applications at Transition Duct – First Stage Nozzle Junction [3]**

Previous studies show that approximately one-third of the total stage efficiency is determined by the leakage rate in the clearances of turbomachines [4],[5] Leakage performance of a seal is related to leakage rate which is defined as mass flow rate that

leaks through the seal. In turbines, seals are usually applied to minimize mass flow rate. Therefore, leakage performance becomes better if mass flow rate is decreased.

Metallic solid plate seals are static sealing elements which involve thick metal shim that can be configured in many ways. Metallic solid plate seal technology has been developed over decades. However, this traditional metal shim seals are inadequate to meet the requirements in terms of wear, compliancy, and leakage when adjacent components significantly move in axial and radial directions due to manufacturing tolerances, assembly tolerances, vibration or thermal expansion [6]. Due to high stiffness, the bending of a thick solid plate is limited. Therefore, thick solid plate seals cannot flex and close the clearance between seal surface and slot surface under offset and mismatch conditions. Such seals contact locally with slot surfaces, leading to local wear and crucially worsening leakage performance. Thinner solid seals provide better compliancy. However, sacrificial wear volume which is needed for long life, is diminished due to low thickness. In order to eliminate the limitations of metallic solid seal, new metal cloth seals are investigated [7]. Cloth seal is an answer to reduce leakage rate and increase wear life as an alternative for metallic solid seals. It can be applied between stationary components (combustors, nozzles, shrouds, diaphragms) of gas turbines and packing ring segmented end gaps of steam turbines. A previous study [8] shows that cloth seal delivers %70 leakage reductions in nozzle segments and up to %30 in combustors. Nozzle-shroud cloth seal applications enhance %0.5 output performance and decrease %0.25 heat rate of an industrial gas turbine [8]. Service life is also extended with flexible cloth seals by at least %50 [3].

Applications of cloth seal reduces leakage rate and allows compliancy. Flexibility of cloth seal leads to reduce local wear rate, and damp forces due to assembly tolerances or oscillations on the rotor. Cloth seal is an innovative technology and it is preferred rather than metallic solid seal in critical regions of turbomachines due to superiority in the aspect of leakage performance and wear life. In combustion laboratory tests, cloth seals serve 30-35% reduction in leakage which means more air for combustion and less NOx emissions [3]. A previous study [9] reveals that the cloth seal leaks 65% less than rigid seals under baseline conditions and %77 less than rigid seals when subjected to offset&mismatch conditions. In another study (Figure 1.4), leakage performance improvements are illustrated for both baseline (zero offset and zero mismatch) and

offset&mismatch conditions [10]. In Figure 1.4, the equivalent gap is a representative gap that decreases with better sealing performance.

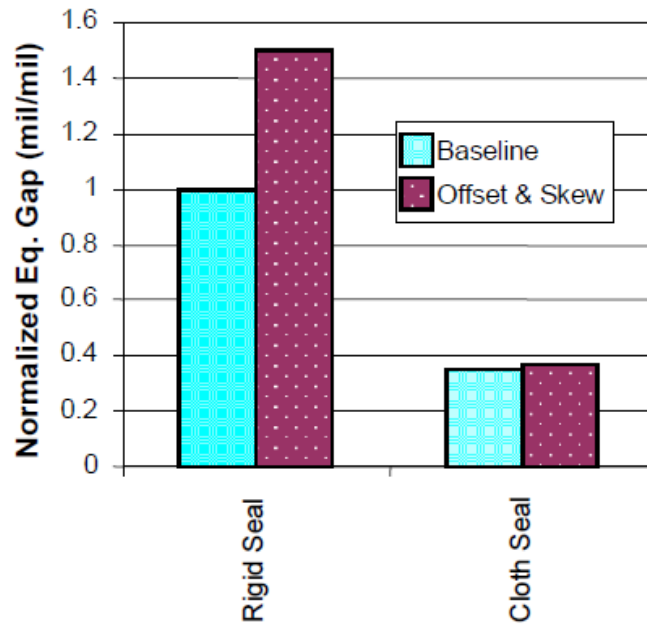


**Figure 1.4: Normalized equivalent gap of different Nozzle-Shroud intersegment seals (rigid seal versus cloth seal) [10]**

### 1.1 Cloth Seal Structure

The cloth seal includes one or more cloth layer and thin shim metal. Several designs are proposed in the literature and patents. Cloth seals are shaped by combining thin sheet metals (named as shims) and woven cloth metal layers. Shim eliminates direct leakage and provides structural strength, while cloth weave enables additional wear volume without contributing stiffness significantly [8]. Metal shims are bent to create right and left tabs, therefore, choking flow interfaces are occurred between the tab and turbine slot. As a result of that, fluid cannot escape easily from lateral gaps. A single or pack of cloth layers may be placed on upper or below side of metal shim. Shim and cloth layers are held by spot welds. Although increasing the number of spot welds reduces the probability of disintegration of cloth and shim layers, it leads to high stiffness and lack of flexibility.

Several high density cloth weave types are evaluated as shown in Figure 1.5. Plain weave is the most basic weave form, which is woven by alternating shute fiber under and over warp fiber. In twill woven fibers, shute fiber passes over and under a pair of warp fibers. Plain Dutch woven fibers are woven with smaller fibers in the shute direction and

larger fibers in the warp direction. Dutch twill weave is a mixture of twill and Dutch weaving where smaller-diameter shuttle fibers are woven by alternating two larger warp fibers. In stranded weave, bundles of warp and shuttle metals pass over and under one another. It increases the contact surface, therefore providing high wear performance.

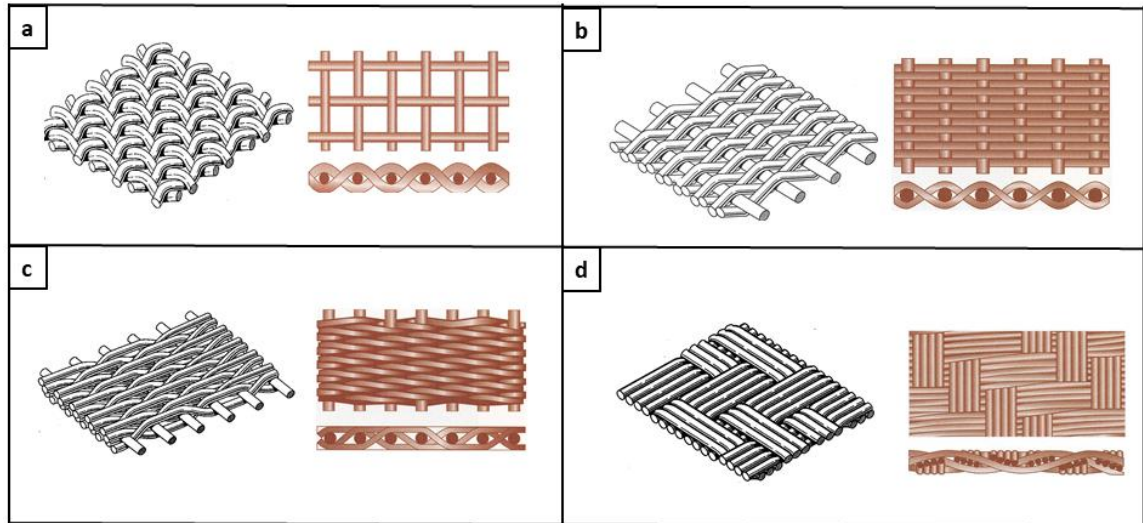


**Figure 1.5: Cloth weave options a) Plain Weave b) Plain Dutch Weave c) Twill Dutch Weave d) Stranded Weave**

A direction which has a  $45^\circ$  angle with both warp and shuttle directions, named as ‘diagonal direction’. Diagonal direction increases wear resistance and help mesh integrity [11]. Due to this reason, experiments and CFD analyses are also done for diagonal direction in this study.

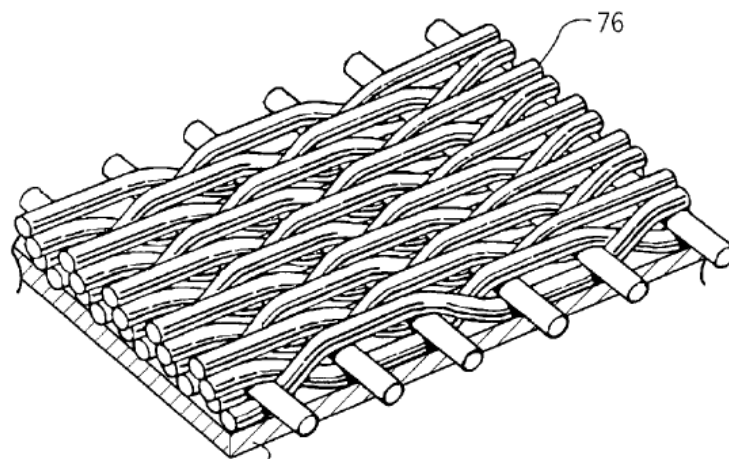


**Figure 1.6: Perspective view of a Twill Dutch metallic cloth weave [12]**

Several materials (Haynes, Inconel, Waspalloy series) are available to manufacture cloth and shim layers. Hardness, oxidation, tensile strength, melting point, thermal

expansion, thermal conductivity, creep, and fatigue resistance are the important mechanical properties for material selection. Haynes 25 is selected for the metallic-cloth fiber material. It is a cobalt–nickel alloy that provides good strength and oxidation resistance at high temperature. The features of Haynes 25 are revealed in Table 1.1. For high-temperature applications, Haynes 188 yields well as the shim material [11].

<b>Material Property</b>	<b>Value</b>
Nominal composition (weight percentage)	Cobalt (51% ), nickel (10%), iron (3% max.), chromium (20%), molybdenum (1% max.), tungsten (15%), manganese (1.5%), silicon (0.4% max), carbon (0.1%)
Density	9.07 g/cm <sup>3</sup>
Melting range	1330–1410 °C
Thermal conductivity	10.5 W/m- °C
Specific heat	403 J/kg- °C
Dynamic modulus of elasticity	225 GPa
Ultimate tensile strength	1015 MPa

**Table 1.1: Specifications of Haynes 25 material at room temperature [13]**

Since cloth seal is contacting seal, it is not suitable to be placed between rotating and stationary components. It can be inserted between rotating components which have no relative rotating motion. Depending on the sealing location, cloth seal may or may not be fixed to turbine slots. In this study, it is applied between stationary components and freely moving in slots. Figure 1.7 illustrates cloth weave and cloth seal structure from the literature. Weave type, warp diameter, shute diameter, warp density and shute density, number of layers, material are the parameters of cloth weave for selection. Warp metals are placed in the middle of cloth weave while shute fibers wrap warp metals from the upside and downside. Cloth weave can be manufactured with several mesh densities such as 20 x 200, 20 x 250, 20 x 350, 24 x 110, 30 x 150 and 30 x 250 (number of warp fibers per inch x number of shute fibers per inch). As illustrated in Figure 1.8, leakage performance is compared for the aforementioned mesh densities at 206.8 kPa (30 psid) and experimental results imply that better leakage performance is obtained with 30x250 mesh density than other tested weaves [10]. Chupp et.al [11] also emphasize that Dutch twill weave with 30 x 250 fiber density per inch is the best cloth weave option for sealing purposes.

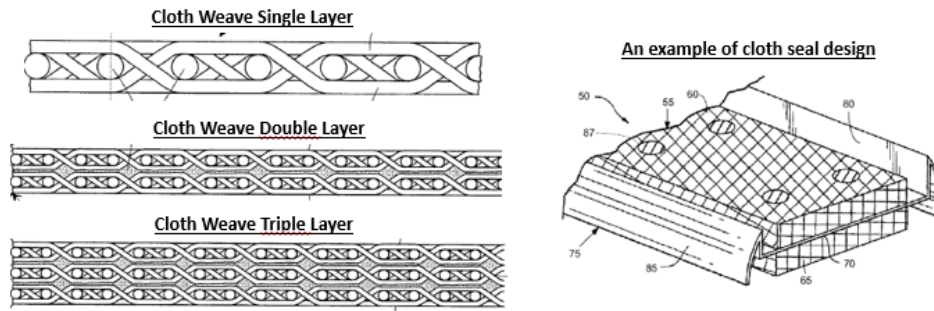


Figure 1.7: Cloth weave and cloth seal structure [14], [15]

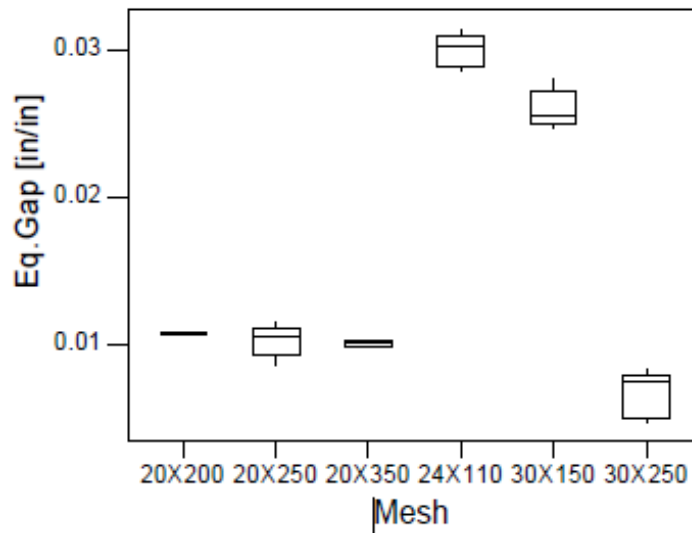
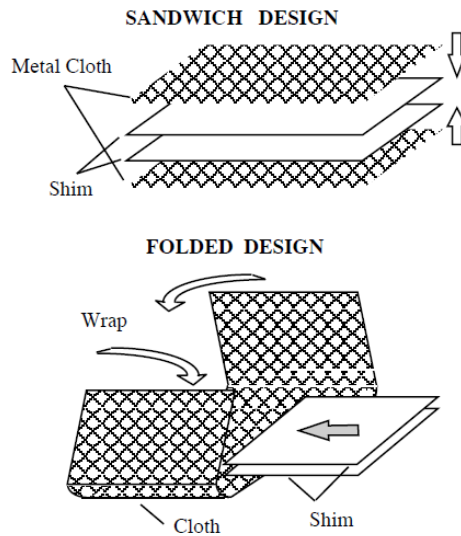


Figure 1.8: Equivalent gap comparison (normalized with cloth thickness) of various mesh densities in diagonal direction at 206.8 kPad (30 psid) [10]

In cloth seal applications, fluid usually moves in the direction from upstream region which has higher pressure to downstream region which has lower pressure. Different cloth seal designs are illustrated in Figure 1.7 and Figure 1.9. Cloth weave merges with metal shim via spot welds to protect the flexibility of seal. Other types of welding may also be applied in edges of cloth weave and metal shim. Seam welding may be applied to weld metal shims to each other if there is more than one shim layers are used. Metal shim is usually bent from edges to generate tabs. Thick tabs reduce seal flexibility whereas thin tabs may fail due to high stresses. Thicker cloth weave may weaken welding and decrease compliancy while thinner weave has lower wear life.



**Figure 1.9: A cloth seal lay-up [9]**

Figure 1.10 illustrates a representative cloth seal design that is used in the present study. To choke the flow between the cloth seal and turbine components, metal shims are bent at each edge to create tabs. A single cloth weave is located at the downstream side of the shim to provide sacrificial wear volume. Another cloth weave is placed upstream side of the shim to protect shim from damage under offset and mismatch conditions. Shim and cloth layers are assembled by spot welds.

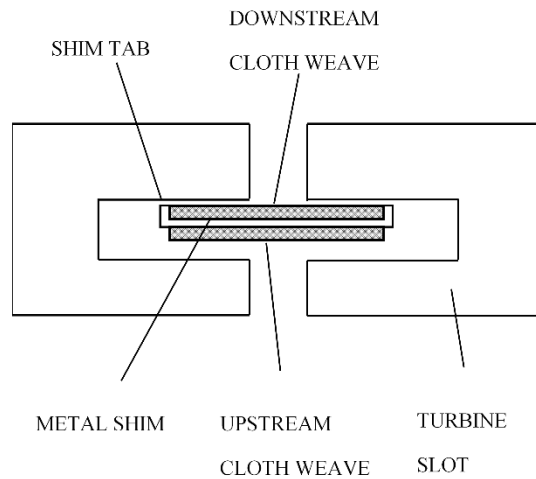


**Figure 1.10: Cloth seal design used in the present study.**

Fluid flow through the cloth seal is shown with red arrows in Figure 1.11. Flow approaches from upstream to the area between lateral slot surfaces and shim tabs. Then it is directed to the choking zone where the flow area is minimum. Once passed the choking

zone, flow is exposed to throttling between cloth weave and downstream slot surface, and subject to resistance through voids inside the cloth weave placed near downstream.

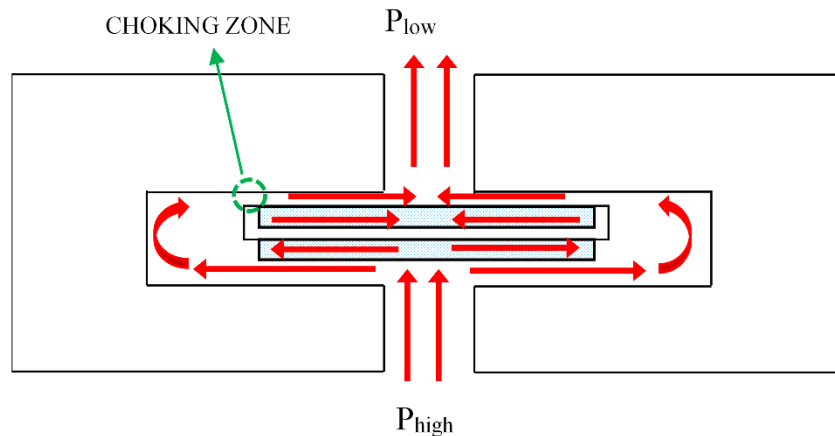


**Figure 1.11: Fluid flow through the cloth seal.**

## **1.2 Main Issues in Cloth Seals**

The main design issues in cloth seal applications are the misalignments, wear, structural durability, and leakage performance. Therefore, novel cloth seal designs should overcome crucial subjects as relative displacement, wear, stress, and leakage. In turbine operating conditions, performance and life of the cloth seal are usually influenced by mentioned phenomena below.

### **1.2.1 Relative Displacement**

Adjacent turbine components may have a considerable relative displacement between each other due to manufacturing tolerances, assembly tolerances, vibration, or thermal growth. Such relative displacements may increase or decrease the distance between turbine slots. The change of the gap between turbine disks is called as 'gap condition' which may squeeze the cloth seal or cause to fall down of cloth seal from the cavity (Figure 1.12). Thermal expansion and contraction need to be handled during start and stop process of turbomachinery. For these reasons, cloth seal length should be selected correctly to handle transient turbine conditions. Gap condition caused by thermal growth, vibration, or assembly problems.

Slots machined for cloth seal insertion may be out of alignment with each other, so an offset occurs between the slots. This situation is named as ‘offset condition’ that may result in excessive local stresses and cloth seal damage unless it is flexible. Offset condition occurs due to vibration or relative thermal growth of adjacent turbine segments. Gap and offset conditions in a seal slot are illustrated in Figure 1.12.

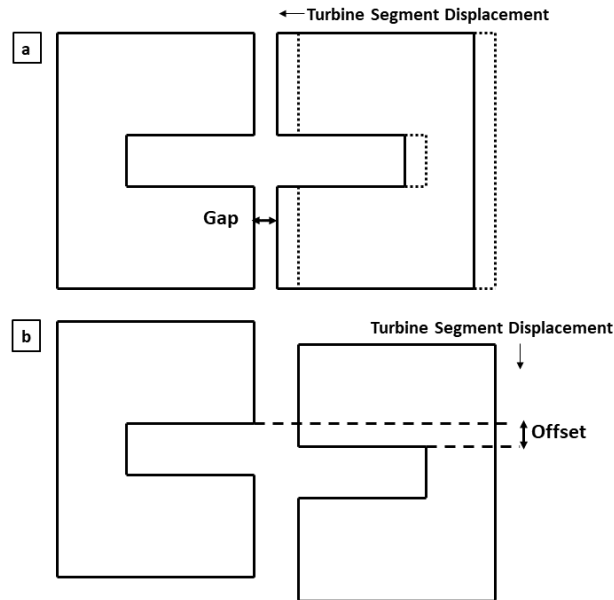


**Figure 1.12: Turbine segments relative displacement conditions a) gap condition b) offset condition**

There may be an angle between slots, especially for transition duct applications of cloth seal. This is named as ‘mismatch condition’ which may lead to lack of compliancy, worse leakage performance, excessive local wear, or failure of cloth seal. Mismatch condition may result from vibration, assembly tolerances or wrong assembly. The angle between surfaces of two adjacent segments is shown in Figure 1.13.

Uneven thermal expansions generate valleys and peaks in a slot profile. In this condition, cloth seal has wavy seating surfaces. A flexible cloth seal design can efficiently operate in gap, offset, mismatch conditions and uneven seating surfaces.

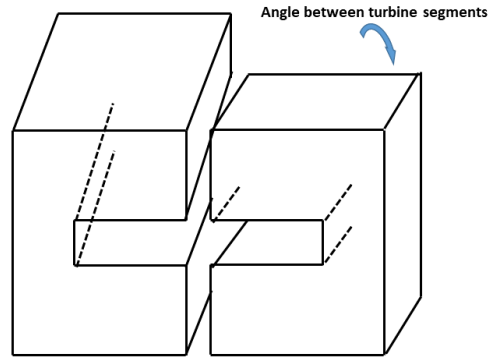


**Figure 1.13: Turbine segments relative displacement: mismatch condition**

### 1.2.2 Wear

Cloth seal is a static seal which has contact with surfaces unlike labyrinth, brush, or leaf seals. As a result of pressure difference, it applies force to the surface. Due to vibration, a relative motion occurs between cloth seal and turbine slot. Wear is inevitable for cloth seal or other stationary seals. Woven cloth layers in the cloth seal provide sacrificial wear volume without significant stiffness increase. Wear life of the design should be higher than the duration between maintenances. Wear rate is equal to volume loss over distance slid, is calculated with Archard's Equation stated as:

$$\Delta V = K \frac{F_n}{H} \quad (1.1)$$

In Equation 1.1, K presents wear coefficient,  $F_n$  is normal force and H symbolizes hardness of softer material. Both sides are divided with the contact area to get local wear depth (W):

$$\Delta W = \frac{\text{Wear Thickness Lost}}{\text{Distance Slid}} = K \frac{F_n}{HA} = K \frac{P}{H} \quad (1.2)$$

P is the contact pressure. Both sides are multiplied with distance slide to get wear thickness lost.

$$\Delta W = \text{Wear Thickness Lost} = K \frac{PL}{H} \quad (1.3)$$

Equation 1.3 shows the wear thickness lost per sliding time. In order to find wear thickness lost for a specified time, nominator is multiplied with total time whereas denominator is multiplied with sliding time.

$$W = \text{Total Wear Thickness Lost} = K \frac{PL}{Ht_{slid}} t_{total} = K \frac{PV}{H} t_{total} \quad (1.4)$$

V stands for sliding velocity and  $t_{total}$  refers to the total time that measured wear thickness. Equation 1.4 shows that higher pressure difference and higher sliding velocity enhance wear thickness lost whereas higher hardness of softer material decreases wear thickness lost. Ongun et. al. [16] developed an analytical model characterizing wear behavior of woven structures to estimate wear life of metal cloth seals. They provide an equation for total volume lost which gives the wear rate of metal cloth by conducting Archard Equation [17],[18].

Wear profile in cloth seal is directly related to flexibility. Excessive local wear may occur in a short time unless a proposed design is compliant. Moreover, cloth seal may split into pieces as a result of local wear that leads to a dangerous situation since pieces break from seal join main flow (burned gas) and hits turbine blades. Choking zone may also be lost if uneven wear occurs. This situation has a negative impact on seal leakage performance. A good design should serve a wide contact surface between the seal and slot with the aim of distributing force to a wider area and declining contact pressure.

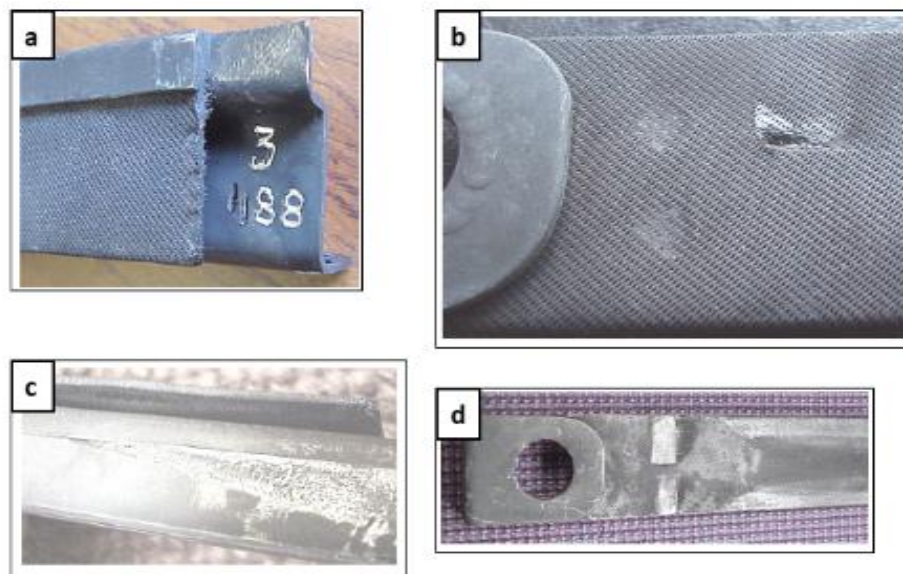


**Figure 1.14: General Electric 7F gas turbine combustor cloth seal wear investigation after 12600 hours of service a) Floating cloth seal b) Mesh integrity with local cuts c) Inner seal d) Side seal [3]**

### **1.2.3 Stress**

Traditional metallic rigid seals are designs with high stiffness in order to solve wear problems. Therefore, stress levels are high in harsh operating conditions. The advantage of cloth seal is operating with high wear life and low stiffness rate. A good cloth seal design is able to handle stresses result from pressure load, wavy seating surfaces, relative displacements, and vibration. Pressure load applies the force on cloth seal and bending stress occurs due to curved slot surface, vibration, offset and mismatch conditions. Welding type and welding parameters also influence stiffness, hence designer should carefully determine welding parameters. Excessive local stress levels cause to rupture of welding or split of cloth weave. In conclusion, cloth seal design should prevent itself from high local stress levels during harsh turbine operating conditions.

Dogu et. al. [1] determined the flow and temperature fields over the cloth seal. The interesting result is that the cloth layer acted as a thermal shield protecting the shim from overheating and excessive thermal stresses in addition to the known wear shield effect.

### **1.2.4 Leakage**

Main aim for sealing application is to reduce undesired secondary leakage flow which occurs in turbine blade tip, transition duct, etc. Several points reduce leakage performance of the cloth seal design. The clearance between seal and seating surface remains high unless the design is compliant. Another issue is uneven sealing surface due to local wear. In this situation, valleys and peaks reveal in choking zone and flow leaks from small spaces. Moreover, cloth seal may slide to one slot in offset condition. In this condition, it may lost its contact with its adjacent slot. High pressure flow penetrates spaces where the contact has been lost. These issues have a negative impact on sealing performance of cloth seal, for this reason, the designer should consider all the issues.

In some applications, temperature of cloth seal and adjacent slots may increase if leakage is blocked completely. Without any leakage, film cooling cannot be supplied. For these reasons, there is a trade-off between cooling and leakage performance.

### 1.3 Problem Statement

The sealing efficiency of the cloth seal is directly correlated with leakage performance. Cloth seals have a complex structure with several design parameters which influence leakage rate through cloth seal. For better efficiency, one should design seals with minimum leakage during entire operating time. Therefore, studying, improving and optimizing cloth seal designs are key to improve leakage performance.

Since the leakage through the cloth weave affects the overall cloth seal performance, the three-dimensional flow in the cloth weave needs to be investigated by testing and with flow modelling tools to constitute a cloth seal design tool. However, modelling the flow through the complex weave voids among each warp and shute fiber involves a very complex flow structure, extensive effort and high CPU time in terms of not only leakage determination but also structural and wear analyses. Therefore, a bulk porous medium flow model is applied to the model cloth seal weave fibers. Several experimental studies were conducted, and equations were developed to detect the flow resistance of a woven cloth [19]-[23]. However, these equations are limited with a mesh type or they need correlated parameters with tests. Therefore, a correlation study with experiments is needed. In this study, cloth weave is modeled as porous medium with inertial and viscous flow resistance coefficients. Sealing performance is affected by these coefficients since they have an impact on leakage rate. Porous medium flow resistance coefficients are changing with respect to geometry, pressure, temperature etc. For this reason, several methodologies (Bernouilli, pressure drop – velocity, Sutherland-ideal gas approach, Ergun equation) are examined in this study to estimate flow resistance coefficients. The present study investigates the accuracy of several methodologies to calibrate porous medium flow resistance coefficients at different pressure loads.

Measuring cloth seal leakage rate subject to turbine operating conditions is complicated. Due to the complex geometry of cloth weave, only applying analytical equations are inadequate to obtain a performance chart. The complex structure of cloth seal under pressure load and relatively offset position of mating surfaces, which not only be considered flow analysis but also related to overall stiffness of the seal design. This study provides a calibration of the flow resistance coefficients with respect to the pressure and temperature; therefore, CFD analyses of the cloth seal is conducted with the

calibrated resistance coefficients and operating clearance in turbine operating conditions. Therefore, the leakage rate of the cloth seal is obtained without leakage tests in turbine operating conditions.

Although several experimental and computational studies [1], [3], [7], [8], [9], [10], [16] have been published for cloth seals, their approach in determining cloth seal performance cannot be fully explained with respect to the design parameters. There is no published analytical formulation relating cloth seal leakage rates to design parameters. Literature reviews indicate that available published data about cloth seal leakage performance are not adequately detailed to derive a closed-form equation defining the relationship between seal design parameters and cloth seal leakage performance. In an effort to fill this gap, the effect of geometric parameters under varying pressure load on the cloth seal leakage performance has been investigated in this study. Pressure load is dominant operating condition that drives leakage rate. Compliant structures like cloth seals may change shape under different pressure loads. Therefore, leakage performance has been studied at different pressure levels. In order to reduce the number of parameters to a manageable size, some of the parameters are fixed and excluded from the experimental design based on the studies in the literature [10], [11]. The remaining eight parameters are included in the screening experiments. Their levels are determined to cover typical application ranges. Parameters, which have a major impact on leakage rate, are determined and analyzed in the main experiments. Equations, test rig designs, analysis models and cloth seal designs are developed in this study.

## 2 BACKGROUND AND LITERATURE REVIEW

Sealing technology is one of the important issues due to high-performance needs of turbomachines. Therefore, various types of seals are applied in turbine and compressor systems. Static metal seals are the traditional applications in gas turbines. Compliancy is lost due to low flexibility in metallic seals, therefore, efficiency and wear life decreases. Moreover, identifying the optimum sealing solution under harsh operating conditions is a challenge.

### 2.1 Static Seal Designs

Static metal seals were applied in several locations of turbines. A seal apparatus was developed by Siemens in order to enable static sealing application between transition ducts [24]. X-shaped design constructed from two metallic strips was offered by Cornett et. al. to provide flexibility and four different choking lines [25]. In another study [26], a metallic seal was extended close to side surfaces. Side edges are included grooves which generate recirculation areas for flow and decrease its energy. Grosjean [27] offers a flexible static seal that fits non-parallel grooves, made of a heat resistant alloy such as Hastelloy X and it comprises two concave central or mid parts and integral looplike symmetric parts. Such design may fail due to wear of contact surfaces which may result that a part of the seal escapes to main flow and hits turbine blades with high velocity. A metal seal is developed to apply between stator and rotor shroud and its upper surface is toothed, similar to laby seal, with the aim of swirl generation [28]. The disadvantage of such a design is lack of flexibility since the thickness of seal is high as equal to height of seal slot [28]. Another X-shaped seal spring was developed for transition duct, involves a couple of arcuately disposed spring elements and upper spring clips are held by flanges of adjacent edges [29]. A three-piece seal assembly was offered by Kellock et.al. [30] to reduce leakage between adjacent turbine segments. A spline seal and another angled spline seal restrict flow in reverse directions, and a third seal segment between spline seals connects two spline seals and restricts flow between two members [30].

## 2.2 Cloth Seal Designs

Several designs have been studied for cloth seals in the literature. A metal shim is sandwiched between two cloth layers to construct a cloth seal which has two opposing raised regions and two opposing unraised edges connecting to turbine slot surfaces [31]. A similar design was also offered by Samudra et.al. [14] to diminish leakage with its metal linear or arcuate legs. A design includes a planar shim having transverse legs in both ends, a flattened leaf spring contact with sealing surfaces on upstream side to squeeze seal in turbine slot and provide extra choking points [32]. Another spring-loaded cloth seal design involves two tabs which are bent to upstream side, have a narrow-angle with the main flat surface [33]. A shim member comprises a middle part with two surfaces and raised longitudinal edges, wherein recesses are shaped by raised longitudinal edges and mesh layers [34]. Porous layers were sandwiched by upper and lower metal shims to make a flexible design [35] in misalignment conditions, however, wear starts from metal layers and loss of these layers may lead to a significant amount of leakage increase. General Electric improves a cloth seal design that comprises imperforate foil layer assemblage made from a metal, ceramic and/or polymer which is covered by cloth layer is made from metal, ceramic and/or polymer fibers. It is claimed that gas-path offered design provides %1 leakage and 6ppm NO<sub>x</sub> production in comparison to %2.4 leakage and 15ppm NO<sub>x</sub> production of conventional metal rigid seal [36]. Another foil layer enclosed by cloth weave design [37] is claimed that %0.4 gas-path leakage with improved design while conventional metal rigid seal has %2.4 gas-path leakage. A twilled cloth layer consists of warp and shute fibers made from a cobalt-based super-alloy covers foil layer, and such design provides low leakage, high wear resistance and compliancy in the condition of misalignment, vibration and relative thermal growth of adjacent turbine components [38]. Aksit et. al.[39] developed a cloth ring design for a tubular cavity which provides low leakage and compliancy with the change of cavity dimensions, purges the cavity of unwanted gases and/or cool cavity. In another design, a seal ring includes innermost layer with a woven metal core formed of stainless steel surrounded by an annular metal layer which is covered by metal foil and finally, the outermost cover of the seal consists of metallic braided material [40]. Such design [40] may provide better leakage performance in exchange for low flexibility in comparison to only cloth design [39]. Vedantam et. al. [41] developed a composite tubular woven seal that involves an inner woven metal component covered by annular silica fiber layer that is covered by a

metal foil with braided stainless-steel outside cover. Metal foil layer blocks leakage, and braided cover supplies a wear surface from outside while metal core and silica fibers hold circular configuration in cross-section [41]. A leakage seal includes two symmetric foil layers and two symmetric covered cloth layers that both have distal ends which diverge from flat region to define curved hook where cloth part is wrapped over foil part [42]. In another design, a spline seal includes metal central core which fills the gap between turbine segments, covered with cloth from all surfaces [43]. Thus, it allows relative radial motion of turbine components without binding or severing of the spline seal [43]. Lacy et. al. [44] offers a gas path leakage seal which comprises a manifold with profile edges having a “shepherd hook” shape, a cloth layer on upper surface and another cloth layer on lower surface. Such design enables flexibility when turbine segments expand and the seal squeezes between lateral surfaces [44]. Another cloth seal design which is bent between segments, involves a shim surrounded by cloth metal [45]. Analysis tools showed that the proposed seal provides %0.4 leakage rate which is equal to tens of thousands of dollars savings per turbine per year in comparison to conventional metallic seal designs [45]. A transition piece seal comprises first flange on one side vertically, second flange placed to adjacent transition piece horizontally, a spring element having a mounting flange engaged the second flange of the transition piece seal support and a flex portion with free edge [46]. The seal which handles with relative movement and misalignment of adjacent structures, involves a long strip metal alloy flanked by 180° folds which creates two margins towards center of seal [47]. These margins bent outwards to create edge sections. Multiple stacked woven cloth layers are brazed or welded from side edges, placed with 45 degrees to the warp and shute directions [15]. 40 warp wires per inch was selected with 0.0105-inch diameter and 220 shute wires per inch was included with 0.0084-inch diameter for the aforementioned design [15]. Flanagan et.al. [48] offer V-shaped or various W-shaped convolution seals to reduce leakage around canular type transition ducts. In another design, two metal shim layers with raised longitudinal edges attached to a cloth layer with a plurality of spot welds or seam welds with 30x250 cloth density (per inch) with 7-10 mils warp and shute thickness [49]. A supplemental seal for the chordal hinge seal comprises more than one metal shims covered by cloth supported by a bracket [12]. In another design [50], a cloth seal comprises of two peripheral portions that one peripheral portion of the cloth seal lies to a cavity in a turbine segment whereas the other portion does not belong to any cavity or

slot and it has a contact surface with another turbine segment. A flexible shim covers cloth and provides a resilient structural member carrying pressure loads [50].

### **2.3 Leakage Analysis of Cloth Seals**

It is difficult to successfully analyze flow of cloth seals under operating conditions. Modeling leakage through each warp and shute fibers is a challenge. In order to comprehensively understand the complex flow through cloth seals, General Electric researchers improved a leakage setup to obtain flow performance of cloth seals [9]. Their study on leakage performance shows the overall performance improvement for both E and F type gas turbines. Leakage declines %65 in comparison to comparable rigid strip seal, and savings rise %77 in offset or mismatch conditions [9]. Aksit et. al. [10] reported that curved cloth seal provided up to %75 mass flow decrease over segmented rigid seals at corner regions.

Dogu et. al. [1] were modeled cloth material as solid with a %50 reduction in its thermal properties. Their model solved Navier Stokes and energy equations describing the mass, momentum and thermal transport using finite elements solution procedure. They showed a temperature profile on cloth seal, flow region and turbine segment. In their study, high-velocity rates occur around the choking zones. However, a more complex modeling methodology is needed to show flow behavior in cloth weave. Dogu [51] investigated brush seal flow models and categorized them as cross-flow models, bulk flow models and porous medium flow models. Cloth weave can be modeled as similar to models that have already been used for brush seals in literature [51].

### 3 MATHEMATICAL MODELLING

The structural and leakage performance of the cloth seal are determined primarily by the behavior of metal shim and cloth layers in the condition of pressure load applied. There is a need to develop or use mathematical models to investigate cloth seals in the aspect of leakage performance. This section covers the analytical study related with seal leakage and flow evaluation.

The velocity and pressure characteristic of fluid in the vicinity of the cloth seal and within the cloth fibers have an impact on the seal durability and leakage performance. The porous structure of the cloth weave affects flow path. Solving fluid equations through the complex weave voids among each warp and shute fiber involves a very complex flow structure, extensive effort, very accurate models (Large Eddy Simulation, Detached Eddy or Direct Numerical Simulation) and high CPU time in terms of not only leakage determination but also structural and wear analyses. Therefore, a bulk porous medium flow model was applied to the model cloth seal weave fibers. The porous medium approach provides simplicity and compactness. It determines dynamic flow characteristic and sealing performance. In the classic model, cloth layers are modeled as solid, therefore, no flow was allowed through cloth regions. Another approach is considered that the entire cloth layer is modeled as a single porous medium with determined flow resistance parameters to leak. The porous medium approach is applying the Navier–Stokes equation with the additional momentum sink which model flow resistance in porous medium. Resistance coefficients are correlated with experimental cloth weave leakage results for warp, shute, diagonal and cross directions. Porous medium approach has been applied for modeling cloth weave to identify flow-driven properties such as leakage rate, pressure, velocity, temperature, kinetic energy.

The porous medium approach is separated from other methods by providing the pressure, temperature distribution and velocity profile inside of cloth region in addition to leakage rate, and it serves more accurate results than solid modeling. Velocity and pressure fields in the close vicinity of cloth layers can be also observed in the light of the porous medium approach.

In this section, mathematical models for porous modeling are explained. Effective clearance calculation methodology, which is important to understand sealing performance, is detailed. Uncertainty analysis for Type A and Type B are described.

### 3.1 Navier-Stokes Equations for Porous Medium Flow

The airflow is assumed to be turbulent and compressible. The reduced Navier–Stokes equations governing the fluid flow in the upstream and downstream regions can be expressed in tensor notation as [52]:

*The Continuity Equation*

$$\frac{\partial \rho}{\partial t} + \nabla \cdot (\rho u) = 0 \quad (3.1)$$

*The Momentum Equation*

$$\frac{\partial(\rho U)}{\partial t} + \nabla \cdot (\rho U \otimes U) = -\nabla \rho + \nabla \tau + S_M \quad (3.2)$$

where the stress tensor is related to the strain rate as

$$\tau = \mu \left( \nabla U + (\nabla U)^T - \delta \frac{2}{3} \nabla \cdot U \right) \quad (3.3)$$

*The Total Energy Equation*

$$\frac{\partial(\rho h_{tot})}{\partial t} - \frac{\partial \rho}{\partial t} + \nabla \cdot (\rho U h_{tot}) = \nabla \cdot (\lambda \nabla T) + \nabla \cdot (U \cdot \tau) + U \cdot S_M + S_E \quad (3.4)$$

The relation between total enthalpy and static enthalpy as

$$h_{tot} = h + \frac{1}{2} U^2 \quad (3.5)$$

These equations, which express the continuity (Equation 3.1), momentum (Equation 3.2), and total energy (Equation 3.4) equations, respectively, describe the motion of air in both the experimental set up and CFD analysis. In Equation 3.4, the term  $\nabla \cdot (U \cdot \tau)$  represents the viscous work term, which is neglected.  $S_M$  represents external momentum sources or sinks acting on the continuum such as gravity, inertial accelerations, and resistive forces. For the porous cloth weave domain, the momentum loss through a porous region is added to the right-hand sides of Equations 3.2 and 3.4, as an external momentum and energy sink.

In addition to the Navier-Stokes equation, the Darcy model provides the relationship between pressure gradient and viscosity in a porous region. It is expressed as below:

$$-S_{M,i} = -\frac{\partial P}{\partial x_i} = \frac{\mu}{K_i} u_i \quad (3.6)$$

$x_i$  refers to orthotropic flow directions,  $\mu$  is the viscosity,  $K_i$  means permeability of the porous media and  $u_i$  is the superficial velocity in the orthotropic flow directions. Superficial velocity is a hypothetical fluid velocity assumed as only given phase or fluid is contributed to flow in a given cross-sectional area. In another way, it is the velocity for calculated mass flow rate by ignoring the influence of porous region. In the absence of porosity effect,  $u_i$  is expressed in terms of average velocity ( $u$ ) and porosity ( $\epsilon$ ):

$$u_i = \frac{u}{\epsilon} \quad (3.7)$$

Porosity model involves only the viscous resistance term in Equation (3.6). An extended version of linear Darcian model is given in Equation (3.8) is a non-Darcian porosity model for more precise resistance relationship as:

$$-S_{M,i} = -\frac{\partial P}{\partial x_i} = (\alpha_i |u_i| + \beta_i) u_i \quad (3.8)$$

$\alpha_i$  refers to inertial resistance coefficients and  $\beta_i$  refers to viscous resistance coefficients. This equation is also expressed as:

$$S_{M,i} = \frac{dP}{dx_i} = -K_{loss,i} \frac{\rho}{2} |u_i| u_i - \frac{\mu}{K_{perm,i}} u_i \quad (3.9)$$

where  $\rho$  is the density, and  $K_{loss}$  is the loss coefficient. In Isotropic Loss Model the porous flow resistance coefficients are the same in each direction. Directional Loss Model can be applied as the momentum source throughout an anisotropic porous region. The advantage of this method allows directional resistance; therefore, different resistance coefficients can be defined for streamwise and transverse directions. Usually, streamwise direction is the direction that allows fluid to flow easily. Transverse directions are perpendicular to the streamwise direction which can also be modeled as a factor of

streamwise resistance coefficient. However, transverse directions may be selected such directions that the same resistance coefficients can be assigned to transverse directions.

Porous media approach requires information about porosity and inertial and viscous resistance coefficients.

In this study, leakage and pressure levels obtained with experiments are calibrated CFD analysis with the aforementioned equations. Matching empirical and computational data provided calibrated resistance coefficient values for each direction. Details of the flow resistance coefficient calibration process are provided in Section 5.1.

### **3.2 Porous Media Resistance Coefficients**

The flow in porous medium is subject to additional flow resistances compared to that in the absence of a porous medium. Flow resistance coefficients need to be calibrated when the pressure and temperature vary. The main purpose of developing an analytical model for flow resistance coefficients in porous medium is to determine a relation between flow resistance coefficients and effective parameters, especially the pressure and temperature level, fluid properties, and porous medium geometry. For this reason, several methodologies (Bernoulli approach, pressure drop – velocity, Sutherland-ideal gas approach, Ergun equation) are used or developed to estimate flow resistance coefficients in cloth weave.

#### **3.2.1 Bernoulli Equation Approach**

The full porous model can be reached with Navier-Stokes equations and Darcy's law. The model involves advection and diffusion terms hence it is suitable for closed area flow. A reduced version of Darcy's law for laminar flow is obtained in Equation 3.10 as actual velocity component ( $U$ ) is written in terms of inverse of the resistance tensor ( $R$ ) and pressure gradient.

$$U = -R^{-1}\nabla P \quad (3.10)$$

Where the gradient of pressure is written as for single dimension:

$$\frac{dP}{dx} \approx \frac{\Delta P}{\Delta L} \quad (3.11)$$

The relationship between velocity and pressure for selected two points in Figure 3.1 expressed with Bernoulli Equation. Assuming the potential energy terms for chosen points are equal to each other since there is no change in the downstream and upstream surface of fence region  $\mu_1=\mu_2=\mu$ :

$$P_1 + \frac{1}{2}\rho_1 u_1^2 = P_2 + \frac{1}{2}\rho_2 u_2^2 \quad (3.12)$$

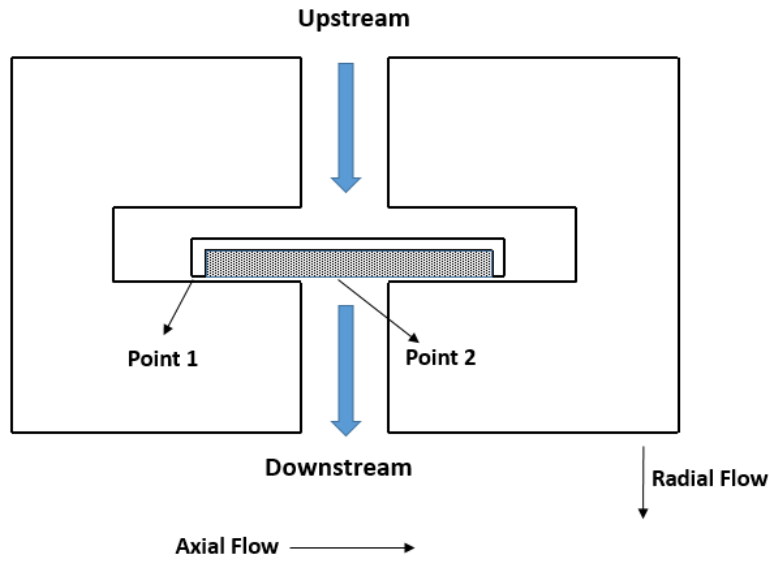


**Figure 3.1: Selected points in choking line (point 1) and downstream of cloth seal (point 2)**

As flow encounters with woven fibers which have high flow resistance, fluid moves toward the clearance region. For that reason, the stagnation point is assumed at Point 1 so axial velocity can be assumed as zero.

$$P_1 - P_2 = \frac{1}{2}\rho u_2^2 \quad (3.13)$$

As pressure difference illustrated as  $P_1 - P_2 = \Delta P$  and velocity for second point is formulated as:

$$u_2 = \sqrt{\frac{2\Delta P}{\rho}} \quad (3.14)$$

$V_2$  is related to density and rate of change in pressure. Assuming that actual velocity refers to average velocity, Equation (3.10) is modified as:

$$u = \frac{u_1+u_2}{2} \approx \frac{V_2}{2} \quad (3.15)$$

$$\frac{u_2}{2} = -R^{-1}\nabla P \quad (3.16)$$

Combining Equation (3.10), (3.11), (3.14) and (3.16) shows that resistance coefficients depend on density, rate of change of pressure and pack thickness.

$$\sqrt{\frac{\Delta P}{2\rho}} = -R^{-1} \frac{\Delta P}{\Delta L} \quad (3.17)$$

$$R = \frac{-\Delta P}{\Delta L} \sqrt{\frac{2\rho}{\Delta P}} \quad (3.18)$$

$$R = \frac{-1}{\Delta L} \sqrt{2\rho\Delta P} \quad (3.19)$$

For simplicity, density is converted pressure proportional to specific gas constant and temperature according to Ideal Gas Law. A modified version of Equation 3.19 with Ideal Gas Law is shown in Equation 3.21:

$$\text{Ideal Gas Law} \Rightarrow \rho = \frac{P}{R_c T} \quad (3.20)$$

$$R = \frac{1}{\Delta L} \sqrt{\frac{P_{avg} \Delta P}{R_c T}} \quad (3.21)$$

The resistance coefficient value is depending on average pressure ( $P_{avg}$ ) rate of change of pressure ( $\Delta P$ ), specific gas constant ( $R_c$ ) and temperature ( $T$ ). Resistance coefficients are calculated for current cloth seal with respect selected reference point as:

$$R_{cur} = R_{ref} \frac{\Delta L_{ref}}{\Delta L_{cur}} \sqrt{\frac{P_{avg(cur)} \Delta P_{cur} R_{c(ref)} T_{ref}}{P_{avg(ref)} \Delta P_{ref} R_{c(cur)} T_{cur}}} \quad (3.22)$$

One can give  $R_{cur}$  as an expression in preprocessing stage of CFD analysis. Calibrated CFD analysis with test results can be considered as a reference state. Therefore, leakage tests are needed for determining the base point. One limitation of this approach is only considering viscous forces by neglecting inertial terms. For this reason, this approach is suitable for laminar flows. In addition, frictional losses due to porous

region need to be included additionally. Moreover, this approach assumes that the resistance coefficients in different directions are changed in the same way.

### 3.2.2 Pressure Drop – Velocity

A non-Darcian porosity model is expressed in Equation 3.8. The equation can be expressed for a porous length as:

$$-S_{M,i} = -\frac{\Delta P}{\Delta L} = (\alpha_i |u_i| + \beta_i) u_i \quad (3.23)$$

If upstream and downstream pressure and mass flow rate are measured at a range, a second-order function can be fitted between pressure drop and superficial velocity (or velocity by multiplying porosity with superficial velocity). In order to obtain velocity, the measured mass flow rate can be used as:

$$u = \frac{\dot{m}}{\rho A} \quad (3.24)$$

A second order curve can be fit between pressure drop in porous domain and velocity. An example of the curve fitting method is shown in Figure 3.2.

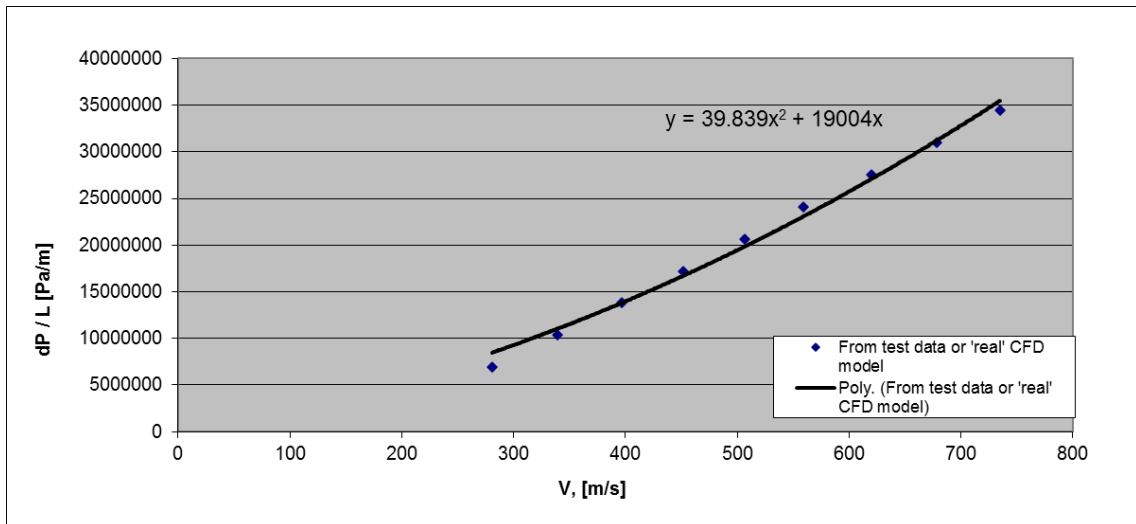


Figure 3.2: An example of curve fitting between pressure drop and velocity [53]

As a result, a quadratic equation can be fitted for each cloth weave design and various directions. This equation can be used to estimate resistance coefficients in the operating conditions that leakage test result does not exist.

### 3.2.3 Sutherland-Ideal Gas Approach

The non-Darcian equation in Equation 3.9 shows that viscous (linear) term is linearly correlated with viscosity whereas inertial (quadratic) term is linearly changing with respect to density. The density varies with pressure and temperature, while the viscosity is only a function of temperature. Therefore, the dependency of flow resistance coefficients on pressure and temperature should be considered in the calculation and calibration of  $\alpha$  and  $\beta$ .

The inertial flow resistance coefficient ( $\alpha$ ) is a function of density that varies with pressure and temperature. Therefore, in the calibration of the flow resistance coefficients, the inertial resistance (quadratic) coefficient is correlated with respect to pressure and temperature by using the Ideal Gas equation.

Meanwhile, the viscous flow resistance coefficient ( $\beta$ ) is a function of viscosity that varies with temperature. Therefore, the viscous resistance (linear) coefficient is correlated with respect to temperature by applying Sutherland's Law [54].

Thus, Sutherland's Law and the Ideal Gas equation are employed in the calibration of the flow resistance coefficients for the porous metallic-cloth fibers. The equations showing the dependency of the inertial/viscous flow resistance coefficient on pressure and temperature are written below:

$$\frac{\alpha_1}{\alpha_2} = \frac{\rho_1}{\rho_2} = \frac{P_1 T_2}{P_2 T_1} \quad (3.25)$$

$$\frac{\beta_1}{\beta_2} = \frac{\mu_1}{\mu_2} = \frac{T_1^{3/2} T_2 + S}{T_2^{3/2} T_1 + S} \quad (3.26)$$

S refers to the Sutherland temperature. These equations provide a correlation for the resistance coefficients for different pressures and temperatures.

At the end of the calibration procedure, a single number is defined for  $\alpha$  and  $\beta$ , while the pressure/temperature dropped from  $P_1/T_1$  to  $P_2/T_2$  over the metallic-cloth fibers.  $P_1$  and  $P_2$  are conducted for various pressure levels as:

$$P_1 = P_{u1}(1 - C_{down}) + P_{d1}C_{down} \quad (3.27)$$

$$P_2 = P_{u2}(1 - C_{down}) + P_{d2}C_{down} \quad (3.28)$$

$P_{u1}$  and  $P_{u2}$  are upstream pressure and  $P_{d1}$  and  $P_{d2}$  are downstream pressure of first and second case points.  $C_{down}$  is a pressure constant that enables correlating the resistance coefficients at different pressure levels.  $C_{down} = 1$  indicates that the downstream pressure levels are considered in the correlation, whereas the  $\alpha$  and  $\beta$  resistance coefficients are correlated with the average pressure levels if  $C_{down} = 0.5$ .

### 3.2.4 Ergun's Equation

Ergun's equation [55] illustrates friction factor in a packed column with respect to Reynolds number. Ergun's equation is expressed as:

$$\frac{\Delta p}{L} = \frac{150\mu}{D_p^2} \frac{(1 - \varepsilon)^2}{\varepsilon^3} v + \frac{1.75\rho}{D_p} \frac{(1 - \varepsilon)}{\varepsilon^3} v^2 \quad (3.29)$$

$\varepsilon$  is the porosity and  $D_p$  refers to equivalent spherical diameter of packing. 150 and 1.75 are model constants which are obtained experimentally. Such values may be changed with test correlations. These are dependent on the turbulence level of the fluid. Akgiray and Saatci [56] developed Ergun's equation to be applied in fluidized beds. Ergun Equation was applied by Wu et. al. [57] in order to obtain flow resistance of Dutch weave and other types of woven meshes. Several studies have been done to evaluate aperture size of Dutch weave [58]-[60]. However, aperture structure and size of the determined cloth weave are difficult to determine since it is sensitive to manufacturing and weave tolerances, applied pressure, offset and mismatch levels.

### 3.3 Cloth Weave Properties

#### 3.3.1 Porosity

Volume porosity is the ratio of the volume of voids over the total volume comprised of the boundaries of the woven fibers. In cloth weave, porosity is mainly dependent on weave type, density&diameter of warp cloth metal, density&diameter of shute cloth metal. In order to decrease cloth porosity, wire size needs to be diminished. However, reducing fiber size decreases cloth thickness which means limited oxidation and wear life [9].

The main objective in developing an analytical model for volume porosity is to determine a relation between volume porosity and geometry as a function of weave type, weave density, the diameters of warp and shute fibers, etc. This section covers a volume porosity model which is applicable for plain and twill weave.

Volume porosity 'ε' is calculated for a woven fabric in Equation 3.30. Volume covered by fibers and total encompassed volume are expressed in Equation 3.31&3.32, respectively.  $D_w$ ,  $L_w$ ,  $n_w$  denote the diameter, length and number of warp fibers respectively.  $D_s$ ,  $L_s$ ,  $n_s$  indicate diameter, length and number of shute fibers respectively.  $L_f$ ,  $T_f$ ,  $H_f$  are overall length, thickness, and height of woven fabric sample respectively.

$$\varepsilon = 1 - \left( \frac{V_{metal}}{V_{total}} \right) \quad (3.30)$$

$$V_{metal} = \frac{\pi D_w^2 L_w n_w + \pi D_s^2 L_s n_s}{4} \quad (3.31)$$

$$V_{total} = L_c W_c H_c \quad (3.32)$$

Combining Equation 3.30 with Equation 3.31&3.32 brings as:

$$\varepsilon = 1 - \left( \frac{\pi D_w^2 L_w n_w + \pi D_s^2 L_s n_s}{4 L_c W_c H_c} \right) \quad (3.33)$$

Width of cloth weave is also calculated, in ideal condition, as the summation of one warp, two shute cloth diameters and two g values that shown in Equation 3.34. g is the gap between warp and shute fibers resulting from bending over each other. It is considered while calculating total cloth weave width. Since g is unknown and can vary from

geometry to geometry, it may be correlated with experimentally calculated porosity which is obtained from weight and volume of cloth weave sample. In another way, height of cloth weave can be measured, and  $g$  can be obtained

$$W_c = D_w + 2D_s + 2g \quad (3.34)$$

In both plain and twill weave, warp fibers are straight, therefore the length of warp fibers is assumed to equal to length of woven fabric sample. However, shute fibers are bent and their actual length needs to be determined. The geometry of plain weave is illustrated in Figure 3.3 and shute wire length per inch for plain weave is represented in Equation 3.35.

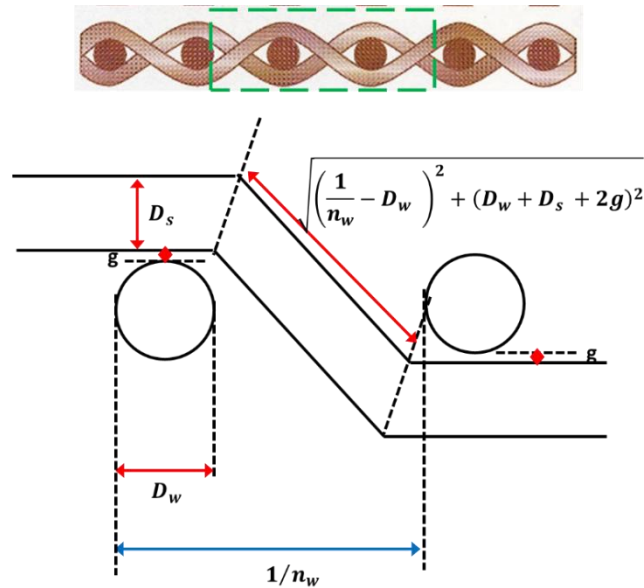


Figure 3.3: Shute wire length calculations for plain weave

$$Plain\ weave \Rightarrow L_{spi} = D_w n_w + n_w \sqrt{\left(\frac{1}{n_w} - D_w\right)^2 + (D_w + D_s + 2g)^2} \quad (3.35)$$

The geometry of twill weave is shown in Figure 3.4. For twill weave, shute wire length per inch is calculated in Equation 3.36.

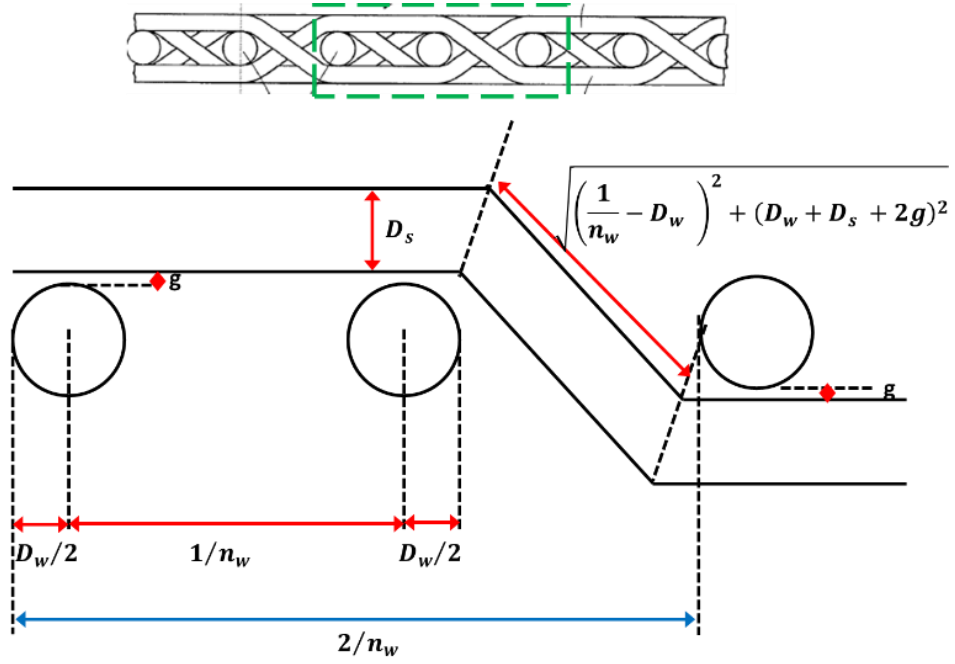


Figure 3.4: Shute wire length calculations

$$Twill\ weave \Rightarrow L_{spi} = \frac{1 + D_w n_w + n_w \sqrt{\left(\frac{1}{n_w} - D_w\right)^2 + (D_w + D_s + 2g)^2}}{2} \quad (3.36)$$

Usually number of warp and number of shute fibers are presented by manufacturers as per inch. In order to simplify the volume porosity equation, it is represented for a 1x1 inch sample in Equation 3.37.  $n_{wpi}$  denotes the number of warp fibers per inch whereas  $n_{spi}$  refers to the number of shute fibers per inch.

$$\varepsilon = 1 - \left( \frac{\pi D_w^2 L_{wpi} n_{wpi} + \pi D_s^2 L_{spi} n_{spi}}{4 L_{fpi} H_{fpi} (D_w + 2D_s + 2g)} \right) \quad (3.37)$$

$L_{wpi} = L_{fpi} = H_{fpi} = 1$  inch. Therefore, the generalized volume porosity equation is expressed as:

$$\varepsilon = 1 - \left( \frac{\pi D_w^2 n_{wpi} + \pi D_s^2 L_{spi} n_{spi}}{4(D_w + 2D_s + 2g)} \right) \quad (3.38)$$

The equations are shown above; prove realistic volume porosity value of the plain and twill woven fabric.

### 3.3.2 Tortuosity & Surface Area to Unit Volume Ratio

Tortuosity is a property of a curve being twisted. A flow becomes more tortuous if it has many turns. It is commonly used to describe diffusion and fluid flow in porous medium. The simplest equation for tortuosity is the flow path divided by shortest path Figure 3.5. Different equations represent tortuosity for a porous medium consisting of 2D square solid particles or a fixed bed of randomly packed identical particles [61],[62].

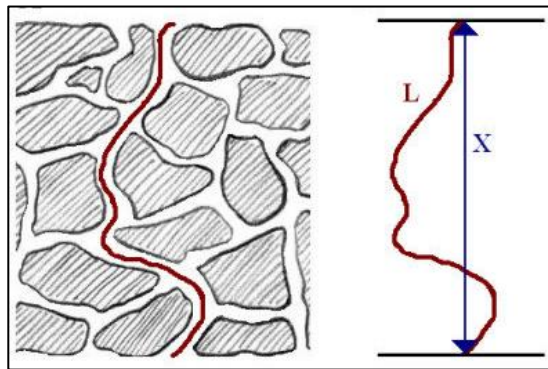


Figure 3.5: A representation of tortuous flow path

Tortuosity is calculated from geometry for Dutch Twill [63]. Geometry of Dutch twill is illustrated in

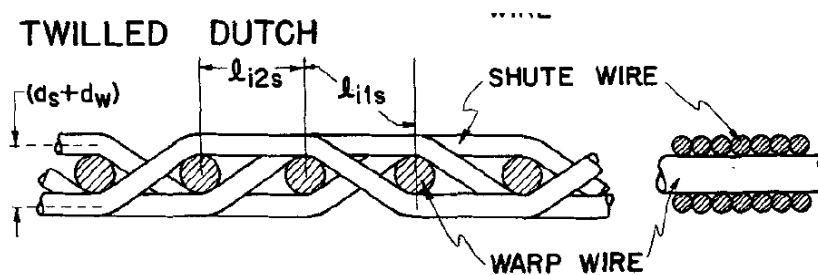


Figure 3.6: Cross-sectional views of Dutch twill weave [63]

The tortuosity of Dutch twill is calculated from the ratio average path and shortest path through plane. It is calculated as 1.28.

$$\text{Shortest Path} \Rightarrow L_{short} = 2 d_s + d_w \quad (3.39)$$

$$\text{Longest Path} \Rightarrow L_{long} = \pi d_s + \pi \frac{d_w}{2} \quad (3.40)$$

$$Tortuosity = \frac{Average Path}{Shortest Path} = \frac{2d_s + d_w + (\pi d_s + \pi \frac{d_w}{2})}{2(2d_s + d_w)} = \frac{\frac{\pi}{2} + 1}{2} = 1.28 \quad (3.41)$$

Surface area to unit volume ratio is used while calculating heat transfer in porous medium. It affects the convective heat transfer between fluid and solid parts of cloth weave region. For Dutch twill, it is expressed as [63]:

$$Surf. Vol. Ratio = \frac{\pi}{2d_s + d_w} [n_w d_w + \frac{1}{2} n_s d_s + \frac{1}{2} n_s n_w d_s l_{i2s}] \quad (3.42)$$

### 3.4 Equivalent Gap Calculation

In order to compare the leakage performance of the different seal design combinations under different pressure conditions better, leakage rates are converted to equivalent sealing gap values and plotted in many figures. The equivalent gap is a representative gap that decreases with better sealing performance. It is calculated by the following equation [9], [64]:

$$Eq. Gap = \frac{\dot{m} \sqrt{T_{high} + 460}}{P_{high} \cdot L \cdot FF} \quad (3.43)$$

where  $\dot{m}$  is the leakage flow rate, L is cloth seal length,  $T_{high}$  and  $P_{high}$  represent upstream temperature and pressure, respectively. FF refers to the 'Flow Function' which is calculated with different equations for choked and unchoked flow:

For choked flow:

$$FF = \sqrt{\frac{g\gamma}{R}} \sqrt{\left(\frac{2}{\gamma + 1}\right)^{(\gamma+1)/(\gamma-1)}} \quad (3.44)$$

For unchoked flow:

$$FF = \sqrt{\frac{g\gamma}{R}} \sqrt{\frac{2}{\gamma - 1} \left[ \left(\frac{P_{high}}{P_{low}}\right)^{-(\gamma+1)/\gamma} \right] \left[ \left(\frac{P_{high}}{P_{low}}\right)^{(\gamma-1)/\gamma} - 1 \right]} \quad (3.45)$$

where g is the acceleration due to gravity,  $\gamma$  refers to specific heat ratio, R is gas constant.

### 3.5 Uncertainty Analysis

Uncertainty analysis is done to evaluate the fluctuation level of measurements during experiments. Fluctuation level is defined as error which is the difference between measured value and true value. Since true value is unknown, several methods are developed to estimate it. Error is also defined based on an approach to reach true value.

The quality of measurement is named as accuracy and is usually presented in datasheets. However, test conditions are specific for each application and uncertainty level is affected by ambient conditions, calibration of measurement tools, fluctuation of measured system or boundary conditions, etc. Therefore, Type A and Type B uncertainty measurements are applied to determine the level of error of measurement.

Type A is obtained by repeated experiment results under the same conditions. First of all, average of measurement results is calculated.

$$\bar{x} = \frac{\sum_{i=1}^n x_i}{n} \quad (3.46)$$

$$R_i = (x_i - \bar{x}) \quad (3.47)$$

$R_i$  is the estimation for true value which equals to the difference between measured value of  $i^{\text{th}}$  test and average test result. Standard deviation is calculated as below:

$$s = \sqrt{\frac{\sum_{i=1}^n (x_i - \bar{x})^2}{n - 1}} \quad (3.48)$$

In order to reach Type A uncertainty, standard deviation is divided by square root of number of measurements.

$$u_a = \frac{s}{\sqrt{n}} \quad (3.49)$$

Type B uncertainty is obtained by accuracy (a) value given in datasheet of measurement equipment.

$$u_b = \frac{a}{\sqrt{3}} \quad (3.50)$$

Combined uncertainty is reached from the calculated Type A and Type B uncertainty levels by using the formula given below.

$$u_c = \sqrt{u_a^2 + u_b^2} \quad (3.51)$$

The combined uncertainty provides the uncertainty level equivalent to one standard deviation (68% level of confidence). To raise the level of confidence, the combined uncertainty is multiplied by a coverage factor (k), and this provided the expanded uncertainty. In this study, k = 3 for a confidence level of 99.7%.

$$u_e = ku_c \quad (3.52)$$

In the standard deviation curve, if standard deviation is multiplied by two, %95.5 probability is obtained whereas if standard deviation is multiplied by three, %99.7 probability is reached. Same probability values are also valid for the confidence level calculation of a measurement. Mostly, the coverage factor is selected two or three or a value between two and three.

Uncertainty measurements are important to compare fluctuations in test system with accuracy provided by supplier. The uncertainty levels for the cloth seal and warp, shute, diagonal, and cross directions of cloth weave leakage tests are illustrated in Section 4.4 for 68.9–758.4 kPad (10–110 psid) pressure differences.

### **3.6 Reynolds Averaged Navier-Stokes Equations with Standard K-Epsilon Model**

A turbulence model applies a procedure to close the system of mean flow equations. Several turbulence models solve an updated version of Navier-Stokes equations by separating averaged and fluctuating of components. Based on Reynolds Averaged Naviers-Stokes (RANS), the terms are separated into average and fluctuating components. As an example, velocity ( $U_i$ ) is expressed in terms of averaged ( $\bar{U}_i$ ) and fluctuating ( $u_i$ ) components as:

$$U_i = \bar{U}_i + u_i \quad (3.53)$$

$$\bar{U}_i = \frac{1}{\Delta t} \int_t^{t+\Delta t} U_i dt \quad (3.54)$$

$\Delta t$  is a time scale the larger than fluctuations of turbulence and smaller than solution time scale. The instantaneous Navier-Stokes equations are averaged with additional terms when flow is considered as turbulent. The Reynolds Averaged Navier Stokes equations are given as:

*The Continuity Equation for RANS*

$$\frac{\partial \rho}{\partial t} + \frac{\partial}{\partial x_j} (\rho U_j) = 0 \quad (3.55)$$

*The Momentum Equation for RANS*

$$\frac{\partial \rho U_i}{\partial t} + \frac{\partial}{\partial x_j} (\rho U_i U_j) = -\frac{\partial P}{\partial x_i} + \frac{\partial}{\partial x_j} (\tau_{ij} - \rho \overline{u_i u_j}) + S_M \quad (3.56)$$

*The Energy Equation for RANS*

$$\frac{\partial \rho h_{tot}}{\partial t} - \frac{\partial P}{\partial t} + \frac{\partial}{\partial x_j} (\rho U_j h_{tot}) = \frac{\partial}{\partial x_j} \left( \lambda \frac{\partial T}{\partial x_j} - \rho \overline{u_j h} \right) + \frac{\partial}{\partial x_j} [U_i (\tau_{ij} - \rho \overline{u_i u_j})] + US_M + S_E \quad (3.57)$$

where  $\tau$  is molecular stress tensor. In addition to the molecular diffusive fluxes, turbulent flux term is added as Reynolds stresses  $\rho \overline{u_i u_j}$ .

The k- $\epsilon$  turbulence model was used and validated the turbulence model in similar CFD analyses [51]. The k- $\epsilon$  model focuses on the mechanisms that k is turbulent kinetic energy (per unit mass) and  $\epsilon$  is dissipation rate of k. The momentum equations are updated for k- $\epsilon$  turbulence model as:

$$\frac{\partial \rho U_i}{\partial t} + \frac{\partial}{\partial x_j} (\rho U_i U_j) = -\frac{\partial P'}{\partial x_i} + \frac{\partial}{\partial x_j} \left[ \mu_{eff} \left( \frac{\partial U_i}{\partial x_j} + \frac{\partial U_j}{\partial x_i} \right) \right] + S_M \quad (3.58)$$

$\mu_{eff}$  is the effective viscosity and  $P'$  is the modified pressure as shown below:

$$\mu_{eff} = \mu + \mu_t = \mu + C_\mu \rho \frac{k^2}{\epsilon} \quad (3.59)$$

$$P' = P + \frac{2}{3} \rho k + \frac{2}{3} \mu_{eff} \frac{\partial U_k}{\partial x_k} \quad (3.60)$$

The  $k$  and  $\varepsilon$  values are calculated from the differential transport equations of turbulence kinetic energy and turbulence dissipation rate.

### 3.7 Navier-Stokes Equations with Derived Equations for Porous Medium Flow

In this study, cloth weave is modeled with porous medium. Therefore, RANS equations are included additional momentum sink in porous cloth weave region by combining Equation 3.57 and 3.58 with Equation 3.9:

*The Momentum Equation in Porous Medium*

$$\frac{\partial \rho U_i}{\partial t} + \frac{\partial}{\partial x_j} (\rho U_i U_j) = -\frac{\partial P'}{\partial x_i} + \frac{\partial}{\partial x_j} \left[ \mu_{eff} \left( \frac{\partial U_i}{\partial x_j} + \frac{\partial U_j}{\partial x_i} \right) \right] - \alpha_i |u_i| u_i - \beta_i u_i \quad (3.61)$$

*The Total Energy Equation in Porous Medium*

$$\begin{aligned} \frac{\partial \rho h_{tot}}{\partial t} - \frac{\partial P}{\partial t} + \frac{\partial}{\partial x_j} (\rho U_j h_{tot}) \\ = \frac{\partial}{\partial x_j} \left( \lambda \frac{\partial T}{\partial x_j} - \rho \overline{u_j h} \right) + \frac{\partial}{\partial x_j} [U_i (\tau_{ij} - \rho \overline{u_i u_j})] - U_i (\alpha_i |u_i| u_i \\ + \beta_i u_i) + S_E \end{aligned} \quad (3.62)$$

The porosity equation derived in Equation 3.38 is also included in RANS equations:

*The Momentum Equation in Porous Medium with Derived Porosity Equation*

$$\begin{aligned} \frac{\partial \rho U_i}{\partial t} + \frac{\partial}{\partial x_j} (\rho U_i U_j) \\ = -\frac{\partial P'}{\partial x_i} + \frac{\partial}{\partial x_j} \left[ \mu_{eff} \left( \frac{\partial U_i}{\partial x_j} + \frac{\partial U_j}{\partial x_i} \right) \right] \\ - \alpha_i \left| \frac{u}{1 - \left( \frac{\pi D_w^2 n_{wpi} + \pi D_s^2 L_{spi} n_{spi}}{4(D_w + 2D_s + 2g)} \right)} \right| \frac{u}{1 - \left( \frac{\pi D_w^2 n_{wpi} + \pi D_s^2 L_{spi} n_{spi}}{4(D_w + 2D_s + 2g)} \right)} \\ - \beta_i \frac{u}{1 - \left( \frac{\pi D_w^2 n_{wpi} + \pi D_s^2 L_{spi} n_{spi}}{4(D_w + 2D_s + 2g)} \right)} \end{aligned} \quad (3.63)$$

*The Total Energy Equation in Porous Medium with Derived Porosity Equation*

$$\begin{aligned}
& \frac{\partial \rho h_{tot}}{\partial t} - \frac{\partial P}{\partial t} + \frac{\partial}{\partial x_j} (\rho U_j h_{tot}) \\
&= \frac{\partial}{\partial x_j} \left( \lambda \frac{\partial T}{\partial x_j} - \rho \overline{u_j h} \right) + \frac{\partial}{\partial x_j} [U_i (\tau_{ij} - \rho \overline{u_i u_j})] \\
&+ U_i \alpha_i \left[ \frac{u}{1 - \left( \frac{\pi D_w^2 n_{wpi} + \pi D_s^2 L_{spi} n_{spi}}{4(D_w + 2D_s + 2g)} \right)} \right] \frac{u}{1 - \left( \frac{\pi D_w^2 n_{wpi} + \pi D_s^2 L_{spi} n_{spi}}{4(D_w + 2D_s + 2g)} \right)} \\
&- \beta_i \frac{u}{1 - \left( \frac{\pi D_w^2 n_{wpi} + \pi D_s^2 L_{spi} n_{spi}}{4(D_w + 2D_s + 2g)} \right)} + S_E
\end{aligned} \tag{3.64}$$

Three-dimensional Navier-Stokes equations for porous medium (Equation 3.55, 3.63 and 3.64) are used in CFD analyses to analyze flow through cloth weave. Equation 3.55, 3.58 and 3.57 which are applied in the flow domains except for porous medium, are the continuity, momentum and energy equations, respectively. These equations are for k-ε turbulence model and iteratively solved until reaching a converged solution.

### 3.8 Equations of State

The constitutive equations for enthalpy and density are defined. The differential of enthalpy is expressed in terms of pressure (p), temperature (T) and heat capacity at constant pressure (C<sub>p</sub>) as:

$$\partial h = \left( \frac{\partial h}{\partial T} \right)_p \partial T + \left( \frac{\partial h}{\partial p} \right)_T \partial p = C_p \partial T + \left( \frac{\partial h}{\partial p} \right)_T \partial p \tag{3.65}$$

In flow analysis, the air is assumed as ideal gas since the compressibility factor of air is near to 1 in defined analysis conditions (Appendix C). For ideal gas, the enthalpy is independent of its pressure and it only depends on temperature. Therefore, enthalpy is calculated with respect to temperature.

$$\partial h = C_p \partial T \tag{3.66}$$

The density is calculated from the Ideal Gas Equation as:

$$\rho = \frac{wP_{abs}}{R_0T} \quad (3.67)$$

$P_{abs}$  is the absolute pressure,  $w$  is the molecular weight and  $R_0$  is the universal gas constant.

## 4 EXPERIMENTAL SETUP

In order to obtain the cloth seal leakage performance, the leakage tests need to be conducted in gas turbine operating conditions. However, it is challenging to set up a test system that works under extreme pressure and temperature levels. Similar to previous studies [9],[10], leakage test rigs are designed to operate at room temperature. The downstream regions open to the atmosphere. The pressure drop levels are selected to cover typical pressure drop levels of a modern gas turbine.

Static leakage flow tests have been performed to determine the leakage rate. The experimental study consists of two different stages. First test stage is established to measure the leakage rate of cloth weave in warp, shute and diagonal and cross directions. Cloth weave tests are performed and compared with CFD analyses to correlate porous medium resistance coefficients in each direction. Second test stage is used to find leakage rate of several cloth seal designs (includes cloth weave and metal shim layers). The results of cloth seal leakage tests are conducted with a DoE study and CFD analyses. The leakage tests are repeated three times and the average value of the leakage rate is considered. Both test systems are available to work under different upstream pressure conditions.

### 4.1 Cloth Weave Test Rig

To calibrate resistance coefficients in CFD analyses, experiments have been completed with pre-determined inlet and outlet boundary conditions.

Two test rigs as shown in Figure 4.1 and Figure 4.2 are set up to measure the cloth weave leakage in the four directions of warp, shute, diagonal, and cross. Cloth weave holders are designed to obtain the leakage flow in the determined directions. For this purpose, two different cloth weave holders are used. An in-plane cloth weave test system is used to obtain the leakage in the warp, shute, and diagonal directions, whereas an out-of-plane test system provided the leakage rate in the cross direction. Similar test rigs are also used in previous works [7],[10]. In Figure 4.1, two side holders are shown for the in-plane test rig. The holders are disassembled, and a circular holder is assembled for the out-of-plane test rig. The system includes ball and globe valves, flowmeter, pressure

transducer, upstream chamber and holders. The ball valve is only used at the beginning and end of the test cycle to allow or halt fluid flow. The globe valve serves precise control for upstream pressure. Upstream pressure sensor is connected to a DAQ system. An interface is generated in a commercial software to read measurements. Leakage rate and pressure levels are recorded via computer. Upstream chamber provides more homogenous pressure distribution, consequently, the oscillations of pressure on upstream side of cloth weave are reduced. Connecting surfaces of components are siliconized, therefore, secondary undesired leakage is prevented. Four cloth samples are prepared for the warp, shute, diagonal, and cross leakage tests.

The test rig operated at pressure drop levels between 68.9 and 758.4 kPad (10–110 psid). The air temperature is at room temperature. During the cloth weave leakage tests, the pressure difference is increased up to 758.4 kPad (110 psid) and then decreased down to 68.9 kPad (10 psid) incrementally. The leakage flow rate is recorded at any 68.9 kPad (10 psid) increment. The tests are repeated for three cycle times for each direction. Each cycle included increasing and decreasing the pressure and upward and downward leakage measurements.

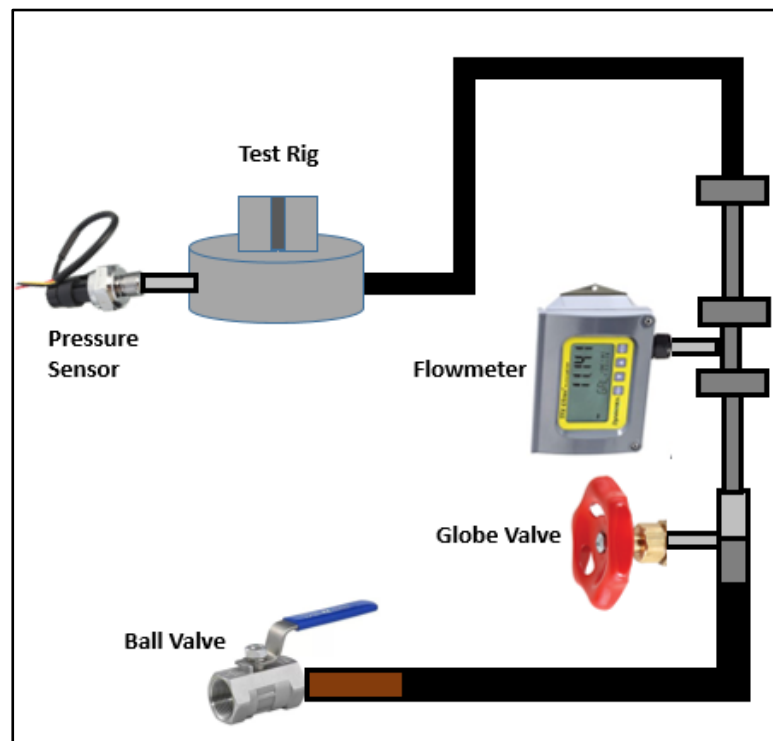


**Figure 4.1: Connections and components of the in-plane test rig**

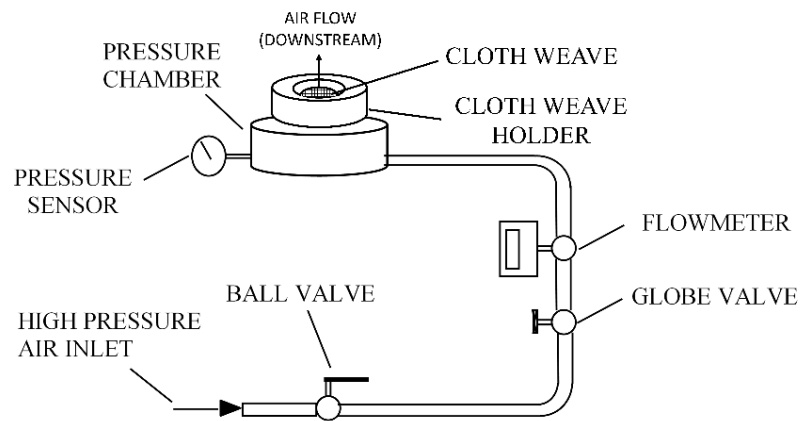


**Figure 4.2: Schematic and connections of the out-of-plane test rig**

#### **4.1.1 In-plane Cloth Weave Test Setup**

For in-plane test setup, cloth weave samples are cut with 100x20 mm dimensions. Dimensions and 90° corners are determined with the aid of a miter and ruler. White silicon remained from previous test is removed with acetone and brake cleaner. A screwdriver is used to scrape silicone residue off holders and bottom plate. Areas for siliconizing are marked with a marker pen. Yellow bands are pasted around silicon area in order not to slop. After specified regions are siliconized, yellow bands are removed. A piece of cloth weave is located upside of a holder and siliconized 5 mm in short edges. Therefore, the leakage flow area is decreased to 90x20 mm during tests. Another holder is pasted with silicone to cloth weave. Six M6 bolts and nuts are used to fasten holders.

Before starting each test, pressure chamber is cleaned with pressurized air to remove residue which is remained from previous tests. Upper surface of pressure chamber is also siliconized in order to eliminate leakage between components. Holders with cloth weave are pasted to pressure chamber and fastened with eight M8 bolts. Bottom plate and bottom platform are fastened with twelve M10 bolts. Each bolt is fastened with recommended tightening torque as shown in Appendix B. Pressure sensor is connected to pressure chamber, and upstream pressure is measured. Pressure sensor is connected to the DAQ system and power supply with cables. Collected pressure data are transferred to a computer and saved. Flow rate is also read from the flowmeter. Leakage between components is detected with leak detection spray.

#### 4.1.2 Out-of-plane Cloth Weave Test Setup

To remove silicone from a previous test, pressure chamber is cleaned from residuals with pressurized air. Acetone or brake cleaner is sprayed to rig components. Dry silicone is removed via scraper.

A piece of cloth weave is cut for out-of-plane direction leakage tests. Bottom cloth holder is also silicone from upper surface where the edges of cloth weave locate. The cloth weave is glued to bottom holder. After then, upper side of cloth weave is glued to upper holder. More than six hours are waited to dry silicone. Pressure chamber and cloth holders are fastened to each other with bolts. Undesired leakage (between components) is controlled with leak detector spray. After ensuring that there is no leakage between components, test starting procedure is applied.

Before and during leakage tests, following steps are applied:

- Air is compressed via compressor which can increase pressure level up to 1400 kPa.
- A dryer decreased humidity rate of air.
- The ball valve is opened. The globe valve is also opened. Fluid moves into upstream side of seals. Apart from seal region, leakage between components is checked via leak detector spray.
- The globe valve is closed. Upstream gauge pressure is waited to decrease 0 kPa. Afterward, the desired pressure level is achieved by calibrating the globe valve manually. Upstream pressure is checked from the software interface. Pressure difference is increased up to 758.4 kPad (110 psid) with 68.9 kPad (10 psid) increments. Such rising is called upcycle (or upward). After that, pressure difference is decreased from 758.4 kPad (110 psid) to 0 kPad which is named downcycle (or downward). In both upcycle and downcycle, pressure difference is calibrated, and leakage is measured in each 68.9 kPad (10 psid) increment.
- Leakage data is gained from the flowmeter. Figure 4.3-4.15 are generated according to specified upstream pressure. Post-test investigation provides the leakage rate and equivalent gap values for different weave direction and pressure drop.

## 4.2 Cloth Weave Leakage Measurements Results

A set of static leakage performance tests are done for 30x250 mesh density, Dutch twill cloth weave samples. Leakage flow rates are illustrated with respect to pressure drop on Figure 4.3 through Figure 4.18. Three repeated test cycles are conducted for each direction. Each cycle has upward and downward leakage measurements. The leakage values are normalized by dividing the leakage of the cross direction at the maximum pressure load of 758.4 kPad (110 psid)'s pressure drop. During upward direction, the globe valve is opened gradually, and pressure difference is increased with 68.9 kPad (10 psid) increments. The normalized leakage results of each cycle up to 758.4 kPad (110 psid) are illustrated.

### 4.2.1 Shute Direction

The leakage measurements for three cycles at eleven test points of shute direction are illustrated in Figure 4.3 through Figure 4.6. Upcycles are symbolized as dark blue rhombus whereas downcycles are represented as yellow squares. Results show that the leakage in shute direction is linearly increasing with respect to pressure drop. Variations between measurement cycles are small.

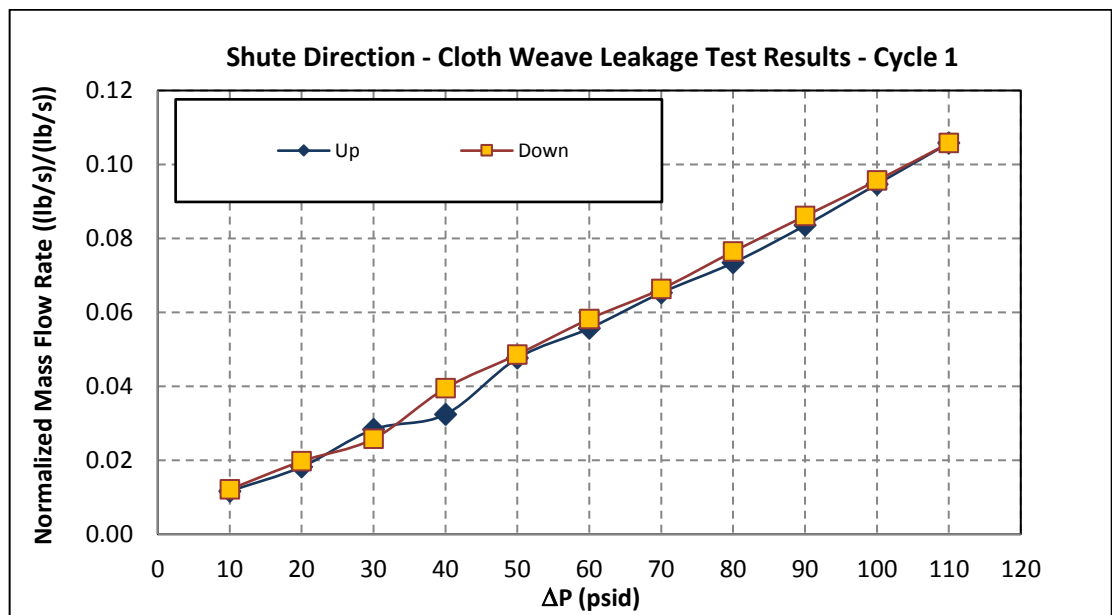


Figure 4.3: Shute direction cloth weave leakage test results – Cycle#1

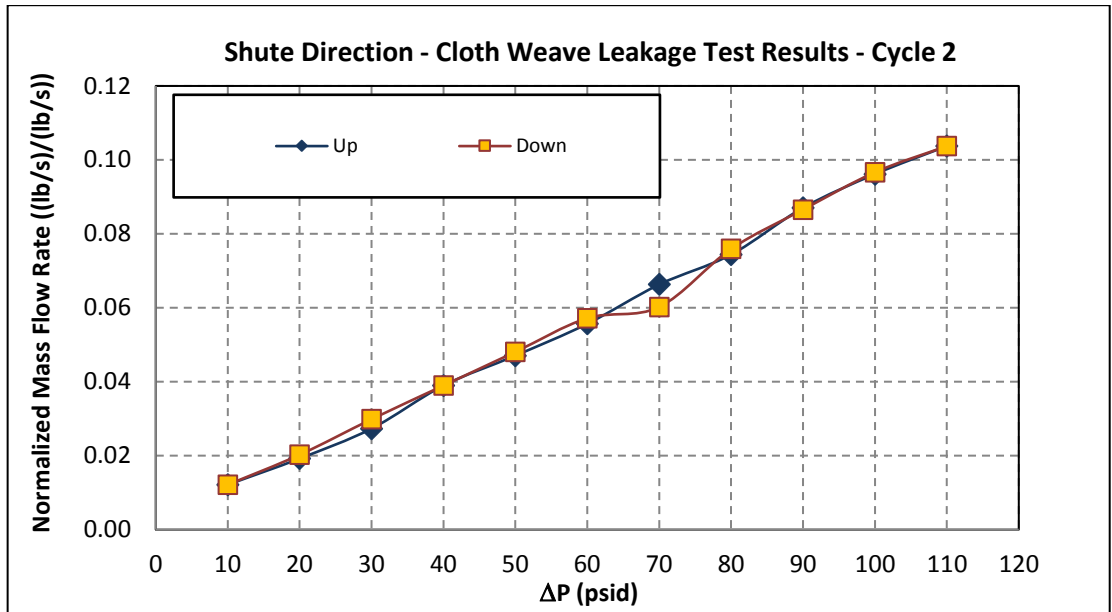


Figure 4.4: Shute direction cloth weave leakage test results – Cycle#2

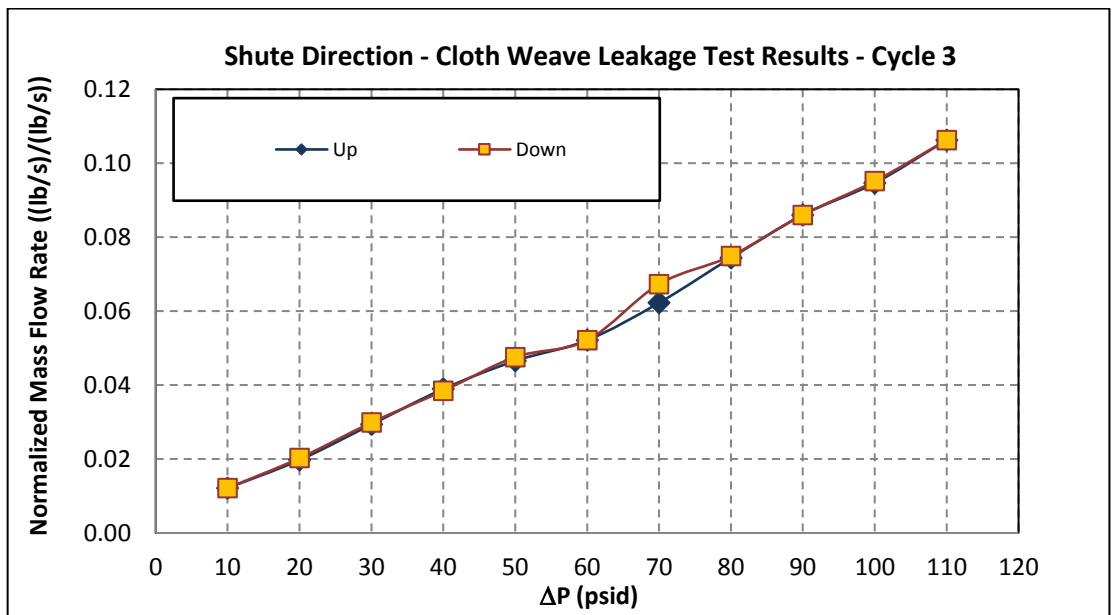


Figure 4.5: Shute direction cloth weave leakage test results – Cycle#3

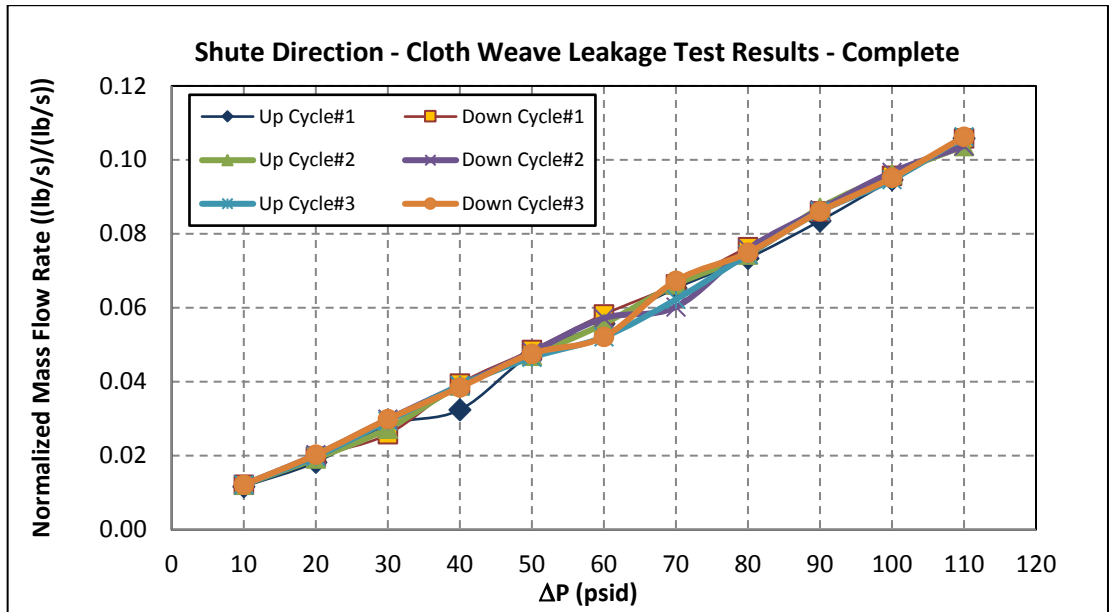


Figure 4.6: Shute direction cloth weave leakage test results – All results

#### 4.2.2 Warp Direction

The leakage measurements for three cycles at eleven test points of warp direction are illustrated in Figure 4.7 through Figure 4.10. Upcycles are symbolized as dark blue rhombus whereas downcycle are represented as yellow squares. Results show that the leakage in shute direction is linearly increasing with respect to pressure difference. Variations between measurement cycles are in an acceptable range.

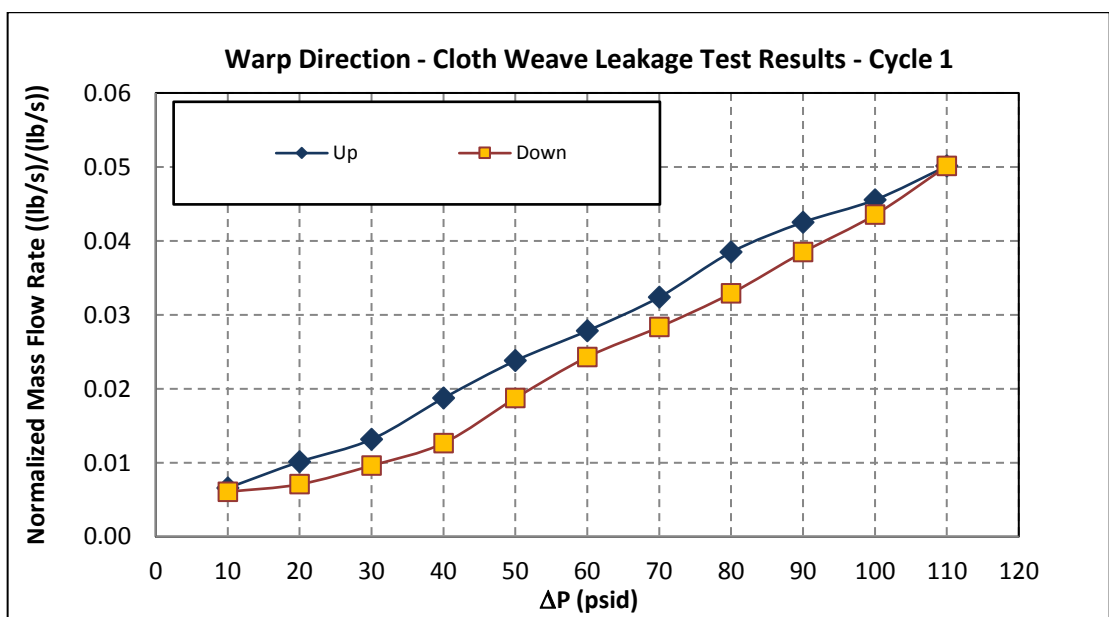


Figure 4.7: Warp direction cloth weave leakage test results – Cycle#1

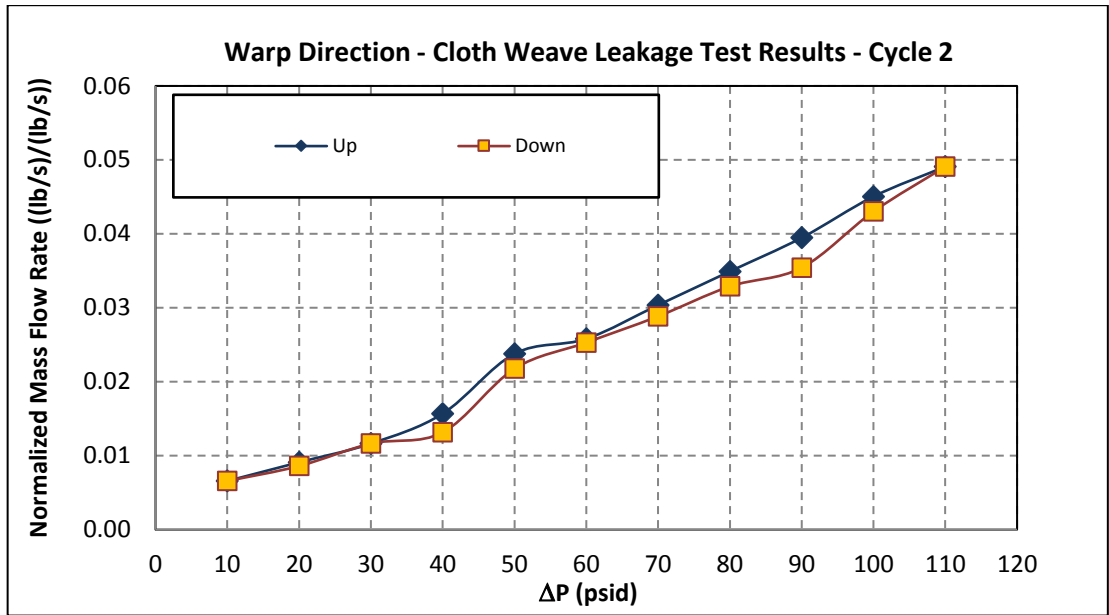


Figure 4.8: Warp direction cloth weave leakage test results – Cycle#2

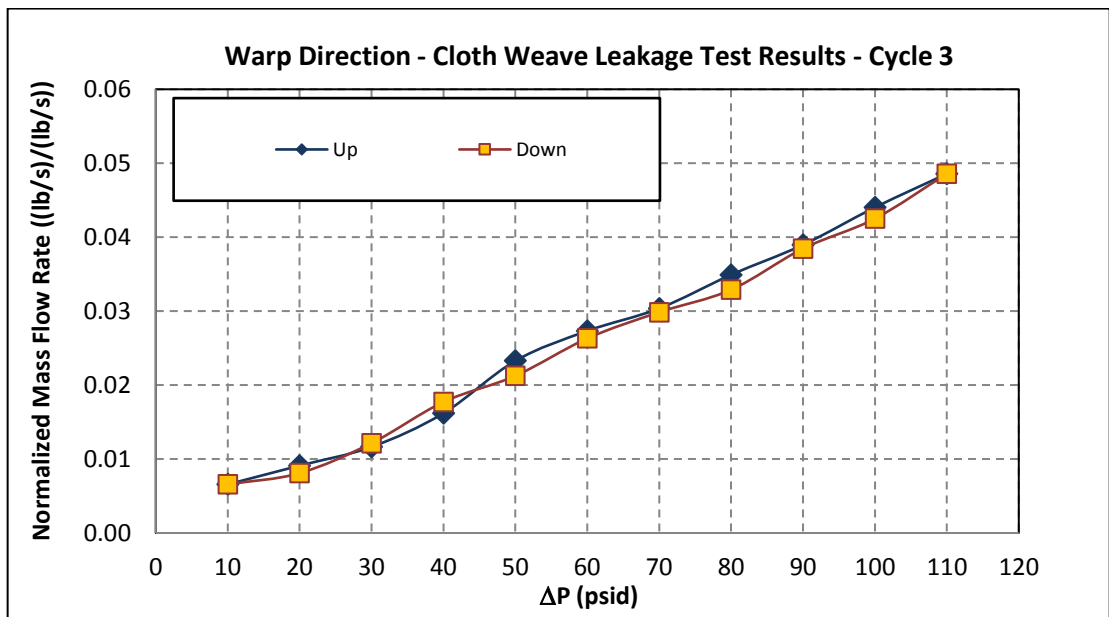


Figure 4.9: Warp direction cloth weave leakage test results – Cycle#3

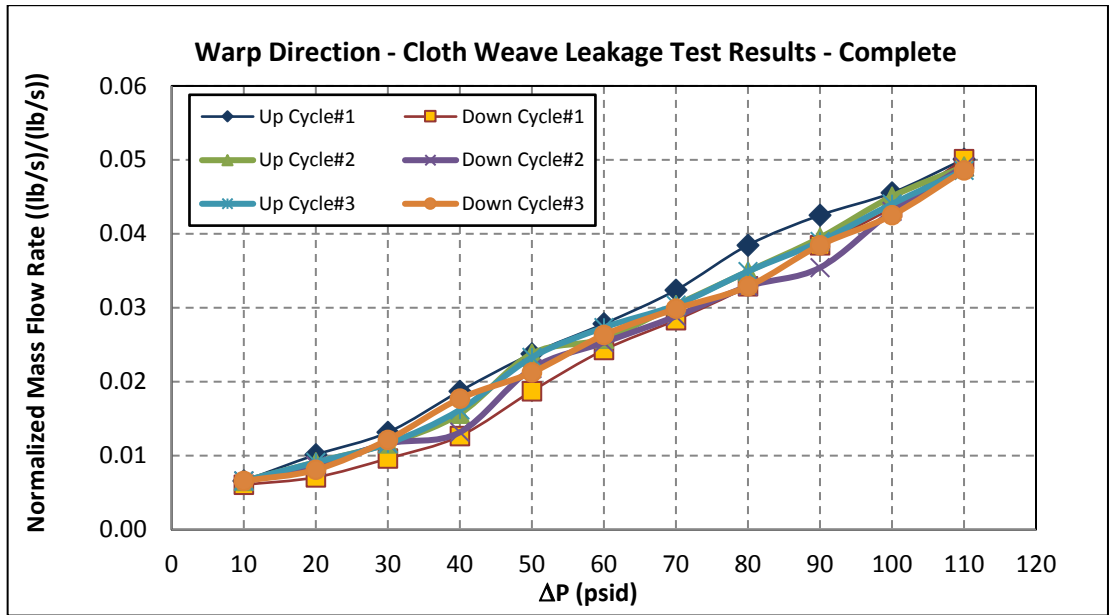


Figure 4.10: Warp direction cloth weave leakage test results – All results

### 4.2.3 Diagonal Direction

The leakage measurements for three cycles at eleven test points of diagonal direction are detailed from Figure 4.11 to Figure 4.14. Upcycles are symbolized as dark blue rhombus whereas downcycle are represented as yellow squares. Results show that the leakage in diagonal direction is increasing with respect to pressure difference. Variations between measurement cycles are in an acceptable range.

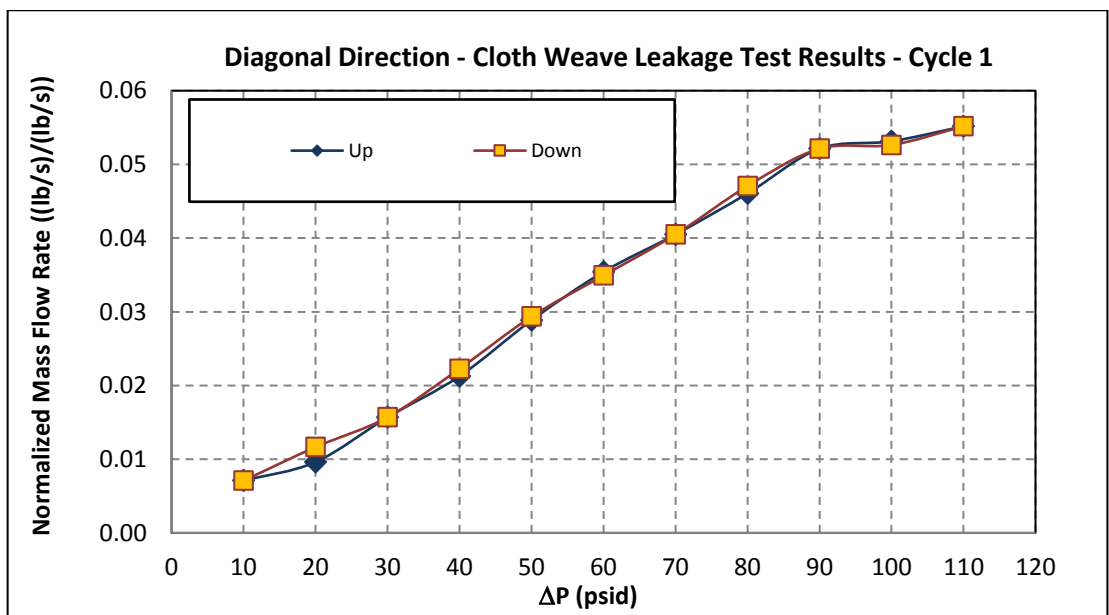


Figure 4.11: Diagonal direction cloth weave leakage test results – Cycle#1

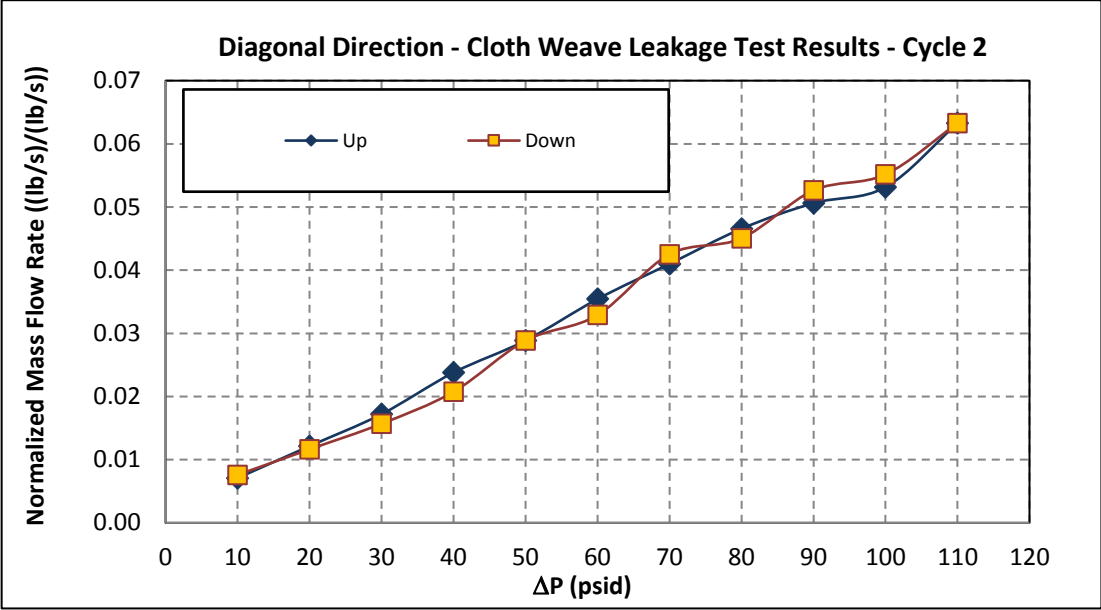


Figure 4.12: Diagonal direction cloth weave leakage test results – Cycle#2

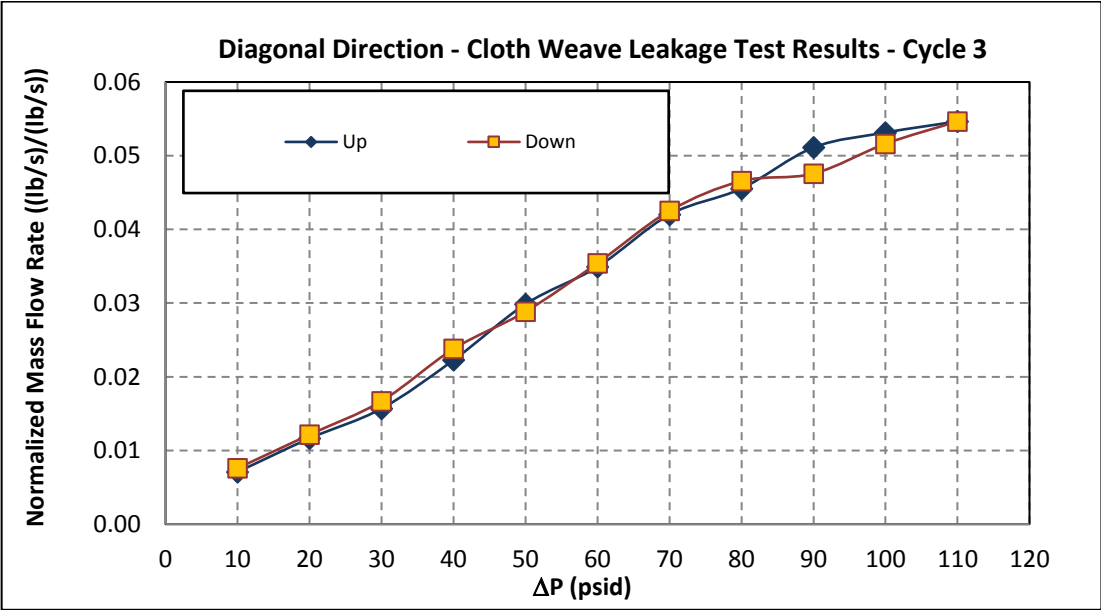


Figure 4.13: Diagonal direction cloth weave leakage test results – Cycle#3

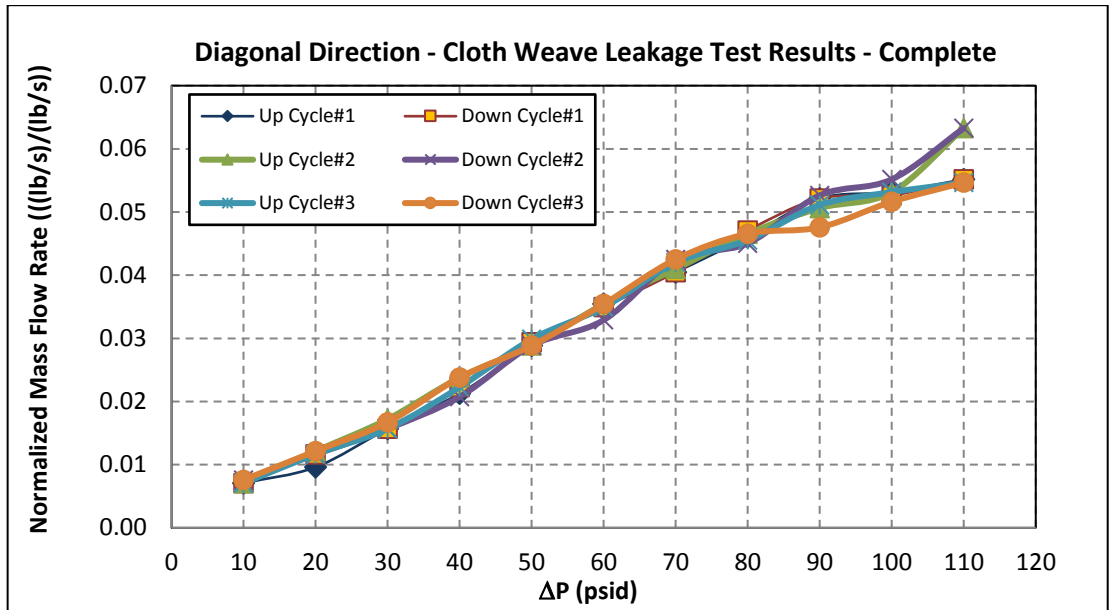


Figure 4.14: Diagonal direction cloth weave leakage test results – All results

#### 4.2.4 Cross Direction

The measured leakage data for three cycles at eleven test points of cross direction are represented from Figure 4.15 to Figure 4.18. Upcycles are symbolized as dark blue rhombus whereas downcycle are represented as yellow squares.

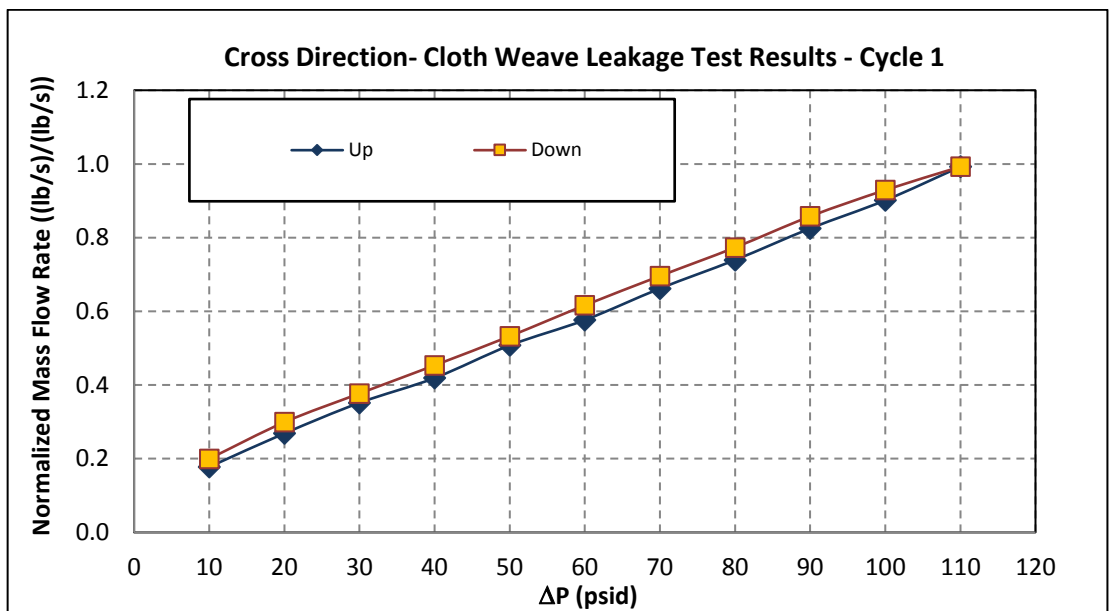


Figure 4.15: Cross direction cloth weave leakage test results – Cycle#1

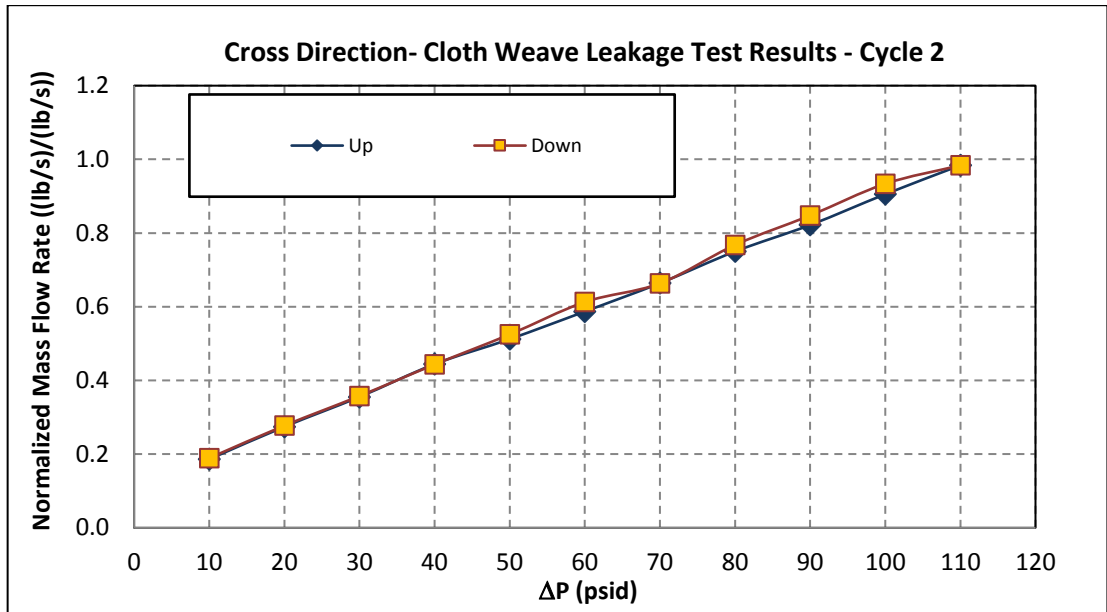


Figure 4.16: Cross direction cloth weave leakage test results – Cycle#2

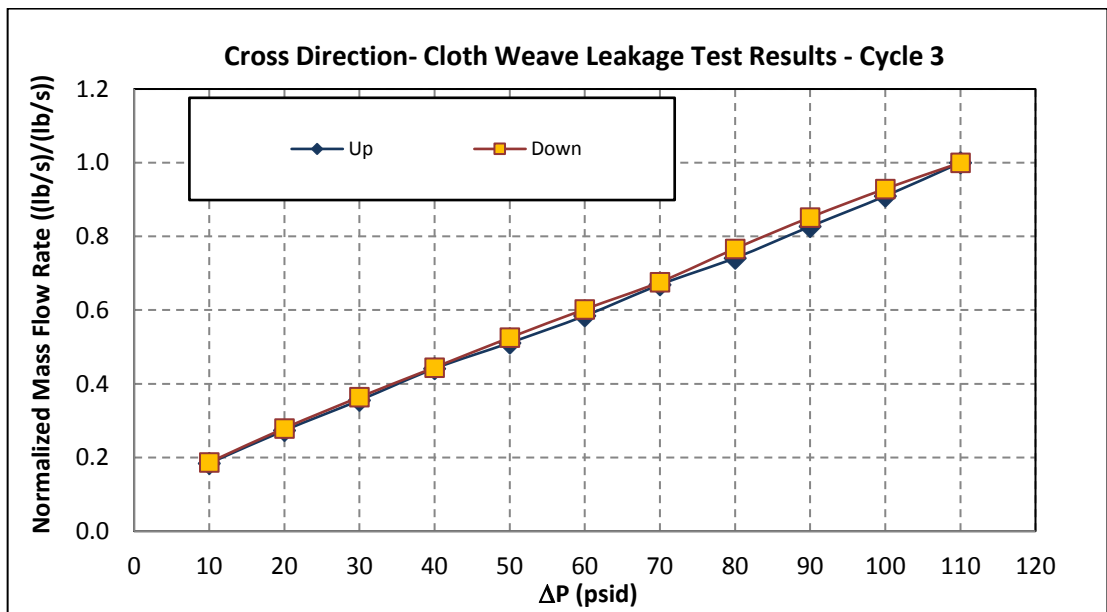


Figure 4.17: Cross direction cloth weave leakage test results – Cycle#3

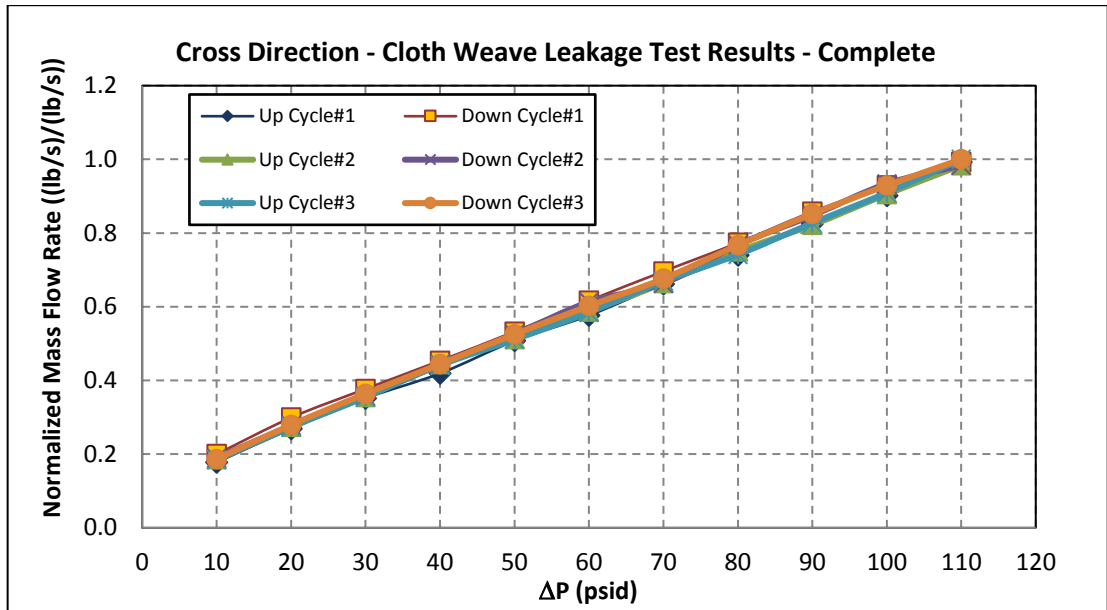


Figure 4.18: Cross direction cloth weave leakage test results – All results

As a result of cloth weave leakage tests, mass flow (leakage) rate is dependent on pressure difference. The results are compared with literature data and used in CFD correlation studies.

#### 4.2.5 Comparison of Cloth Weave Tests with Literature

Leakage test results of cloth weave are compared with the Dinc et.al.'s data [7], In order to compare leakage performance in all cloth weave directions, the parameter of equivalent gap is employed. Since the area exposed to leakage flow are different for each cloth weave direction, equivalent gap values are calculated and normalized with respect to weave thickness for in-plane directions of warp, shute and diagonal. The normalization is done by using flow area for cross direction.

Flow performance of warp, shute, diagonal, and cross directions in terms of the normalized equivalent gap is plotted and compared in Figure 4.19. Present test results are plotted with solid lines while Dinc et.al.'s data [7], which includes several weave densities, are plotted with dashed, dotted, and dot-dashed lines. The present test also includes the cross direction and extends the test data for higher pressure ratios.

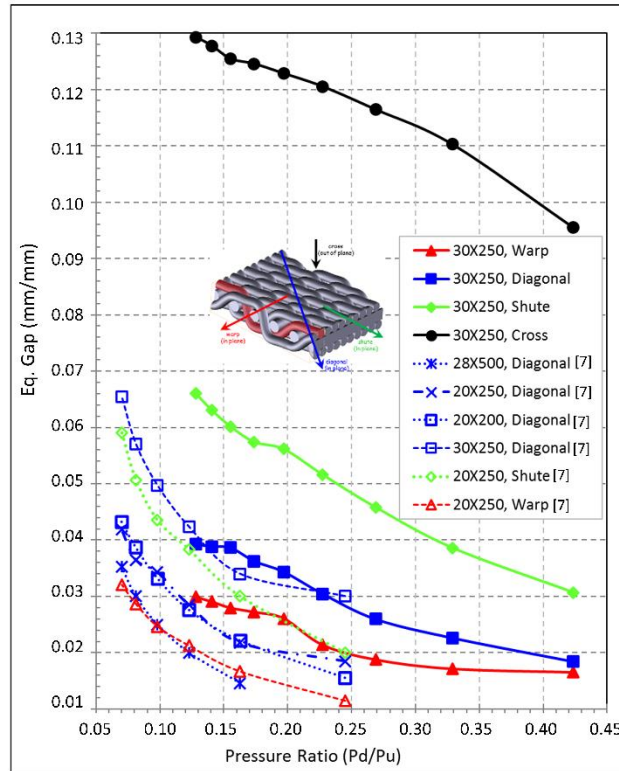


**Figure 4.19: Comparison of cloth weave flow performance for all directions of warp, shute, diagonal and cross.**

Test results in Figure 4.19 indicate that the best leakage performance in terms of the normalized equivalent gap is in the warp direction followed by diagonal, shute and cross directions. These directional best sealing results are compatible with Dinc et.al. study [7]. Similar to leakage results of different cloth weave densities [7], cloth weave leakage is dependent on the pressure load.

While comparing the present test data with Dinc et.al.'s data, it should be noticed that the weave densities are different for warp and shute directions. The difference between present test data and Dinc et.al.'s data are minimal for the same weave density (30x250) at diagonal direction while present tests measure higher leakages for warp and shute directions. This could be attributed to weave density as the main parameter.

Cross direction has the highest normalized equivalent gap; therefore, it is the worst direction in terms of leakage performance. Normalized equivalent gap for cross direction is 2-4 times higher than in-plane directions (warp, shute, diagonal).

As a result, leakage rate is minimum if the flow is in the warp direction. Leakage test results point out that, for the best sealing practices, the cloth weave in cloth seal geometry should be aligned in such a way that flow direction would be in the warp direction. The weave alignment depends on the engine location and working conditions that dictate the flow over the cloth seal.

### 4.3 Cloth Seal Test Rig

Cloth seal test system is established to test several cloth seal designs and allows to change dimensions and angle of the slot. Therefore, it is designed with several components that have alternative dimensions. As illustrated in Figure 4.20, the test system is comprised of a test fixture, a compressor, an air dryer, a flowmeter, pressure sensor, pipes, globe and ball valves. Air is pressurized by the compressor, then passes through the air dryer to dehumidify and filter particles. High-pressure flow reaches the test rig from the upstream side. Flow is forced through the sealing clearance and discharged to the atmosphere. The leakage tests are conducted by varying upstream pressure and keeping the downstream pressure constant.

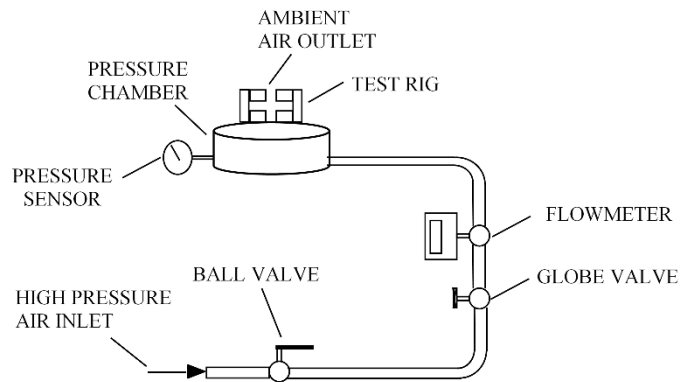


**Figure 4.20: Schematic and connections of the cloth seal test system.**

Upstream pressure is measured from the pressure chamber as shown in Figure 4.20. The pressure sensor has an accuracy  $\pm 0.25\%$  of the full-scale range. It has a range from 0 to 3447 kPa. A mass flow meter is placed after the globe valve. It operates with an accuracy  $\pm 1\%$  of the full-scale range. The mass flow meter has a range from 0 to 330 kg/sec. Globe valve allows adjusting the inlet pressure. Once upstream pressure is stabilized at the required pressure drop value, pressure and leakage data are recorded. A

data acquisition system is conducted to capture pressure and leakage data. Before starting each test, the test rig is pressurized to determine the undesired bias leakage between components. Bias leakage is the undesired flow that leaks between the rig components rather than through the cloth seal. It tends to consistently increase measured leakage rate, therefore, results in a systematic error for leakage rate. A separate set of tests is conducted to calculate bias leakage at each pressure drop. During these tests, actual sealing interfaces are glued, and bias leakage flow is measured under determined test pressure load levels. Actual leakage rates are obtained as the difference between measured flow rate and bias leakage rate.

The leakage test rig is configured to test cloth seal parameters in different operational ranges (Figure 4.21). The test rig consists of left and right slot components, control apparatus; side, top, bottom, front, and rear plates. Front and rear plates are hidden to show other components better. The bottom plate is fixed onto the pressure chamber. A slot in the bottom plate allows fluid flow from the pressure chamber to the upstream side of the cloth seal. The downstream side of the test system is opened to the atmosphere. Two spacers allow to adjust both position and angle relatively between right and left slots. Therefore, mismatch and offset levels can be changed. The cloth seal is placed into the region which is illustrated with the dashed black line rectangle. Some dimensions of the leakage test rig are illustrated in Figure 4.22.

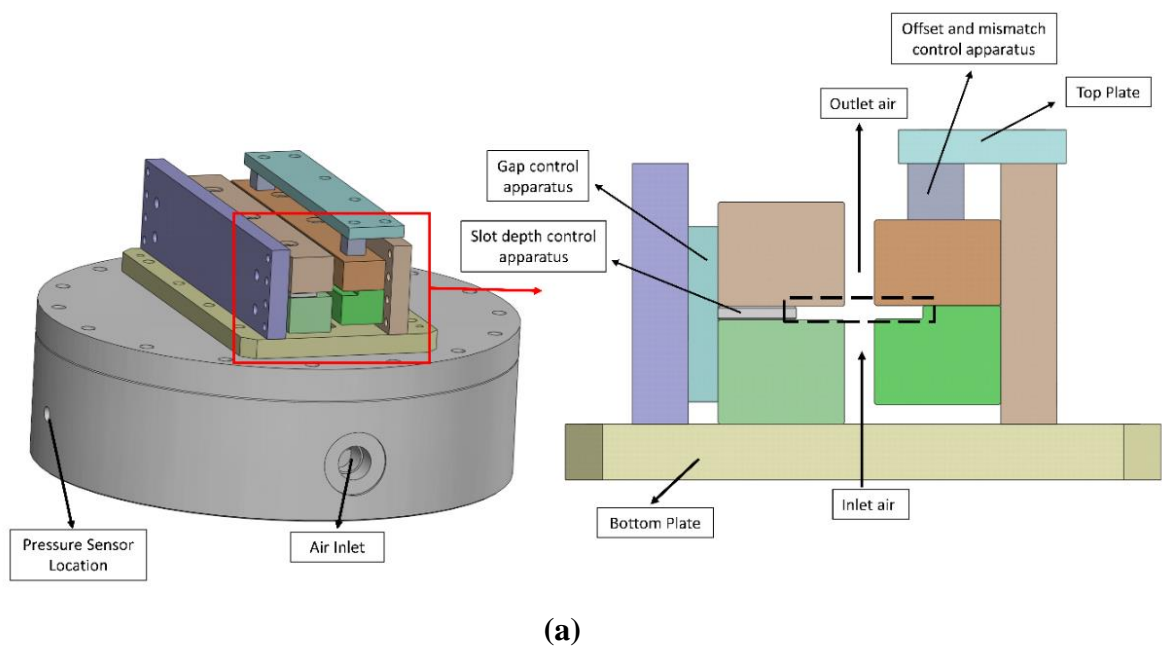


**Figure 4.21: Pressure chamber and leakage test rig design: CAD design of pressure chamber and test rig with control apparatus**

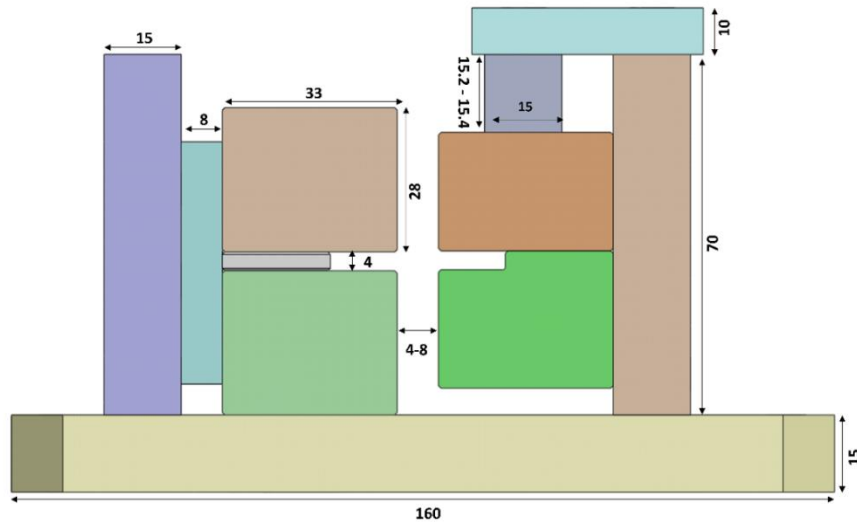


**Figure 4.22: Leakage test rig dimensions (the units are in mm).**

Rig design allows all components to be disassembled between experiments when dimensions of some of the components need to be changed. Some experimental difficulties are encountered during test combinations since glued components must be separated after each test. However, all experiments were completed successfully. The tests are conducted to measure leakage rate at different slot depths, surface roughness, gap, offset, and mismatch levels. Experiments are performed at pressure levels of 30 psid (206.8 kPad), 50 psid (344.7 kPad), and 70 psid (482.6 kPad). The tests are conducted at room temperature, and the test rig is pressurized with dry air. Tests are repeated three times for each data point to capture variations between test cycles. In each test cycle, pressure drop is increased up to the slightly higher than the required pressure drop level as set by the experimental design and then decreased down to atmospheric level. Therefore, six leakage rate data are measured and averaged for an experiment. The leakage rate data and accuracy of the sensor are used for uncertainty analysis.

#### **4.4 Uncertainty Analysis of Leakage Test Results**

##### **4.4.1 Cloth Weave**

The uncertainty levels for the warp, shute, diagonal, and cross direction leakage tests are illustrated in Figure 4.23 for 68.9–758.4 kPad (10–110 psid) pressure differences. The calculated uncertainties are divided by the arithmetic mean of six corresponding

pressure drop leakage results. The Type B/average leakage is dependent on the accuracy of the flowmeter; therefore, it is constant for all cases. The Type A/average leakage varied with respect to the variance between the measurements. The combined and expanded uncertainties followed a similar trend as the Type A uncertainty. The expanded uncertainty/average leakage ( $k = 3$ , for a confidence level of 99.7%) is equal to or less than 10% for all the tested cases. The uncertainty analysis addressed random measurement errors due to the compressor, dryer, test rig, etc. No correlation between the error rate and the pressure drop level is found.

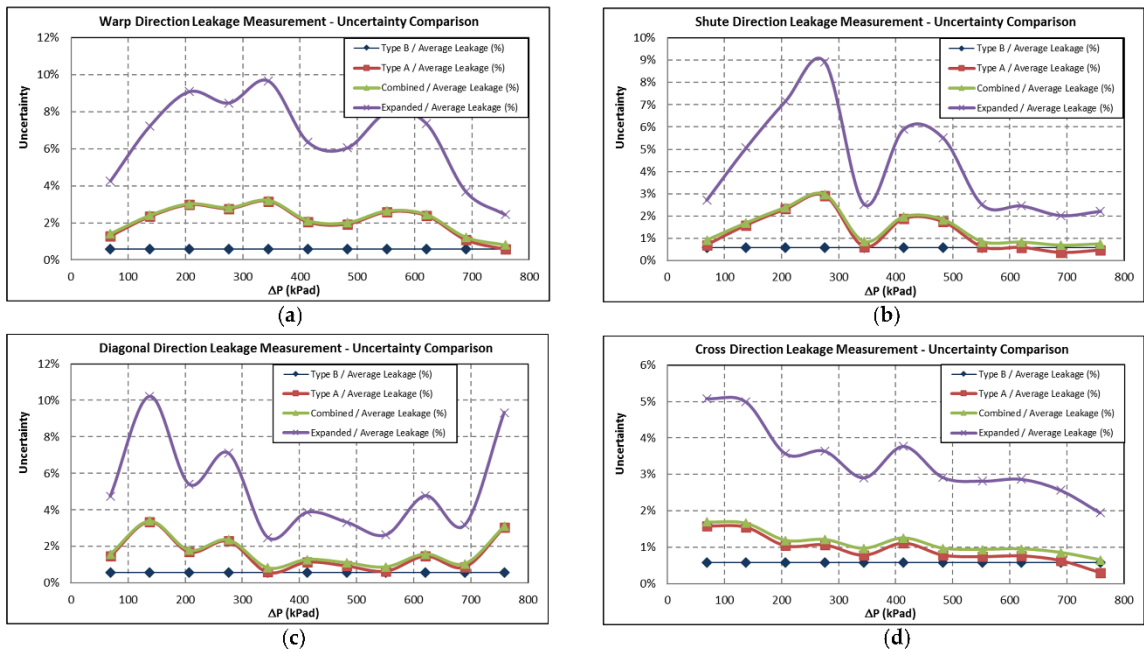


**Figure 4.23: Uncertainty analyses for cloth weave leakage tests: (a) warp direction, (b) shute direction, (c) diagonal direction, and (d) cross direction.**

#### 4.4.2 Cloth Seal

The uncertainty levels of screening and main experiment leakage tests are illustrated in Figure 4.24 and Figure 4.25, respectively. The calculated uncertainties are divided by the arithmetic mean of six corresponding pressure drop leakage results. Type B/Average Leakage is dependent on the accuracy of the flowmeter, therefore, it is constant for all experiments. Type A/Average Leakage is varying with respect to variance between measurements. Combined and Expanded Uncertainties follow a similar trend

with Type A Uncertainty. Expanded Uncertainty/Average Leakage ( $k = 3$ , for a confidence level of %99.7) is calculated less than %10 for all experiments.

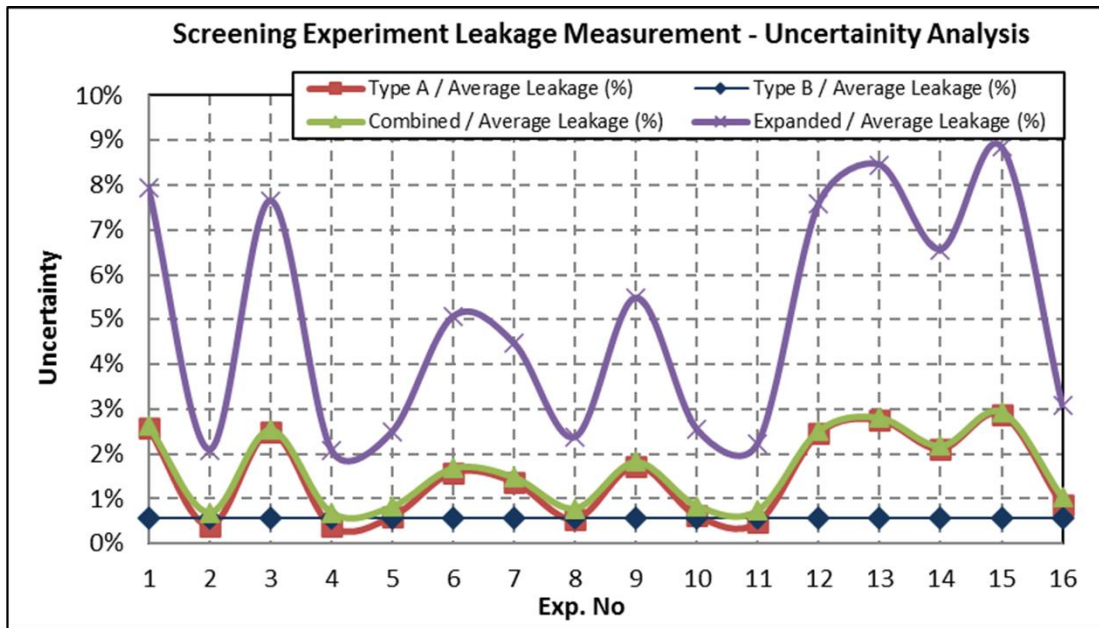


Figure 4.24: Uncertainty analyses for screening experiments.

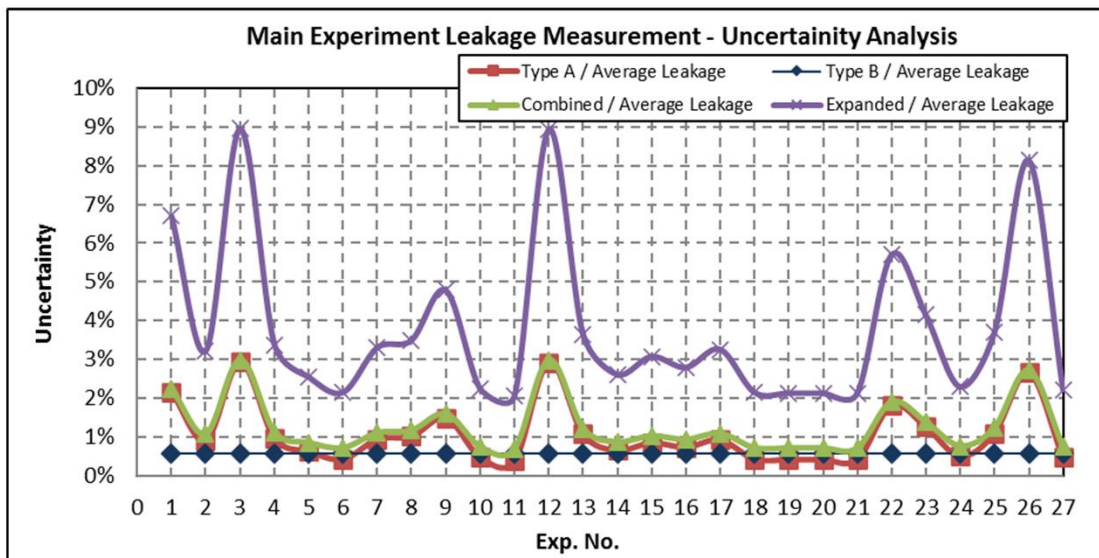


Figure 4.25: Uncertainty analyses for main experiments.

## **5 CLOTH WEAVE AND CLOTH SEAL CFD MODEL ANALYSIS**

In this chapter, computational fluid dynamics (CFD) studies for both cloth weave and cloth seal are presented. Leakage tests are performed for both cloth weave and cloth seal in air environment. The porous medium flow resistance coefficients can be calculated reliably from the solution of three-dimensional Navier-Stokes equations with CFD models and used to calibrate them for the representation of aerodynamic effects in analytical models. Therefore, different approaches are investigated, and Sutherland-ideal gas approach is applied for estimation of flow resistance coefficients. In order to find calibrated resistance coefficients, cloth weave CFD analyses are conducted.

Leakage rates which are obtained in cloth weave experiments, are matched with CFD analyses by calibrating flow resistance coefficients.

ANSYS CFX solver is used in both cloth weave and cloth seal CFD analyses. Geometry is created in ANSYS Workbench which provides automatic mesh and surface updates with respect to change in geometry. The workstation has 8 cores operating at 3.5 GHz with 32 GB RAM. The details of the work and findings are explained in the following sections.

### **5.1 Cloth Weave CFD Analyses and Correlation with Experiments**

In this study, cloth weave is modeled as porous medium with inertial and viscous flow resistance coefficients. Leakage rate is changed with respect to these coefficients. Porous media flow resistance coefficients are changing with respect to geometry, pressure, temperature, etc. For this reason, several methodologies (such as pressure drop – velocity, Sutherland-ideal gas approach, Ergun equation) are examined to estimate flow resistance coefficients (3.2). The present study investigates the accuracy of several methodologies to calibrate porous medium flow resistance coefficients at different pressure loads. CFD analyses of in-plane and out-of-plane directions of cloth weave are correlated with leakage test results. The modeling details are listed below:

1. For in-plane CFD analysis (warp, shute, and diagonal), the CFD model is modeled in a 3-D cartesian coordinate system (Figure 5.1). Three cell thicknesses are considered in the third direction. The symmetry boundary conditions are applied on two surfaces to reduce the computational domain and time.
2. For the out-of-plane direction of cross flow, a section model with  $1^\circ$  in the 3-D cylindrical coordinate system is used since a circular piece of cloth weave is tested in the sample holders (Figure 5.2).
3. Cloth weave is modeled as a porous medium for which flow resistance coefficients are determined by applying approach. The volume porosity of the cloth weave domain is calculated from porosity equation derived in Section 3.3.1. It is validated experimentally by using the weight, density, and volume of the cloth weave sample.
4. The operating fluid is air.
5. Steady-state CFD analyses are performed.
6. The flow is compressible and turbulent.
7. The turbulence flow model is set to k- $\epsilon$  turbulence model with 5% turbulence intensity at inlet and outlet faces of the model domain.
8. Static pressure and temperature values are defined on the inlet boundary. Opening pressure and temperature boundary conditions are applied for outlet boundary.
9. Smooth wall roughness is defined for static walls. For the smooth wall roughness, dimensionless sand-grain roughness is between 0 and 5. Adiabatic and no-slip wall boundary conditions are used for the walls. The maximum  $y^+$  value reached 5.
10. In the porous cloth weave domain, the resistance coefficients are applied for each direction of warp, shute and diagonal.
11. The momentum, mass, and turbulence kinetic energy residuals are set to  $10^{-5}$  for convergence. Most of the converged CFD cases provided residuals less than  $10^{-8}$ . In some high pressure-ratio CFD cases ( $P_d/P_u < 0.1$ ), the residuals are between  $10^{-5}$  and  $10^{-6}$ . For all the CFD cases, several convergence criteria for the velocity,

temperature, pressure, turbulence quantities, and inlet and outlet mass flow rates are met.

The boundary conditions are tabulated in Table 5.1.

Direction	Analyze Details	Turbulence Model	Fluid	Fluid Temperature	Pressure Difference	Outlet Pressure
Shute	Steady State, 3-D	k- $\epsilon$	Air	25°C	68.9-758.4 kPad (10-110 psid)	101.4 kPa
Warp						
Diagonal						
Cross						

**Table 5.1: Boundary conditions and model details for In-Plane and Out-of-Plane CFD analyses**

CFD model domain and boundary conditions for in-plane directions of warp, shute, and diagonal are illustrated in Figure 5.1. The out-of-plane CFD model domain and boundary conditions for cross flow direction is shown in Figure 5.2.

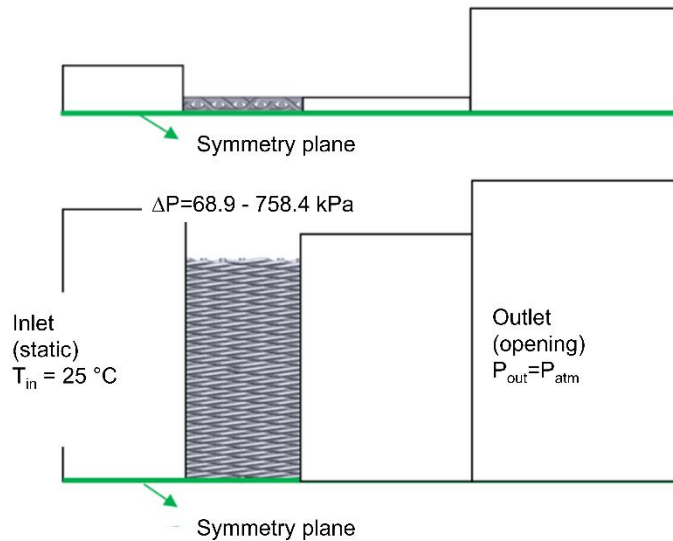


**Figure 5.1: CFD model domain and boundary conditions for in-plane directions of warp, shute, and diagonal.**

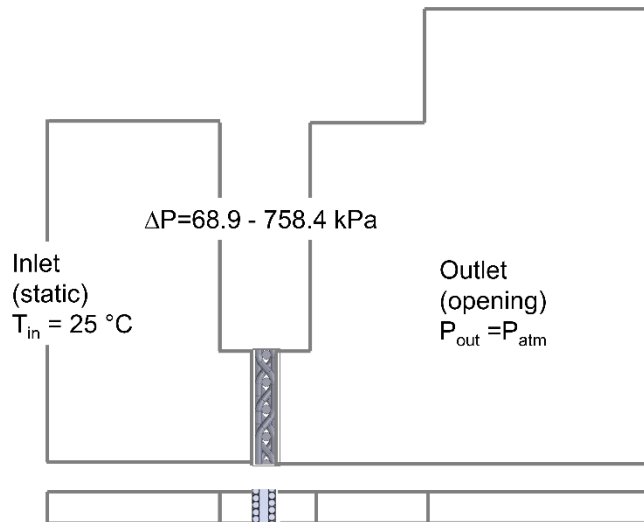


**Figure 5.2: CFD model domain and boundary conditions for out-of-plane direction of cross.**

The CFD model for cross direction includes 60,000 hexahedron meshes. Meshes are refined around the cloth weave region where pressure gradients and velocities are high. Since pressure drops in cloth weave thickness, this thickness had at least 30 meshes in the cross direction. A mesh view is shown in Figure 5.3 and Figure 5.4 for in-plane and out-of-plane directions, respectively. A similar size of meshes is used in all CFD analyses. Each simulation needs 4 to 6 hours for convergence.

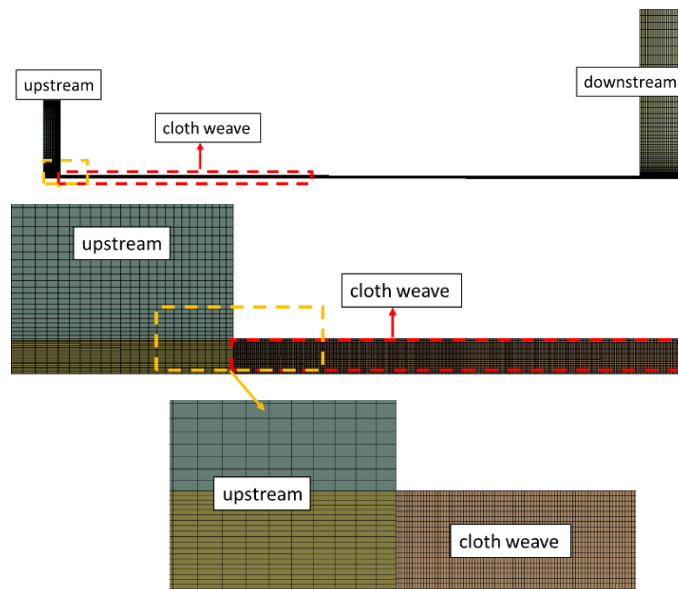


**Figure 5.3: Mesh views for in-plane directions of warp, shute, and diagonal.**

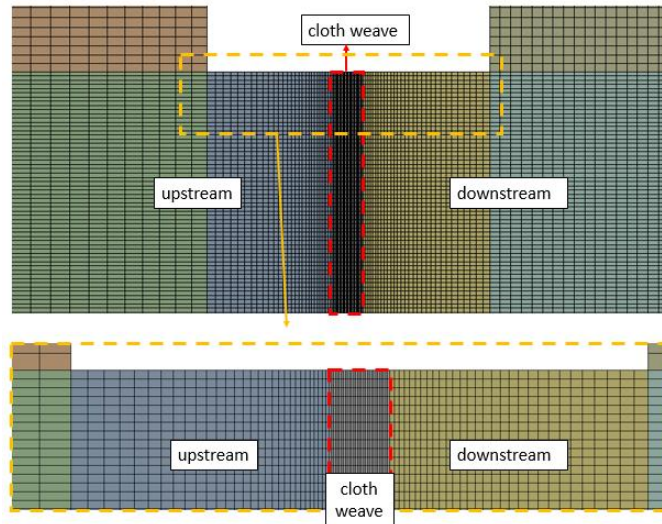


**Figure 5.4: Mesh views for cross direction.**

### **5.1.1 Comparison of Pressure Drop-Velocity & Sutherland-Ideal Gas Approach**

Flow in porous medium is subject to additional flow resistances compared to absence of porous medium. For this reason, a cloth weave CFD model with porous medium approach requires inertial and viscous resistance coefficients, therefore, those coefficients need to be determined. Due to limitations of Bernouilli and Ergun’s equation as discussed in Section 3.2, they are not included in comparison study. In order to compare Pressure drop-velocity and Sutherland-ideal gas approaches, porous media resistance coefficients of cloth weave are correlated for warp direction. The results of experiments and CFD analysis with different resistance coefficient calculation methods are illustrated in Table 5.2 and Table 5.3. The errors show the mass flow rate differences between test and CFD results. In Pressure drop-velocity method, cloth weave pressure drop is clarified as a function of superficial velocity. Viscous (linear) and inertial (quadratic) resistance coefficients are determined for both “Density of average conditions” and “Inlet&outlet density” methods. One method is named “inlet&outlet density” to obtain flow density which is average of inlet and outlet density. Another method to obtain density is “density of average conditions” method which uses average value of inlet and outlet pressure and temperature in porous region.

The velocity is calculated by using mass flow rate, flow area and density which is found with two different methods. Second-order curves are fitted with two different methods. The calibrated flow resistance coefficients for Pressure drop-velocity

(Inlet&outlet density) are; inertial flow resistance:  $\alpha=3.477 \times 10^3 \text{ kg/m}^4$  and viscous flow resistance:  $\beta=1.092 \times 10^6 \text{ kg/m}^3\text{-s}$ . For Pressure drop-velocity (Density of average conditions) approach, inertial flow resistance is found as  $\alpha=2.150 \times 10^5 \text{ kg/m}^4$  and viscous flow resistance is  $\beta=1.375 \times 10^4 \text{ kg/m}^3\text{-s}$ . These flow resistance coefficients are kept constant for different pressure drop cases. The errors between experiments and CFD analysis with inlet& outlet density method are high (error 18-50%). For density of average conditions method, the errors between experiments and CFD are less than 10% for  $\Delta P > 413.7 \text{ kPa}$  (60 psi), however, the difference reaches up to 25% at  $\Delta P = 137.9 \text{ kPa}$  (20 psi).

<b>Error (%) between experimental and CFD leakage rate results (Pressure Drop – Velocity approach)</b>			
<b><math>\Delta P</math> (kPa)</b>	<b><math>\Delta P</math> (psi)</b>	<b>Pressure Drop – Velocity (Inlet&amp;outlet density)</b>	<b>Pressure Drop – Velocity (Density of average conditions)</b>
137.9	20	18.0	25.1
206.8	30	12.7	11.5
275.8	40	22.5	10.6
344.7	50	30.1	20.6
413.7	60	31.4	15.1
482.6	70	38.1	9.0
551.6	80	42.5	5.8
620.5	90	46.5	2.1
689.5	100	48.7	1.1

**Table 5.2: Error between experimental and CFD leakage rate results (Pressure Drop – Velocity approach)**

The leakage rate errors between CFD analyses and experiments of the Sutherland-ideal gas approach are shown in Table 5.3. Inertial flow resistance coefficients are changing with respect to pressure ratio whereas viscous flow resistance coefficients are constant for all cases since temperature is constant in experiments. At first, to obtain a base point in calibration, inertial and viscous resistance coefficients for  $\Delta P = 689.5 \text{ kPa}$  (100 psid) are calibrated by matching test and CFD leakages. Inertial flow resistance coefficient is decreased in lower pressure drop cases. For lower  $\Delta P$  cases, the difference between experiments and CFD is higher than 10% except  $C_{\text{down}} = 0.9$ . Variation between

experiments and CFD cases ( $C_{\text{down}} = 0.9$ ) are less 10% for  $\Delta P = 137.9 \text{ kPa} - 689.5 \text{ kPa}$  (20-100 psi). Results show that Sutherland-ideal gas approach with  $C_{\text{down}} = 0.9$  provides a good leakage agreement with the experiments in warp direction.

This study shows that the use of a different set of porous flow resistance coefficients for different pressure drop cases provides better leakage agreement. The result is compatible with the study of Chen et.al [65]. They emphasized that resistance coefficients are related to pressure load.

$\Delta P$ (psi)	<b>Error (%) between test and CFD results (Sutherland-ideal gas approach)</b>				
	$C_{\text{down}} = 0.5$	$C_{\text{down}} = 0.6$	$C_{\text{down}} = 0.7$	$C_{\text{down}} = 0.8$	$C_{\text{down}} = 0.9$
20	22.2	18.9	14.4	8.0	2.8
30	23.5	21.2	18.1	13.2	5.1
40	18.7	16.9	14.3	10.4	3.7
50	4.7	3.1	0.9	2.5	8.3
60	4.2	3.1	1.5	0.9	5.2
70	4.0	3.2	2.2	0.4	2.6
80	2.6	2.1	1.5	0.4	1.4
90	1.5	1.1	0.8	0.2	0.6
100	1.1	1.1	1.1	1.1	1.1

**Table 5.3: the leakage difference between the test and CFD in warp direction (Sutherland-ideal gas approach for resistance coefficients)**

In summary, leakage rate of cloth weave is investigated with both Pressure drop-velocity and Sutherland-ideal gas approaches for warp direction. For Pressure drop-velocity approach, second-order polynomial is fit to obtain inertial and viscous flow resistance coefficients that lead to high leakage rate error between experiments and CFD results. The errors between experiments and CFD of Pressure drop-velocity (Inlet& outlet density) approach analyses are 18-50%. For Density of average conditions approach, the errors between experiments and CFD decrease less than 10% for higher pressure, on the other hand, the errors reach up to 25% in low pressure drop cases.

In addition to the study that details are explained in this section, both Pressure drop-velocity and Sutherland-ideal gas approaches are also applied in different directions and

several conditions. A comprehensive calibration study shows that the inertial or viscous resistance coefficient is calculated as a negative value in some cases of Pressure drop-velocity approach. Negative flow resistance coefficient values are not compatible with the physics behind.

The results show that Sutherland-ideal gas approach provides a good match with leakage test results by calibrating  $C_{\text{down}}$  value. Therefore, CFD analyses are performed and compared for all directions by calibrating flow resistance coefficients with Sutherland-ideal gas approach in the following section.

### **5.1.2 Sutherland-Ideal Gas Approach CFD Analysis of Cloth Weave**

In order to determine the metallic-cloth fiber flow resistance coefficients that matched with the test leakage, metallic-cloth fiber CFD models are built for each direction of warp, shute, diagonal, and cross. For each direction, CFD analyses are performed with weave flow resistance coefficients calculated by using the Sutherland-ideal gas approach and test data. Then, the CFD leakages are compared with the test leakages.

CFD analyses are run under test conditions by using the Sutherland-ideal gas approach. In the calibration of the metallic-cloth fiber flow resistance coefficients, test data at the minimum and maximum pressure loads are excluded, to stay in the minimal test noise range. Thus, the CFD analyses are performed at nine points between  $\Delta P = P_u - P_d = 137.9$  and  $689.5$  kPad (20–100 psid) with  $68.9$  kPad (10 psid) increments. The ambient temperature is defined on the upstream side, which is measured during the tests.

At first, to obtain a base point in the calibration, the inertial and viscous resistance coefficients for  $\Delta P = 689.5$  kPad (100 psid) are calibrated by matching the test and CFD leakages (Figure 5.5a).

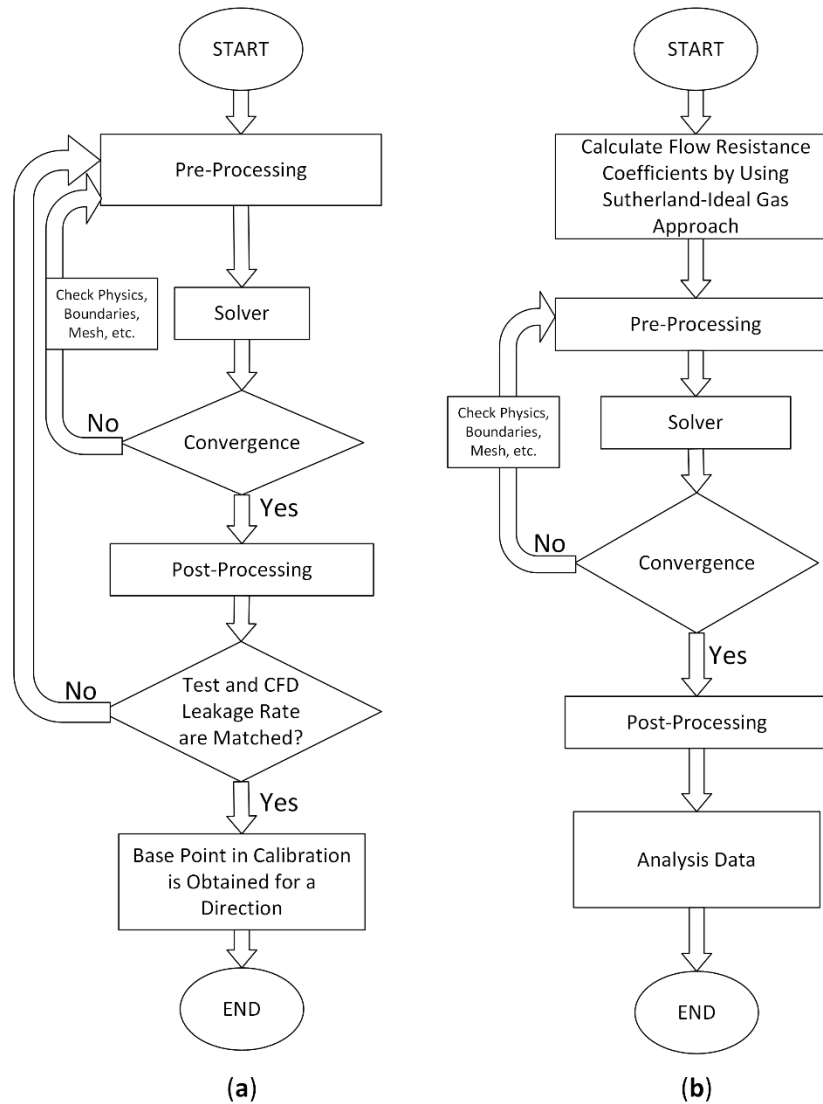


**Figure 5.5: Flowchart describes the steps for CFD analyses of Sutherland-ideal gas approach (a) base point and (b) calibration process for different pressure loads.**

In the calibration process (Figure 5.5b), the CFD analyses utilized the Sutherland-ideal gas approach as stated in Equations 3.25–3.28. It should be kept in mind that the inertial resistance coefficient varies with pressure and temperature (Equation 3.25), whereas the viscous resistance coefficient is only a function of temperature (Equation 3.26). In the tests and CFD analyses, the temperature is observed to be nearly constant. That is, the resistance coefficients changed depending on the evaluation of the pressure level, which varied over the weave flow thickness. This is represented with the pressure constant ( $C_{\text{down}}$ ) as stated in Equations 3.27–3.28. Therefore, the CFD analyses are repeated for a range of pressure constants  $C_{\text{down}} = 0.5\text{--}1.0$  for in-plane directions and

$C_{down} = 0.0-1.0$  for the cross direction, with 0.1 increments, to determine the best leakage match with the test data.

In comparing the test and CFD leakages, the leakages are normalized by dividing the leakage of the cross direction at the maximum pressure load of 758.4 kPad (110 psid).

All the tests and CFD leakages are compared in Figure 5.6 for all four directions of warp, shute, diagonal, and cross. Figure 5.6 includes the whole range of pressure constant values for all weave directions.

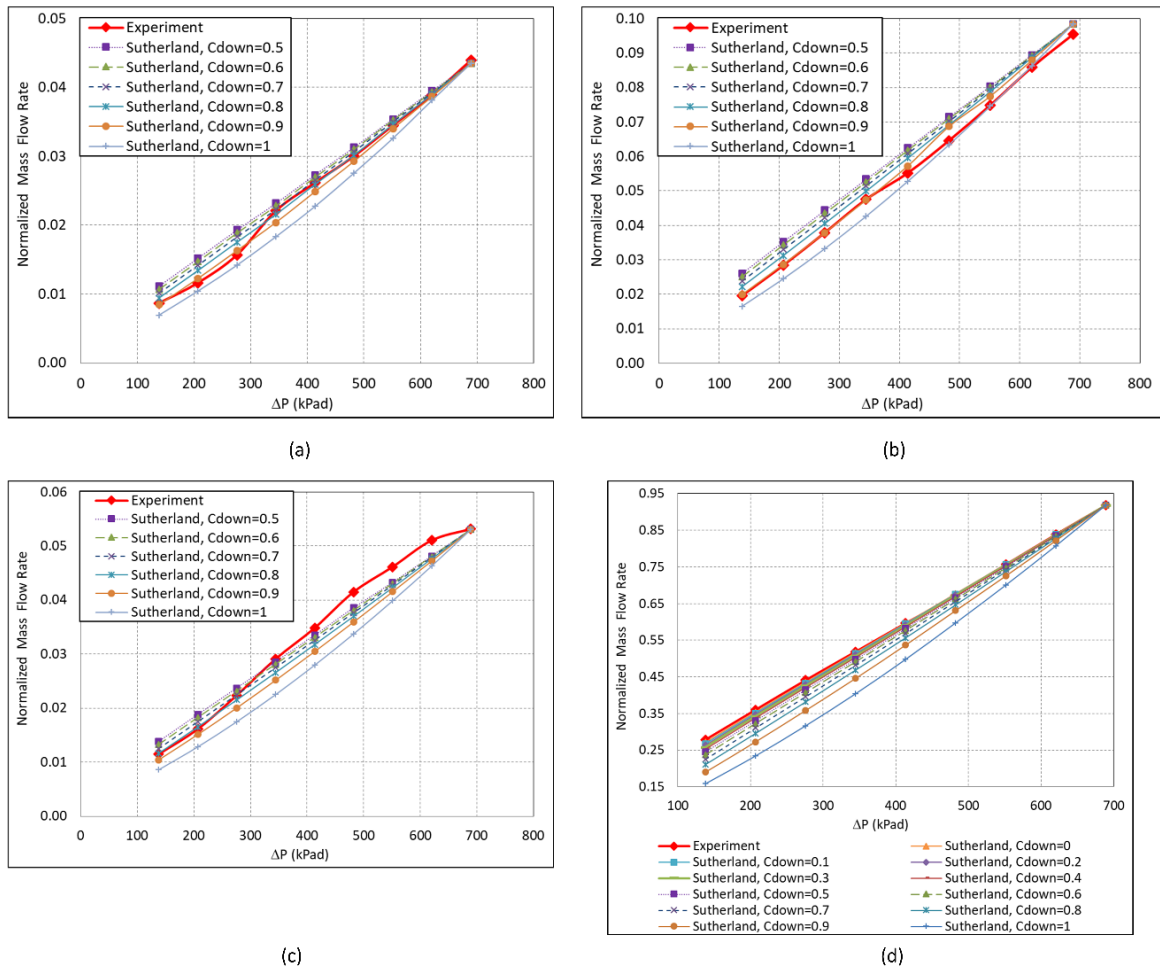


**Figure 5.6: Comparison of CFD and test results for various pressure constant ( $C_{down}$ ) values: (a) warp direction, (b) shute direction, (c) diagonal direction, and (d) cross direction**

For warp and shute directions, the best match between test and CFD leakages is obtained for  $C_{down}=0.9$  at which leakage difference between test and CFD is less than 10% for all pressure loads of  $\Delta P=137.9-689.5$  kPad (20-100 psid).

For diagonal direction,  $C_{down}=0.7$  gives the minimum leakage difference of 10%.

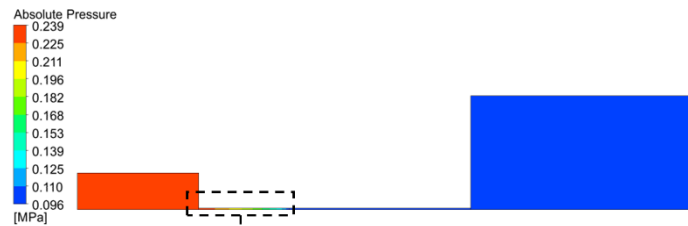
For cross direction,  $C_{\text{down}}=0.0$  provides the best leakage agreement with tests yielding 0.03% difference.

Thus, the best  $C_{\text{down}}$  values are listed below:

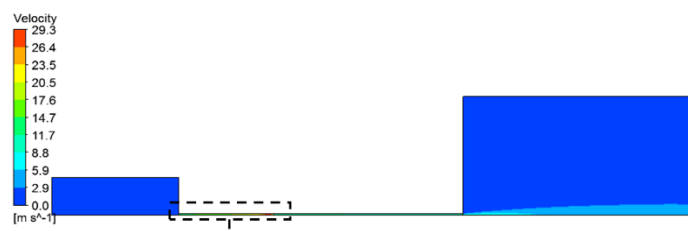
- warp 0.9
- shute 0.9
- diagonal 0.7
- cross 0.0

All these tests and CFD works show that the use of a different set of porous resistance coefficients for different pressure load cases provides better leakage agreement.

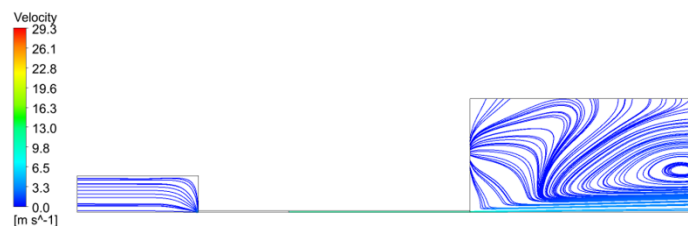
Flow formation within the weave are visualized by plotting pressure contours, velocity magnitude, streamlines, and vectors in Figure 5.7, Figure 5.8, Figure 5.9, and Figure 5.10 for warp, shute, diagonal, and cross directions, respectively.



a) pressure contours



b) velocity magnitude contours



c) velocity streamlines

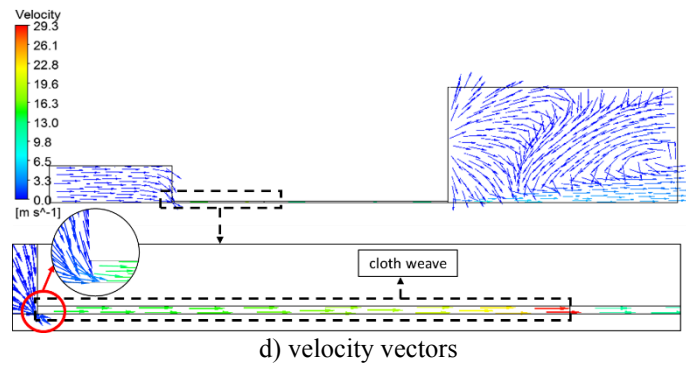
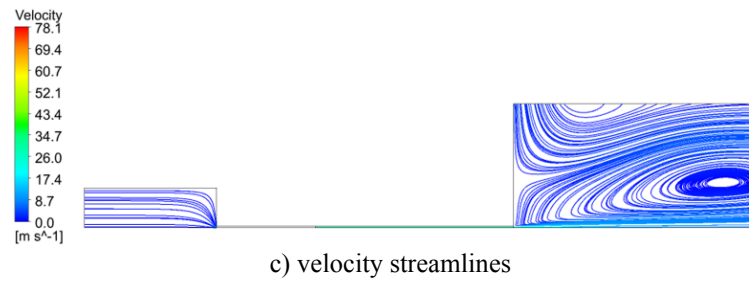
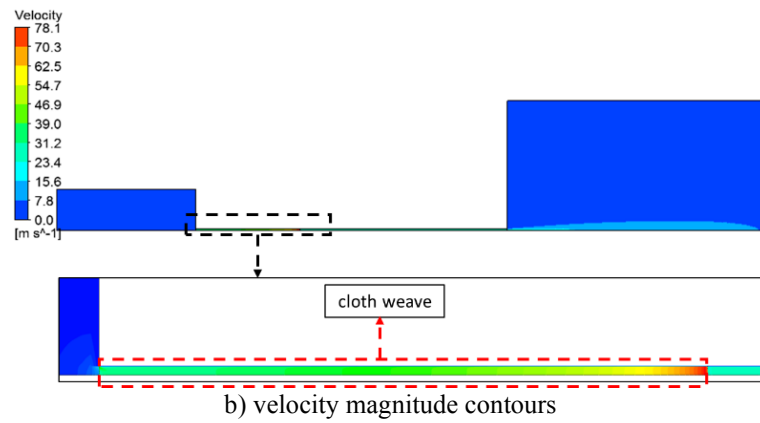
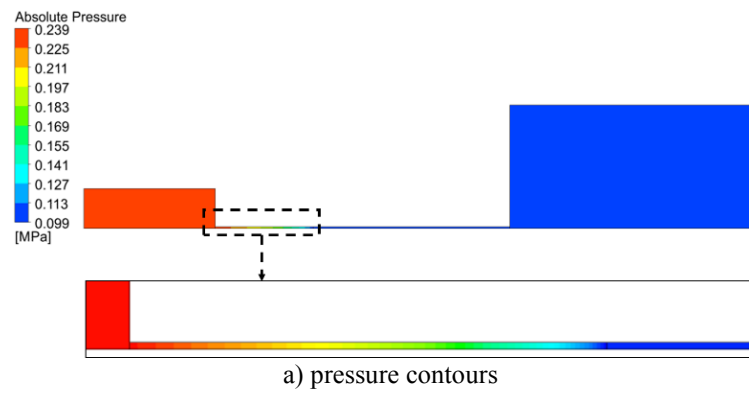


Figure 5.7: CFD results for warp direction ( $C_{down}=0.9$ ,  $\Delta P=137.9$  kPa)



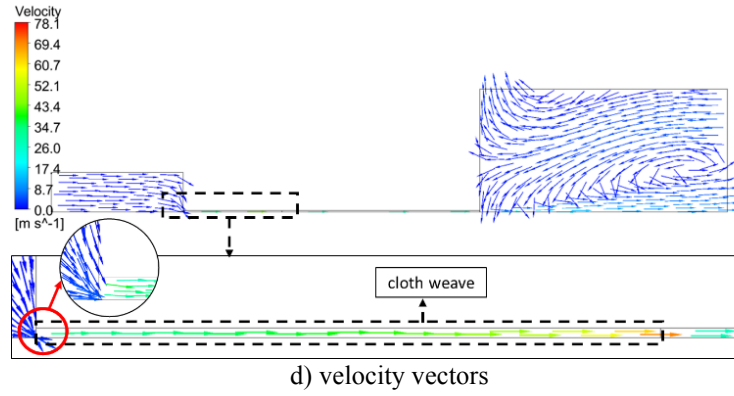
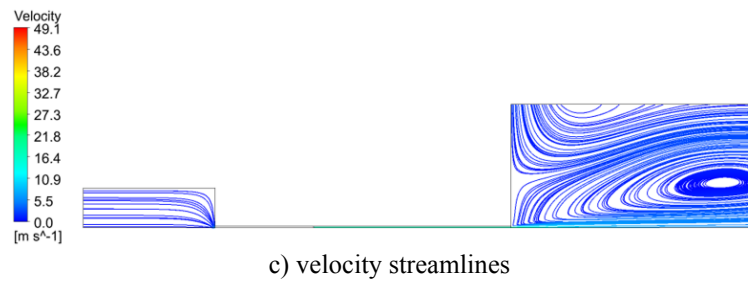
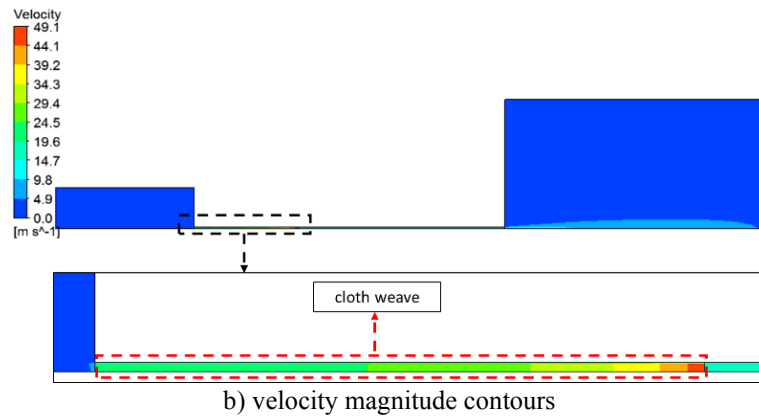
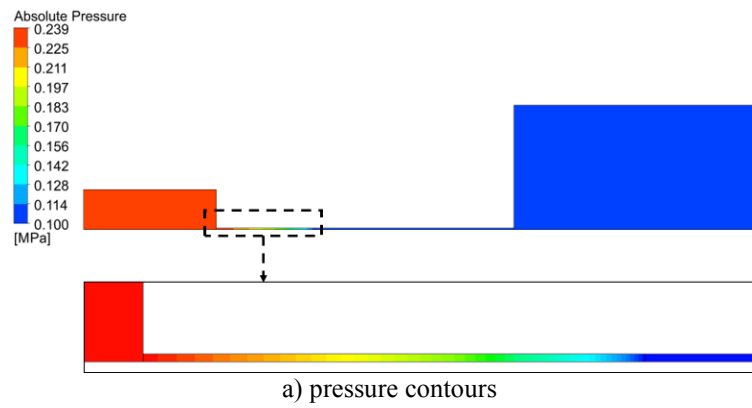


Figure 5.8: CFD results for shute direction ( $C_{down}=0.9$ ,  $\Delta P=137.9$  kPa)



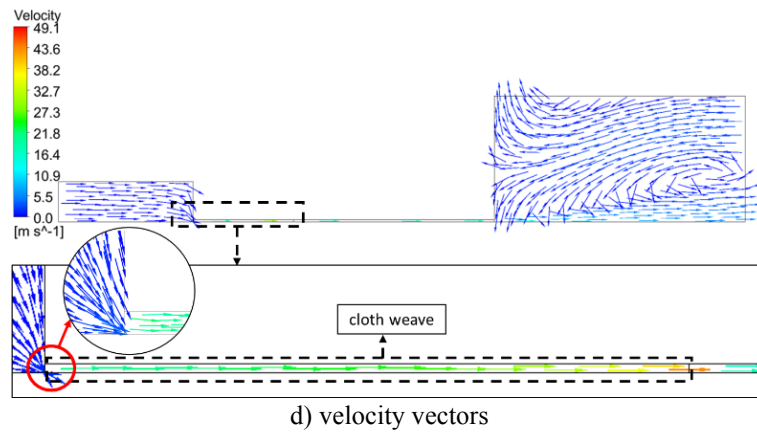
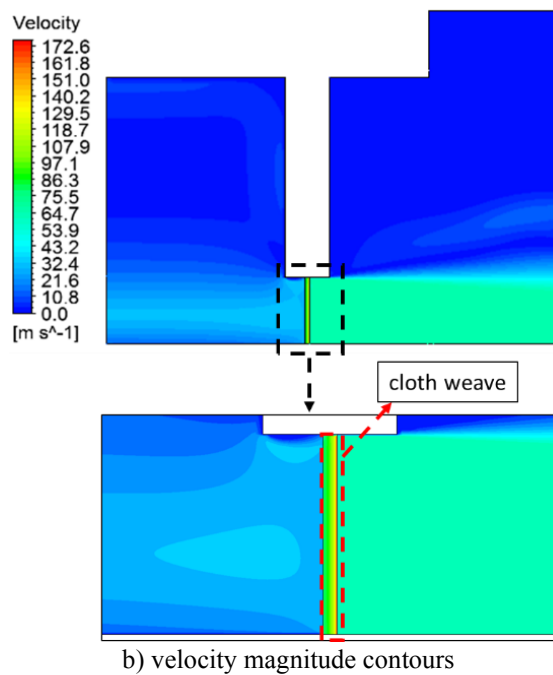
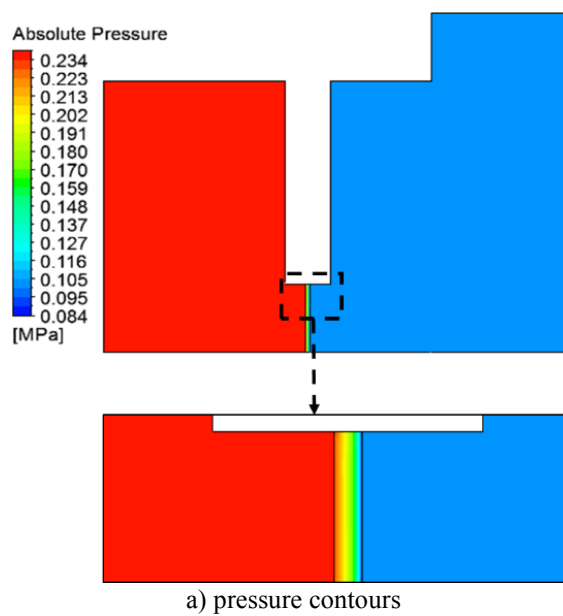
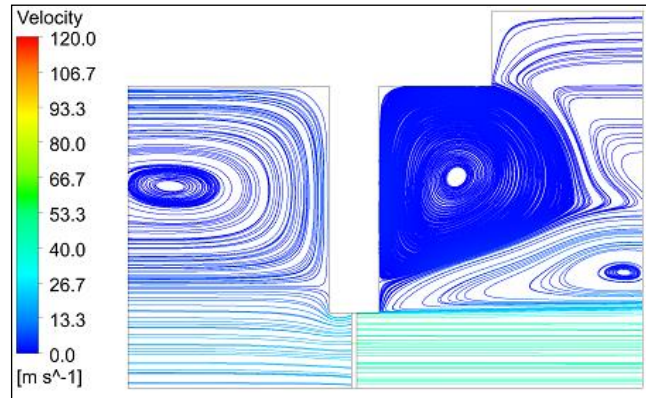
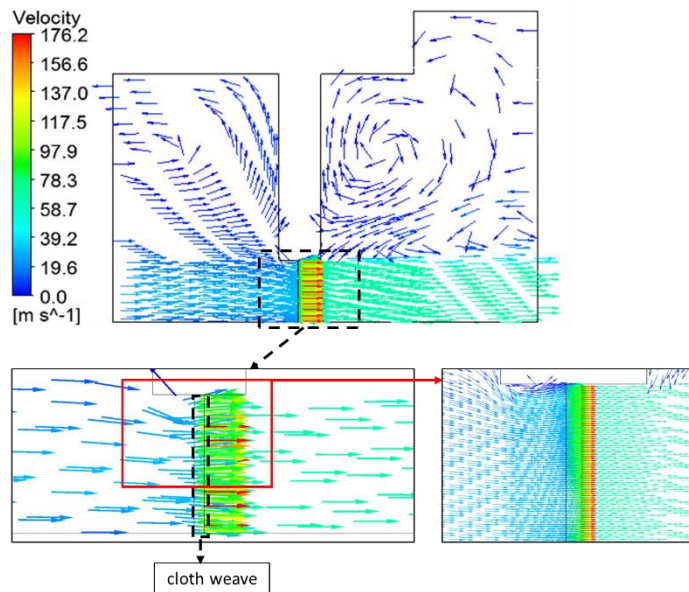


Figure 5.9: CFD results for diagonal direction ( $C_{down}=0.7$ ,  $\Delta P=137.9$  kPa)





c) velocity streamlines



d) velocity vectors

**Figure 5.10: CFD results of cross direction ( $C_{down}=0.0$ ,  $\Delta P=137.9$  kPad)**

In Figure 5.7, Figure 5.8, Figure 5.9, and Figure 5.10, pressure gradually drops through cloth weave. Flow smoothly directs through the cloth weave region from the upstream. These streamlines extending in downstream region due to flow expansion. Flow velocity increases in the porous cloth weave domain since solid regions in porous domain restrict the flow area and accelerates fluid.

Flow formation within the weave is visualized by plotting pressure contours, velocity magnitudes, streamlines, and vectors in Figure 5.7, Figure 5.8, Figure 5.9, and Figure 5.10 for the warp, shute, diagonal, and cross directions, respectively. The pressure is almost constant, except for metallic-cloth fibers, as shown in Figure 5.7a, Figure 5.8a, Figure 5.9a, and Figure 5.10a. The change in color shows that a pressure drop occurs in

the region of the metallic-cloth fibers. The pressure gradually reduced through the cloth weave from the upstream side to the downstream side. In the cloth weave region, the pressure is constant in the radial directions. This supports the assumption that pressure gradients are zero in radial directions, and the values of resistance coefficients in radial directions are not important.

The flow property plots show that the flow is smoothly directed through the region of metallic-cloth fibers from the upstream side for both the in-plane and cross directions, in Figure 5.7b-d, Figure 5.8b-d, Figure 5.9b-d, and Figure 5.10b-d. The figures are mostly plotted with 10 intervals. The diffusing flow into the metallic-cloth fibers accelerated through the cloth weave in the axial direction. The velocity vectors show that the flow strongly moved in the axial direction, and the radial velocity is almost zero in the porous region. Then, the flow extended to the downstream region. The flow velocity reached its maximum value at the downstream side due to expansion. Some recirculation zones formed in the up/downstream regions. The flow velocity distributions are similar in the in-plane directions of warp, shute, and diagonal.

In addition, Figure 5.11 illustrates the normalized pressure within the porous metallic-cloth fibers in the flow direction. The pressure is normalized with respect to the up/downstream pressures as in  $p^* = (P - P_d) / (P_u - P_d)$ , while the flow direction is normalized with the weave thickness as in  $z^* = z/t$ . It should be noted that the weave thickness in the flow direction was  $t = 20$  mm for the in-plane directions, while it is  $t = 0.7$  mm for the cross direction.

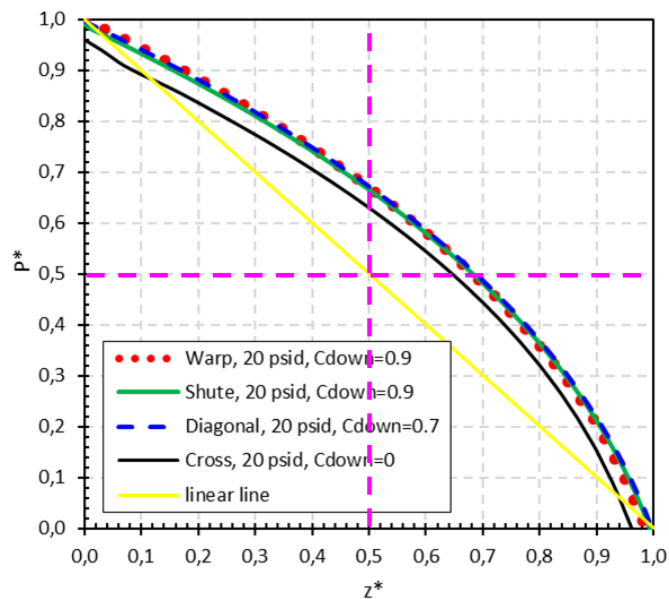


**Figure 5.11: Normalized pressure within the porous metallic-cloth fibers in the flow direction (normalized weave thickness ( $z^*$ ) vs normalized pressure ( $p^*$ )).**

Figure 5.11 shows that the pressure gradually drops over the weave thickness. The pressure variation with the weave thickness is well represented with a polynomial function at least in the second order. Most of the pressure drop occurs at the downstream side. The 50% of the pressure load drops in the first 70% of the weave thickness. Thus, the last 30% of weave thickness is subject to the 50% pressure drop.

In summary, flow properties plots show that the flow smoothly directs through the cloth weave region from the upstream for in-plane directions. Pressure drop occurs over the weave thickness. Then, the flow extends to the downstream region. Flow velocity reaches its maximum value at the downstream side due to expansion. Some recirculation zones form in the up/downstream regions. With selected  $C_{down}$  values, Sutherland-ideal gas approach provides a very good leakage agreement with the experiments. Variations between experiments and CFD results are less than 10% in each direction. The results of this study show that Sutherland-ideal gas approach is a good candidate to estimate flow resistance coefficients and leakage performance of cloth weave in turbine operating conditions. Pressure and velocity fields are visualized to find out cloth weave flow behavior. Porous medium approach represents correlation between cloth weave and fluid very well.

## **5.2 Cloth Seal Benchmark CFD Study with Conjugate Heat Transfer Model**

In order to make sure the models used in cloth seal CFD analysis; previous studies are investigated. A numerical analysis of flow and temperature distribution over cloth seal geometry is studied by a collaboration of Rensselaer Polytechnic Institute and General Electric USA [1]. In order to validate CFD model, a CFD analysis is generated based on geometry and boundary conditions that are used in the previous study [1]. The analysis is run with similar specified geometrical configuration and boundary conditions as shown in the paper. However, geometry and boundary conditions may not be the same as the paper, since some of the properties are not defined clearly. CHT (Conjugate Heat Transfer) models are also included to observe temperature distribution of solid shim and turbine slots. Model is generated in ANSYS Workbench, and analyses are completed in

CFX commercial tool. The model is built in 2-D planar-symmetric coordinate system. The symmetry boundary condition is also defined to turbine slot side. The working fluid is air while simulating the benchmark CFD analysis. The flow in the entire cavity is modeled as compressible and turbulent. The standard k-epsilon approach is used for turbulent flow. The total number of cells is about 134,000 for CFD model. Metal shim and stator casing are modeled with solid materials. Since cloth weave is modeled as a solid domain with a half reduction in its thermal properties in the previous study [1], same methodology is followed in benchmark CFD analysis while modeling cloth weave region. The inlet is defined as inlet boundary condition with static pressure and temperature while the outlet of the model is defined as opening boundary with static pressure upon specified values at upstream and downstream regions. Since cloth seal applied in static sealing regions, surface speed of walls are defined as zero in the model. Benchmark study CFD model geometry and the boundary conditions are illustrated in Figure 5.12. Right half of the overall geometry is modeled, and symmetry boundary condition is applied in the middle plane of cloth seal. Therefore, number of cells is reduced by 50% without any loss of accuracy. The clearance is selected as 0.0427 mm (1.68 mil) which is calculated with respect to the table given in Appendix A.

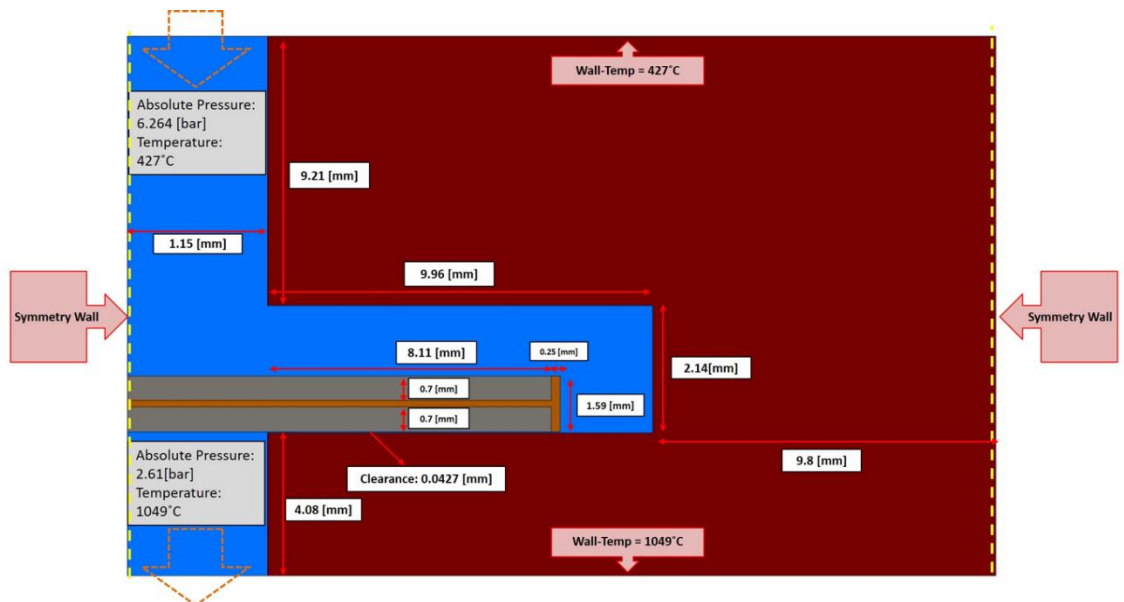


**Figure 5.12: CFD analysis geometry and boundary conditions for the benchmark study**

The boundary conditions and leakage result are tabulated in Table 5.4. Since cloth seal is applied to reduce cooling air contribution to hot gas, upstream temperature is the temperature of coolant flow coming from compressor. Downstream temperature is the hot

gas temperature; therefore, it is considerably higher than upstream temperature. Leakage rate is expressed for 2.54  $\mu\text{m}$  (0.1 mil) third direction thickness.

Case	Ambient	Clearance [ $\mu\text{m}$ ]	Tup [C]	Tdown [C]	Pup [kPa]	Pdown [kPa]	$\Delta\text{P}$ [kPa]	Leakage Rate [kg/s]
CFD Benchmark Study	Air	42.7	427	1049	626.4	261	365.4	$3.82 \times 10^{-8}$ (for 2.54 $\mu\text{m}$ thickness)

**Table 5.4: CFD analysis boundary conditions and leakage result for the benchmark study**

Region	Material	Density [ $\text{kg}/\text{m}^3$ ]	Specific Heat Capacity [J/kg.K]	Thermal Conductivity [W/m.K]
Cloth Seal	Haynes 230 (with half thermal properties)	4485	287	11.2
Fluid	Air	Calculated by ANSYS CFX		
Shim	Inconel 939	7932	664	20.6
Stator Casing				

**Table 5.5: Properties of material used in the CFD model**

The velocity vectors are shown in Figure 5.13 for both AIAA paper [1] (white-black pictures on the left side) and studied benchmark CFD analysis (colored pictures on the right side). High-velocity regions are observed around entrance and exit of clearance region. The flow smoothly approaches the clearance from the upstream side and it accelerates drastically in the clearance region.

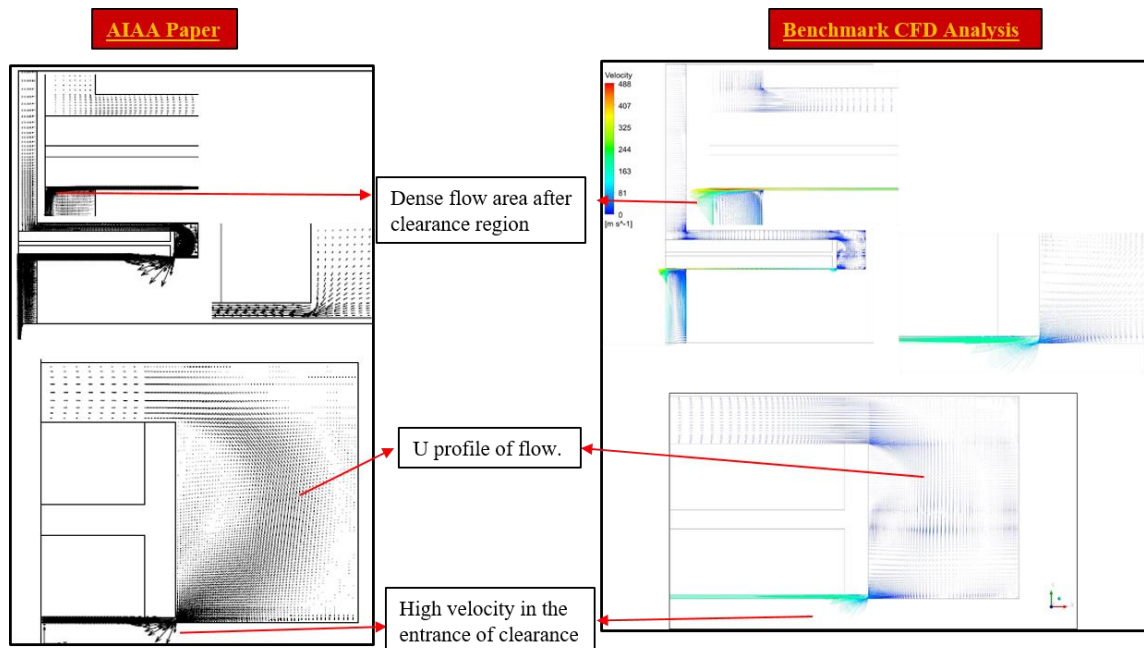


**Figure 5.13: Velocity vector plots of AIAA paper (left) [1] and benchmark study (right)**

Velocity streamlines are shown for benchmark study in Figure 5.14. Flow smoothly reaches to upper side of cloth seal and turns from first corner. It directs through lateral gap after second corner and accumulates in a U-profile in lateral region. Flow speeds up drastically in clearance region due to narrow cross-section. In benchmark CFD analysis, a recirculation region is observed on downstream side. The difference is a result of the definition of the outlet boundary.

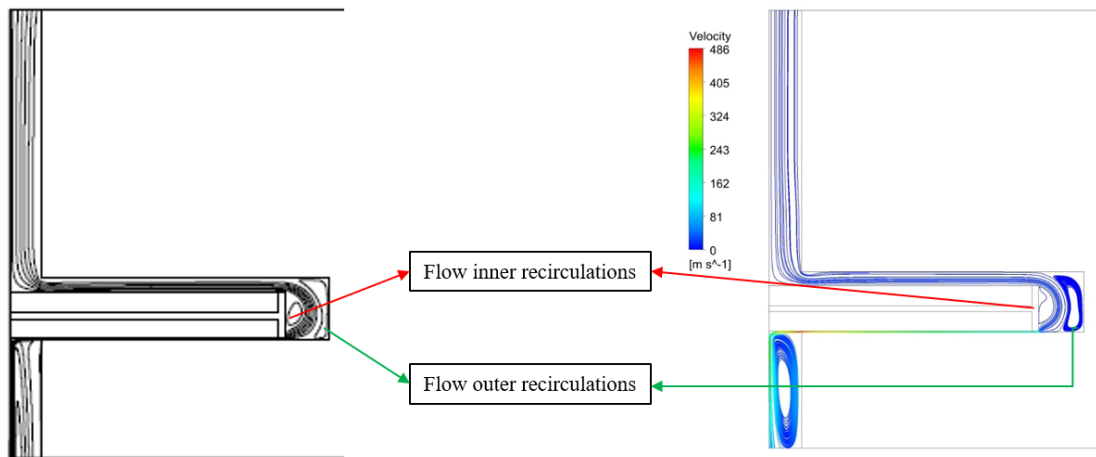


**Figure 5.14: Velocity streamlines of AIAA paper (left) [1] and benchmark study (right)**

Temperature distribution plots are shown in Figure 5.15. Temperature profile o are compared. Benchmark study provides realistic solid temperature distribution with smooth temperature raise from upstream side to downstream side in solid region. However, since boundary conditions of solid region are unknown in the study [1], there is a temperature distribution difference in solid region. The reason for such a difference might be due to temperature boundary condition in upper surface of solid region.

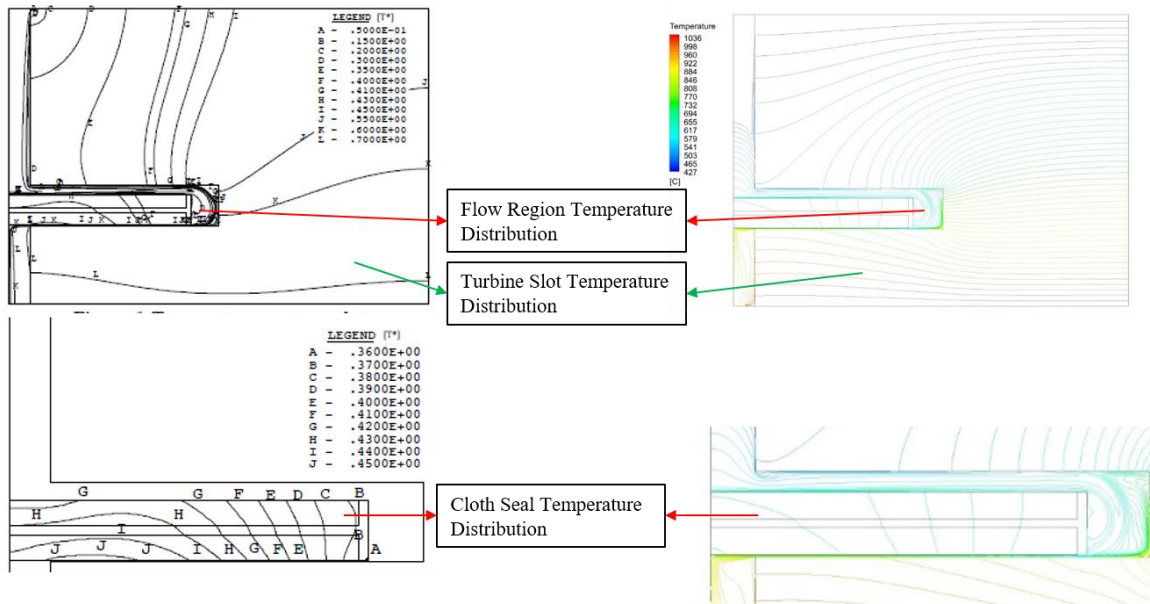


**Figure 5.15: Temperature contour plots of AIAA paper (left) [1] and benchmark study (right)**

Pressure distribution of flow region in benchmark CFD model is shown in Figure 5.16. Significant portion of the pressure drop is observed in the clearance region due to choking zone.

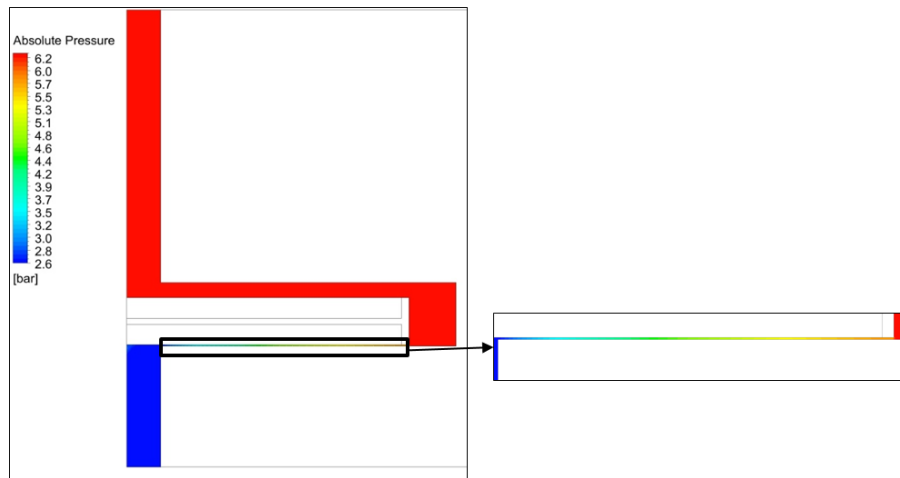


**Figure 5.16: Pressure profile of benchmark study**

Figure 5.17 presents temperature distribution of benchmark CFD&CHT analysis. Coolant air enters the flow region with the temperature lower than 500 C. Its temperature increases up to 600 C while reaching clearance region. Air temperature exceeds 800 C after clearance region. Cloth seal temperature reaches up to 700 C, therefore, materials for cloth weave and metal shim should be selected from the materials operating in high-temperature (such as Haynes or Inconel series).

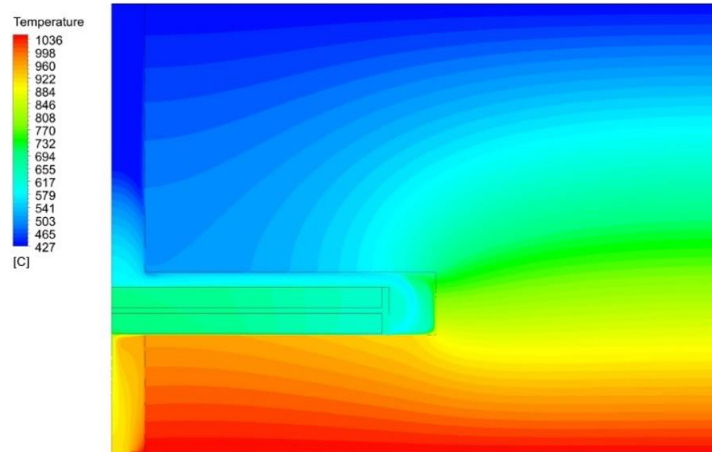


**Figure 5.17: Temperature profile of the benchmark study**

### **5.3 Cloth Seal CFD Analyses**

After cloth weave CFD analyses are correlated with test results, resistance coefficients are obtained for different directions and pressure drop levels. Steady-state CFD simulations for cloth seals are completed to observe leakage performance and flow distribution. Parametric CFD model geometry is generated in ANSYS Design Modeller. This model provides easy and quick change in geometric dimensions. Meshing process is also automated by defining number of nodes in divided edges, therefore, mesh of the model can be automatically updated. In order to correlate leakage rates of test results with CFD models, operating clearance is changed iteratively. In both baseline and offset positions, operating clearances are changed in CFD models until test results and CFD results are matched. In CFD analyses, the operating fluid is air which is modeled as compressible and turbulent. The turbulence flow model is set to standard k- $\epsilon$  turbulence model with 5% turbulence intensity at inlet and outlet faces of the fluid domain. Static pressure and temperature values are defined on the inlet boundary. Opening pressure and temperature boundary conditions are applied for outlet boundary. In the porous cloth weave domain, calibrated resistance coefficients are applied as anisotropic. Therefore, resistance coefficients are different in different directions.

### 5.3.1 Cloth Seal CFD Analysis in Test Conditions

In order to find operating clearance for a pressure drop, leakage rates of test and CFD results are matched. Mesh details of cloth seal CFD analysis are illustrated in Figure 5.18. 160,000 elements are applied in mesh models. Mesh is refined in clearance zone to capture high gradients of flow properties.

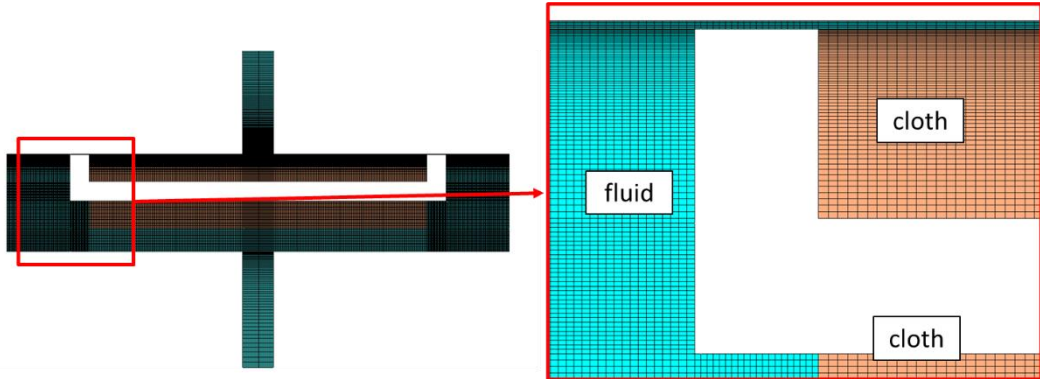


Figure 5.18: Cloth seal CFD model mesh details

CFD analyses are performed as steady-state condition in CFX with a 3D model. The operating conditions of CFD analyses are the same as leakage test conditions. Cloth weave region is modeled with porous medium approach.

Position	T <sub>up</sub> [C]	P <sub>up</sub> [kPa]	P <sub>down</sub> [kPa]	ΔP [kPa]	Offset Level [mm]	Operating Clearance [mm]	Leakage Flow Rate [g/s]
Baseline	25	441	101	340	0	0.0195	6.78
Offset					0.2	0.0103	4.03

Table 5.6: Boundary conditions and results of CFD analysis of cloth seal (leakage test condition)

In Figure 5.19, pressure contours of cloth seal design are illustrated. Normalized pressure is calculated as (Normalized Pressure = (Pressure – P<sub>min</sub>) / (P<sub>max</sub> – P<sub>min</sub>)). Pressure contours are plotted with 16 intervals. In Figure 5.19 (a), high-pressure drop occurs in the choking zone. The pressure is almost constant except choking zone. In Figure 5.19 (b),

pressure drop is observed in both choking zone and porous cloth region. This may be a result of the contraction around the slot edges which close to downstream side.

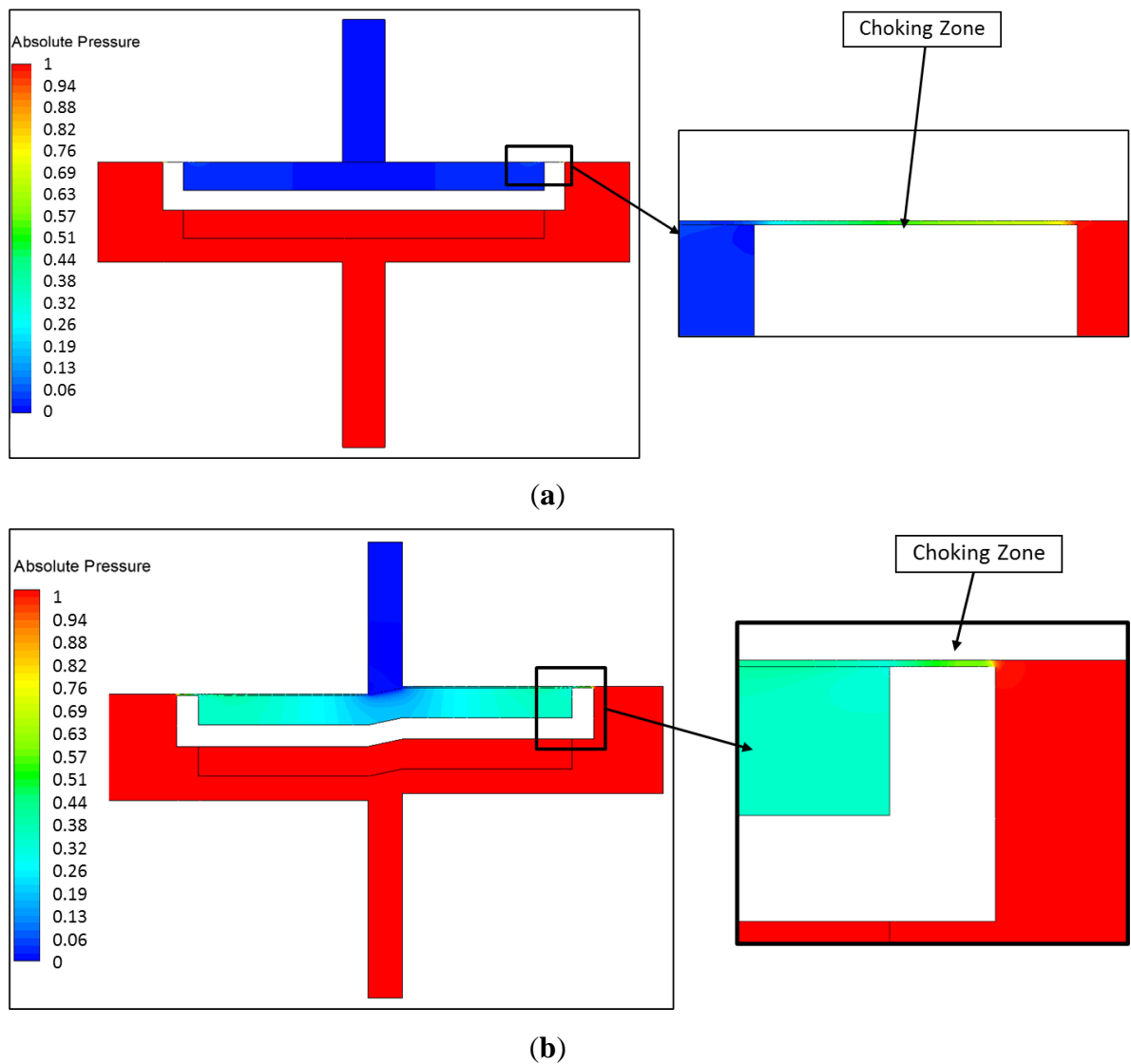


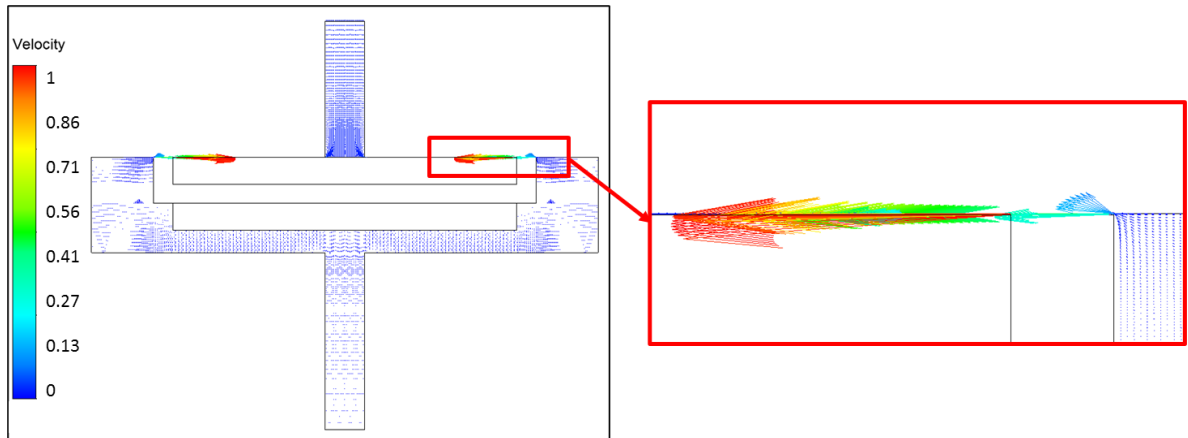
**Figure 5.19: Normalized pressure distribution of cloth seal design in test conditions**

**a) baseline position b) offset position**

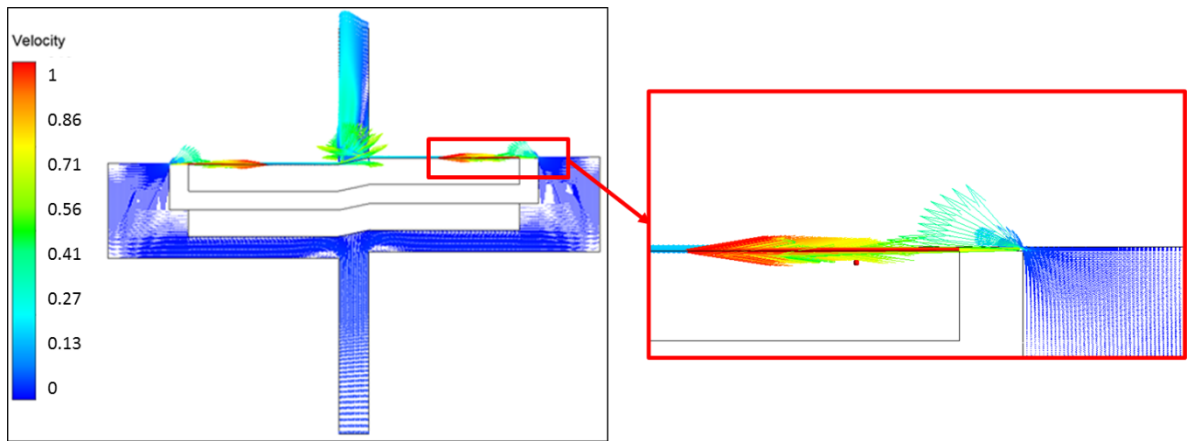
The velocity vectors and streamlines are illustrated in Figure 5.20 and Figure 5.21. Normalized velocity is calculated as (Normalized Velocity = Velocity /  $V_{max}$ ). Mass flow rate which is equal to the product of density, velocity, and flow area, remains constant due to the conservation of mass. Area and density in choking zone are less than upstream flow region. Therefore, flow accelerates at the choking zone.

The flow smoothly directs through the choking zone from the upstream for baseline and offset positions in Figure 5.21. Then, the flow extends to the downstream region. Due

to the offset position, streamlines are not symmetric towards outlet (Figure 5.21 (b)). A recirculation area is observed on one side of the downstream channel.



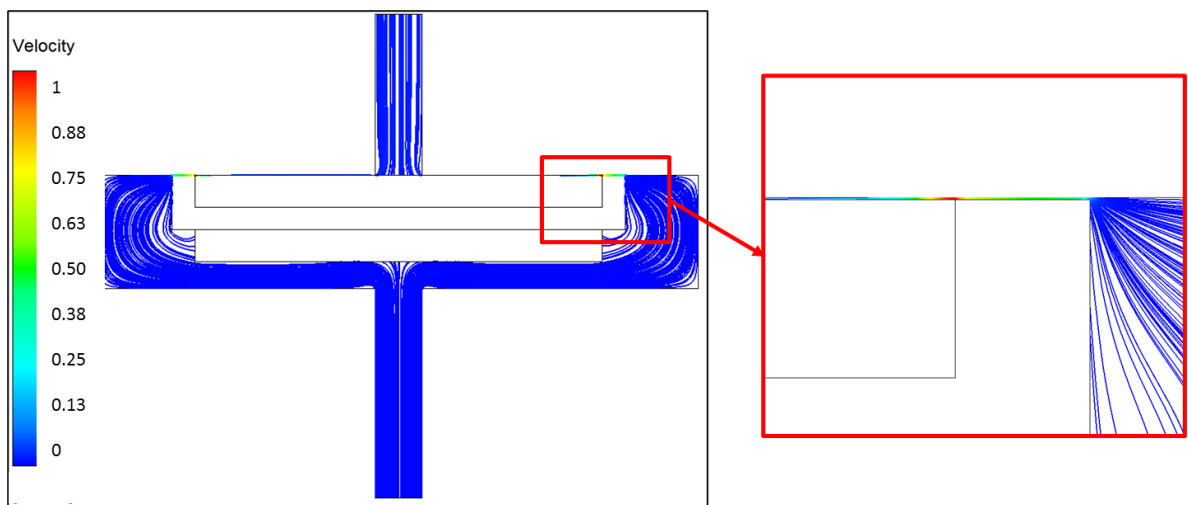
(a)



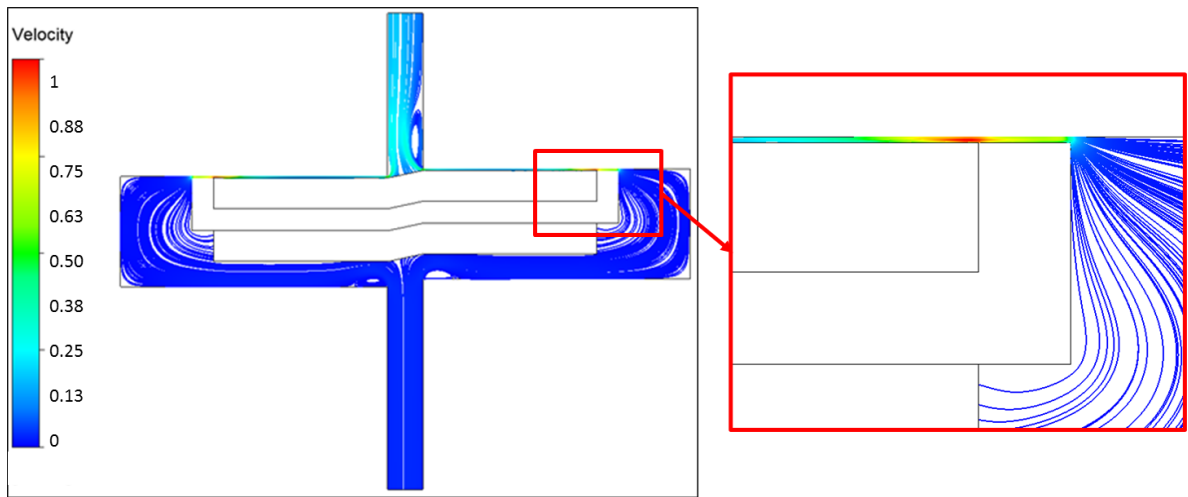
(b)

**Figure 5.20: Normalized velocity vectors of cloth seal design in test conditions**

a) baseline position b) offset position



(a)

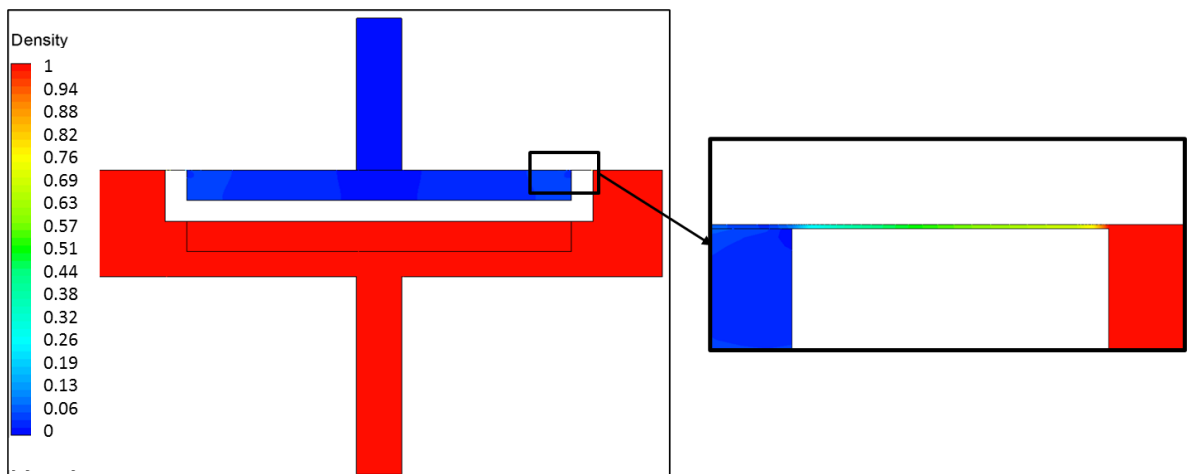


(b)

**Figure 5.21: Normalized velocity streamlines of cloth seal design in test conditions**

**a) baseline position b) offset position**

The density contours are shown in Figure 5.22. Normalized density is calculated as  $(\text{Normalized Density} = (\text{Density} - \rho_{\min}) / (\rho_{\max} - \rho_{\min}))$ . As a characteristic of a compressible flow, the density is a function of the pressure. For this reason, density distribution shows same trend as pressure distribution. The density mostly changes at the choking zone where high-pressure gradients occur.



(a)

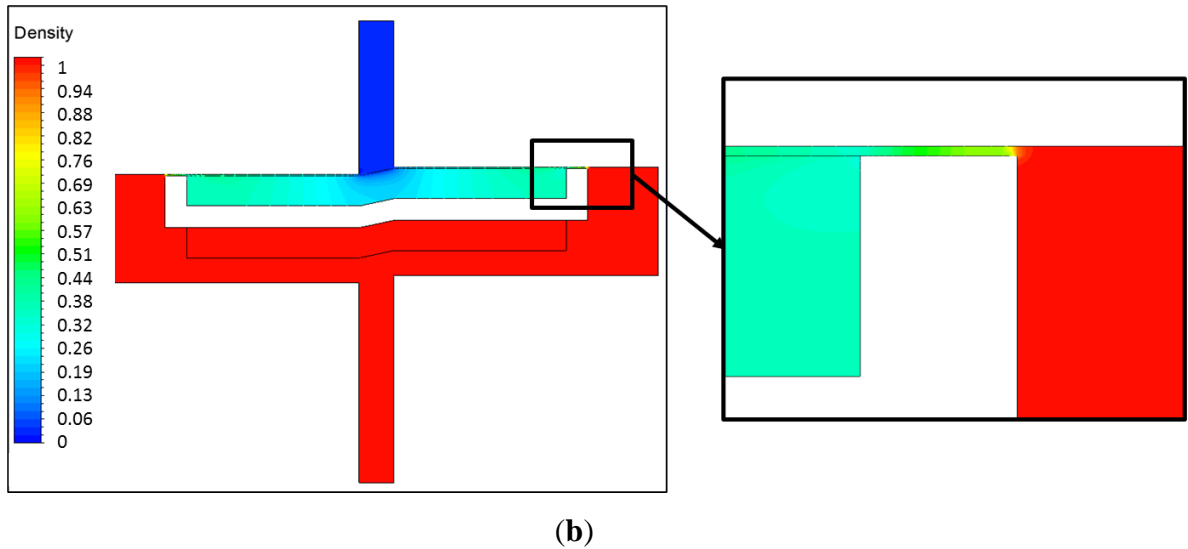


**Figure 5.22: Normalized density distribution of cloth seal design in test conditions**  
a) baseline position b) offset position

### 5.3.2 Cloth Seal CFD Analysis in Turbine Conditions

In previous section, cloth seal CFD analyses are performed in test conditions to find operating clearances. These operating clearances are used in CFD analysis of turbine operating conditions. Same CFD geometries are used in test and turbine condition analyses. The flow is modeled as compressible and turbulent with standard k- $\epsilon$  model. Static pressure and temperature are defined for inlet whereas opening pressure and temperature are given for outlet boundary. The results of baseline and mismatch positions are tabulated in Table 5.7. Upstream and downstream pressure levels are different from test condition analyses. The pressure and temperature of boundary conditions are defined from an industrial gas turbine data, therefore, they are excluded from table. The pressure drop level is the same as test condition CFD analyses.

Position	$\Delta P$ [kPad]	Offset Level [mm]	Operating Clearance [mm]	Leakage Flow Rate [g/s]
Baseline	340	0	0.0195	213.6
Offset		0.2	0.0103	140.5

**Table 5.7: Boundary conditions and results of CFD analysis of cloth seal (turbine condition)**

In Figure 5.23, pressure contours of cloth seal design are illustrated. Normalized pressure is calculated as  $(\text{Normalized Pressure} = (\text{Pressure} - P_{\min}) / (P_{\max} - P_{\min}))$ . In Figure 5.23 (a), high-pressure difference occurs in the choking zone. The pressure is almost constant except choking zone. In Figure 5.23 (b), pressure mostly changes in choking zone and a portion of pressure drop is observed in porous cloth region.

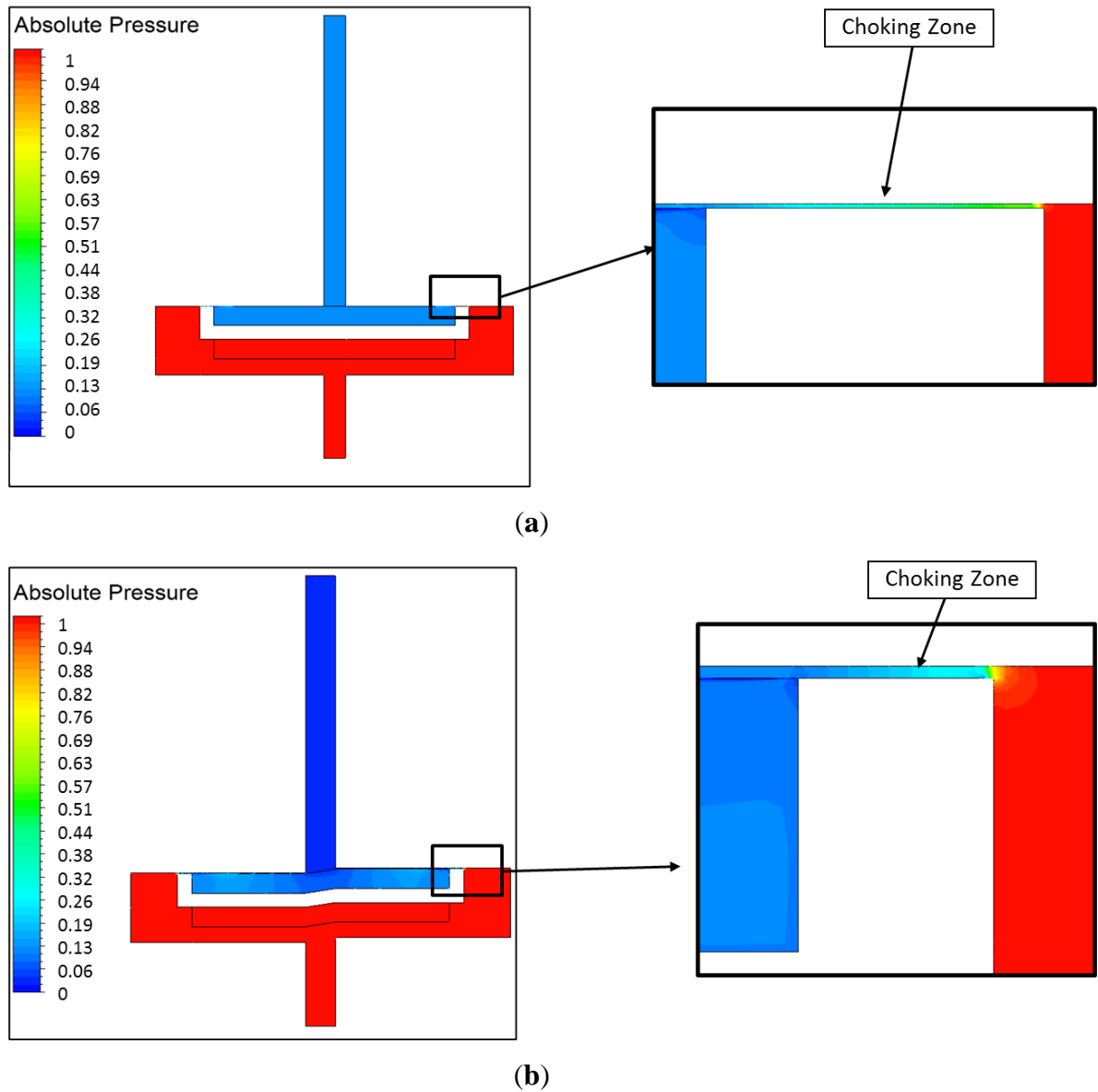


**Figure 5.23: Normalized pressure distribution of cloth seal design in turbine operating conditions**  
a) baseline position b) offset position

The velocity vectors and streamlines are illustrated in Figure 5.24 and Figure 5.25. Normalized velocity is calculated as  $(\text{Normalized Velocity} = \text{Velocity} / V_{\max})$ . The flow accelerates at the entrance of clearance due to conservation of mass. Similar to test conditions, the flow smoothly directs through the choking zone from the upstream for

baseline and offset positions in Figure 5.25. Then, the flow extends to the downstream region. Due to the offset configuration, streamlines are not symmetric towards the outlet (Figure 5.25 (b)).

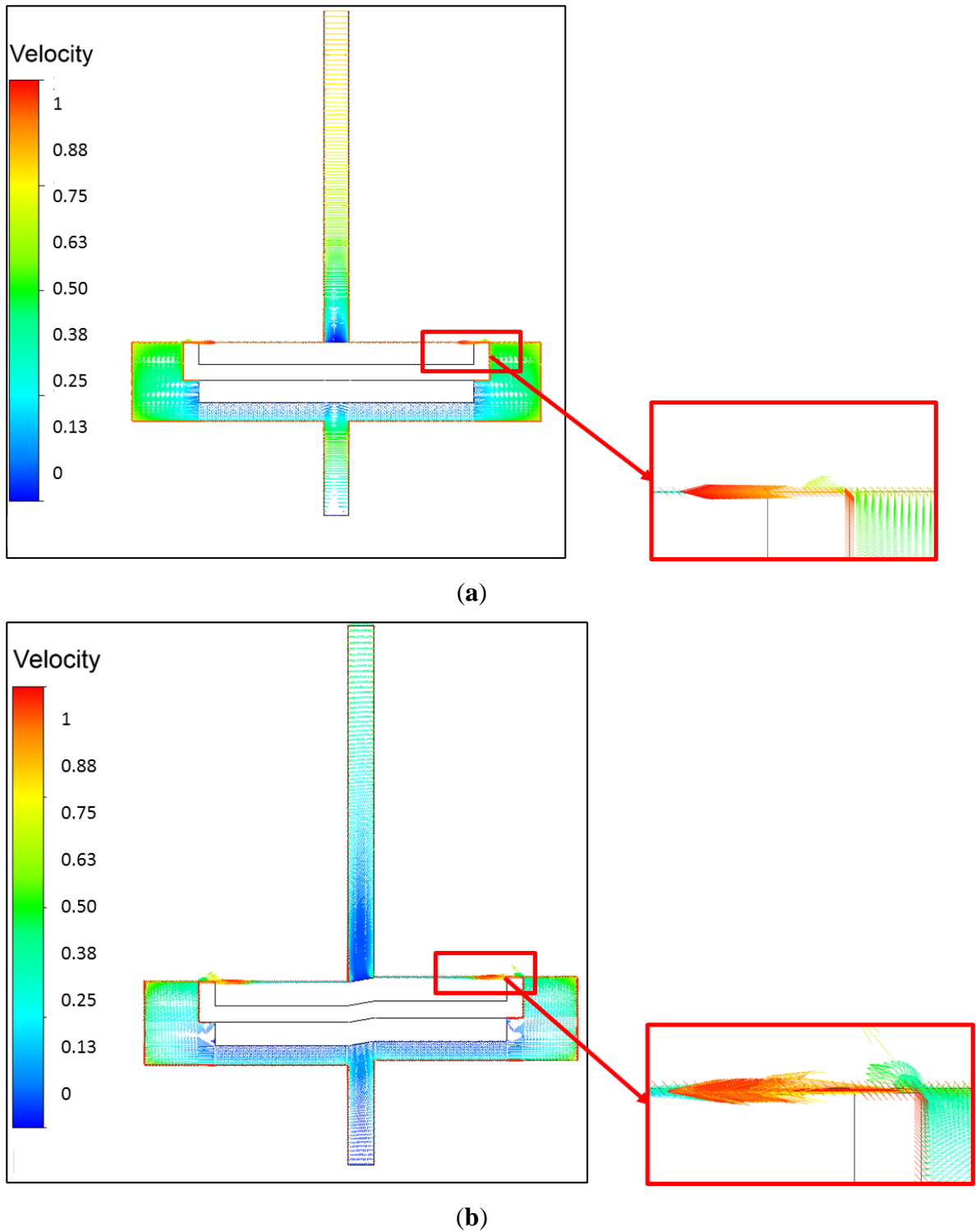
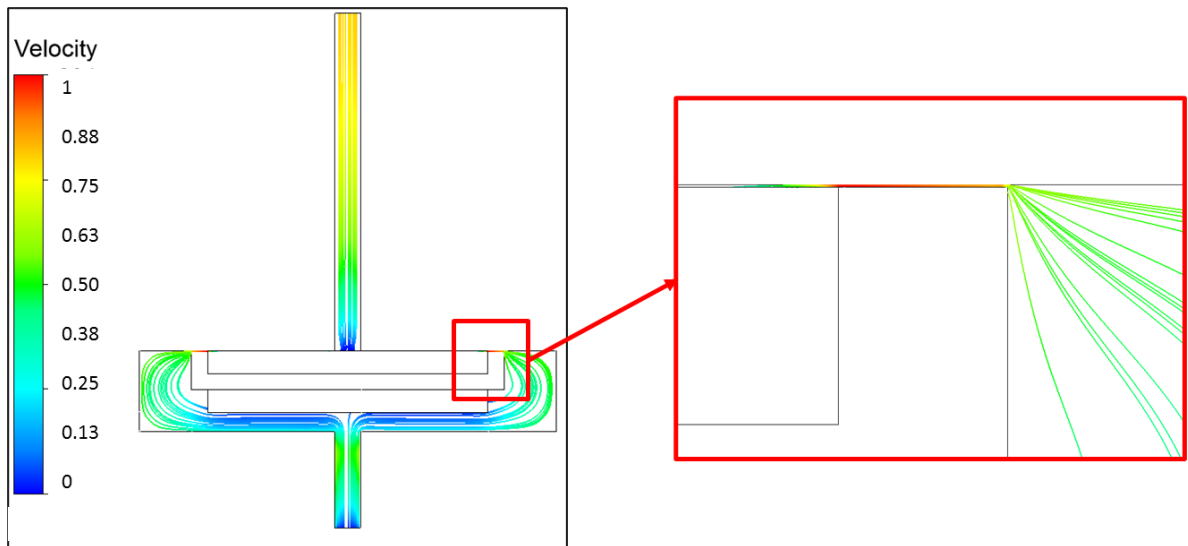
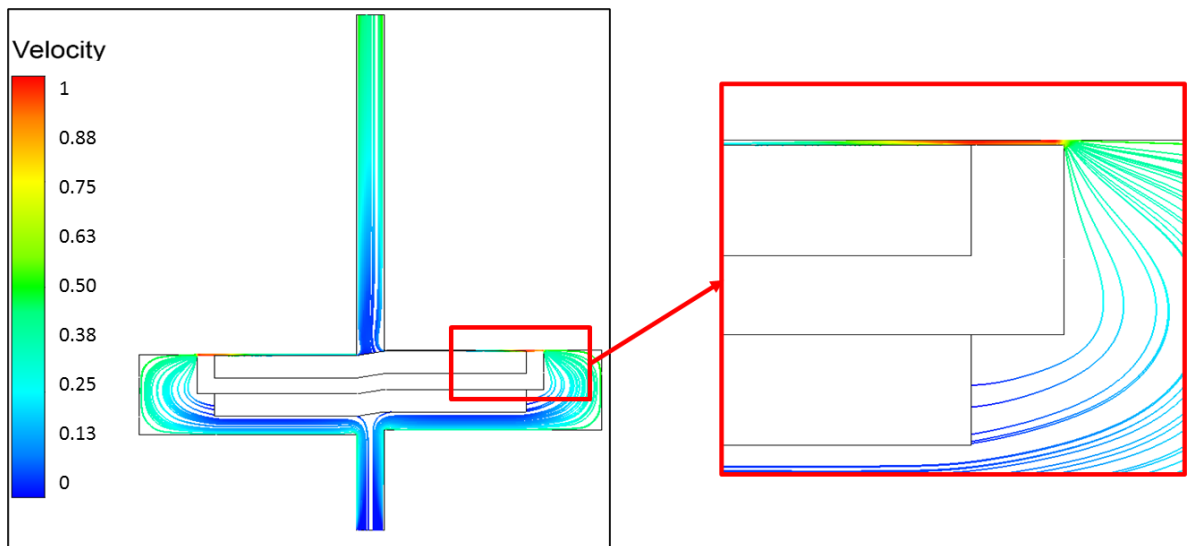


**Figure 5.24: Normalized velocity vectors of cloth seal design in turbine operating conditions**  
a) baseline position b) offset position



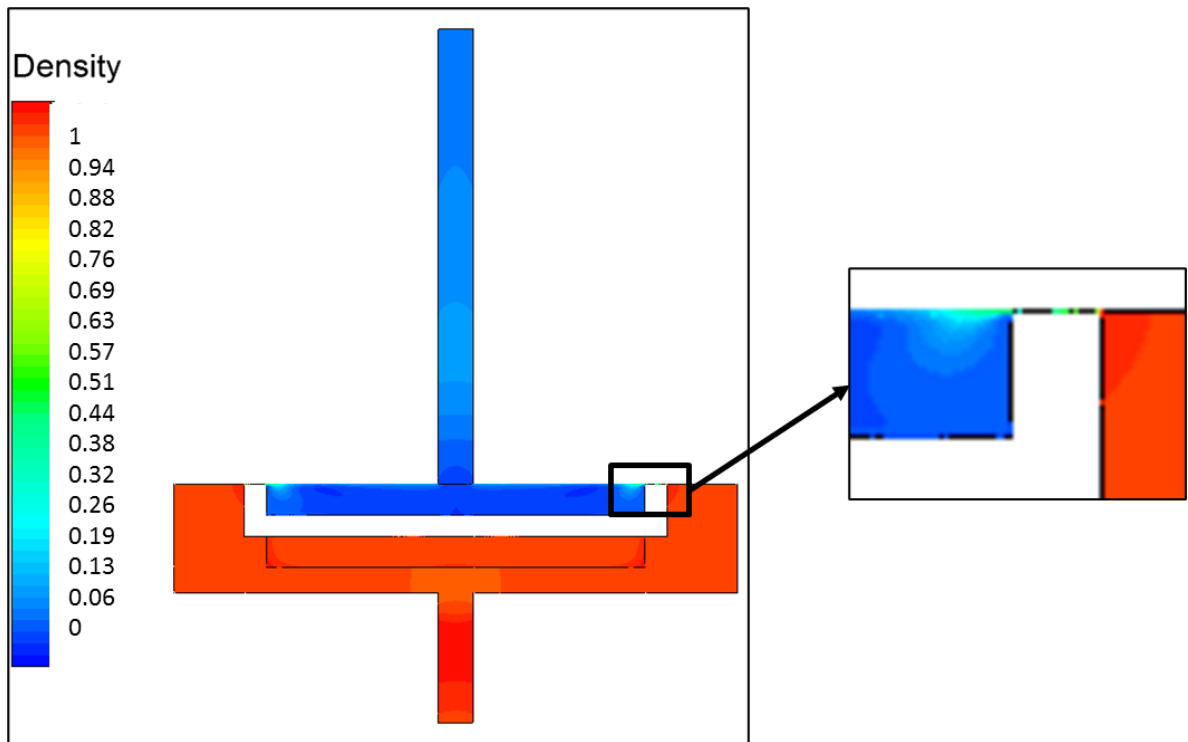
(a)



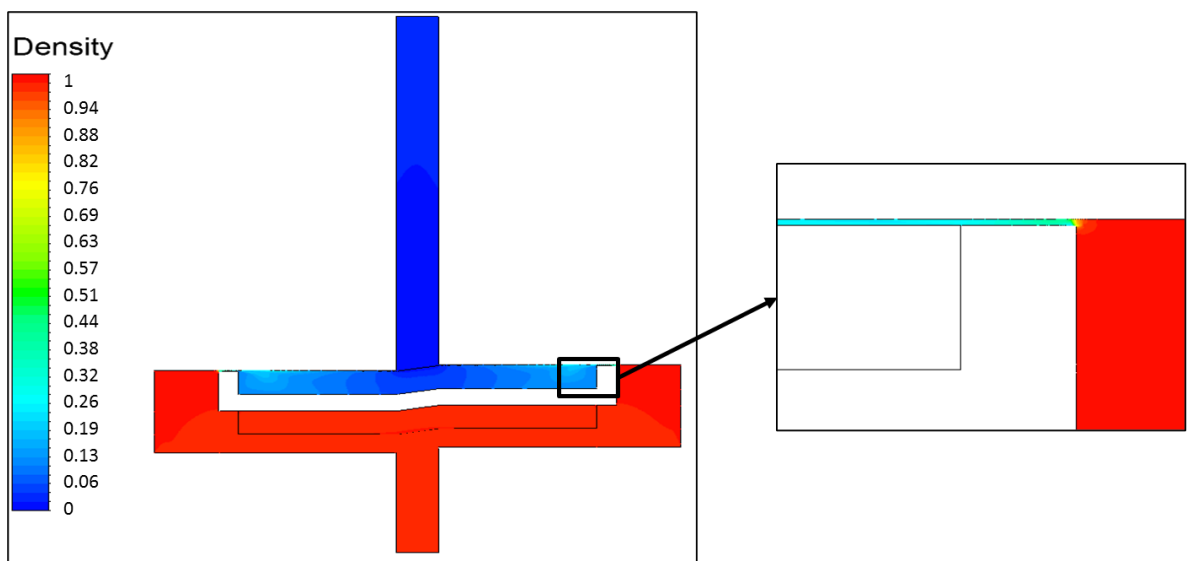
(b)

**Figure 5.25: Normalized velocity streamlines of cloth seal design in turbine operating conditions**  
**a) baseline position b) offset position**

The density contours are shown in Figure 5.26. Normalized density is calculated as  $(\text{Normalized Density} = (\text{Density} - \rho_{\min}) / (\rho_{\max} - \rho_{\min}))$ . The density follows a similar trend with pressure. It mostly changes at the choking zone where high-pressure gradients occur.



(a)



(b)

**Figure 5.26: Normalized density distribution of cloth seal design in turbine operating conditions**

**a) baseline position b) offset position**

Cloth seal CFD analyses provide the leakage rate in turbine operating conditions with calibrated flow resistance coefficients and operating clearance. In order to obtain the increase of overall power output with cloth seal application, a system level analysis of gas turbine needs to be performed. A flowchart of a system-level assessment for a gas turbine is illustrated in Appendix D.

## 6 DESIGN OF EXPERIMENTS

In this chapter, The optimized output is called as *objective* and inputs which have impact on objective is named as *parameters*. Discrete parameters are defined in a certain number of values. Such values are named as *levels*. Equivalent gap is selected as objective to compare cloth seal leakage performance for various designs and boundary conditions. Once the leakage rate is obtained, equivalent gap is estimated. To understand the effects of several cloth seal parameters on equivalent gap, a systematic design of experiments is generated. Steps of DoE study are explained as below:

- Identification of the parameters affecting the leakage performance
- Selection of the method for screening experiments
- Establishing an experimental design for screening experiments
- Pareto chart and identification of strong parameters
- Comparison test results with the data existing in the literature
- Establishing experimental design for main experiments
- Pareto chart and a closed-form equation for strong parameters

### **Cloth Seal Leakage Performance Parameters**

Parameters that affect the leakage performance are listed in Table 6.1. Geometric parameters of the cloth seal are illustrated in Figure 6.1. In order to perform a high-resolution DOE study, the number of parameters should be reduced. Therefore, the last ten parameters (parameters 9–18) are fixed at common values based on engineering judgment and literature data. Cloth material is selected as cobalt-based alloy Haynes 25/L605 which has superior high temperature wear resistance and is used as common cloth material [7],[11]. Haynes alloy 188 has good oxidation resistance for high temperature and is commonly used as shim material in cloth seals [11]. The data provided in the literature indicates that Dutch Twill with  $30 \times 250$  per inch density provides better leakage performance and is commonly used as the cloth of choice in cloth seals [10]. Therefore, Dutch Twill is selected as the cloth weave type with  $30 \times 250$  density which also determines cloth weave thickness, warp and shute diameters. Spot weld diameter is

selected by considering integrity to cloth wires and minimum additional stiffness. Slot height is selected much higher than cloth seal thickness as commonly practiced allowing easy blind engine assembly. Due to experimental limitations and limited effect on elastic modulus, the effect of temperature is omitted in this study. The remaining eight parameters are considered to have a significant effect on leakage performance and are selected for a higher resolution DoE study. In order to measure leakage performance, the objective of the DoE study is selected as the leakage rate that the mass flow rate leaks through the cloth seal.

No	Parameter Name	Abbreviation	No	Parameter Name	Abbreviation
1	Slot depth	SD	10	Cloth material	CM
2	Cloth width	CW	11	Cloth weave thickness	CWT
3	Gap	GP	12	Dia. of warp fiber	DW
4	Shim thickness	ST	13	Dia. of shute fiber	DS
5	Surface roughness	SR	14	Weave type	WT
6	Pressure drop	PD	15	Weave density	WD
7	Offset	OF	16	Spot weld dia.	SW
8	Mismatch	MI	17	Slot height	SH
9	Shim material	SM	18	Temperature	TE

**Table 6.1: Candidate parameters for cloth seal leakage performance study.**

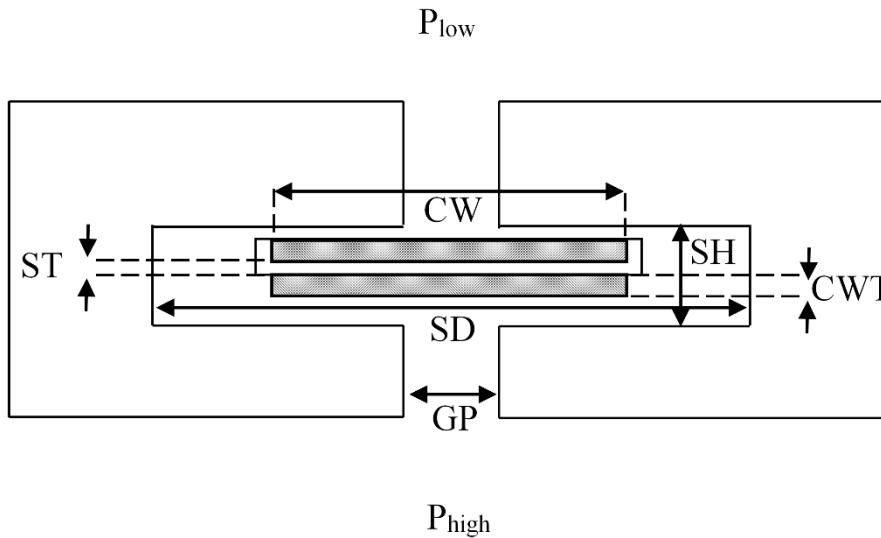


**Figure 6.1: Cloth seal geometric parameters.**

## 6.1 Screening Experiment Design

Even though the number of parameters is reduced to eight, the derivation of a nonlinear relation between eight parameters and leakage rate requires a high number of

experiments for a high-resolution study. Therefore, screening experiments are performed to determine the strong parameters with a high effect on leakage performance. The least significant parameters are eliminated for final DoE study.

If a full factorial experiment design is used, all experiment design combinations should be tested. This requires  $2^8 = 256$  experiments for two-level experiment designs, while the number rises to  $3^8 = 6561$  for three-level experiment designs. As a result, full factorial experiment design demands very long test period and high cost. Therefore, the number of experiments should be further reduced using a fractional factorial experiment design for screening experiments. It is straightforward and simple to design in the chosen levels of parameters. Minitab software is used for Fractional Factorial Design.

In order to investigate the selected eight parameters, a two-level Resolution IV experiment design is applied. Therefore, the number of experiments is reduced to a significant amount while using a high number of parameters. Table 6.2 shows the selected levels for the eight parameters. Sixteen experiments are prepared to analyze the effect of eight parameters in two-levels. They are tested with the parameter levels as tabulated in Table 6.3.

No	Parameter Name	Unit	Abbreviation	Level
1	Slot depth	mm	SD	32 - 36
2	Cloth width	mm	CW	22 - 26
3	Gap	mm	GP	4 - 8
4	Shim thickness	mm	ST	0.254 - 0.508
5	Surface roughness	$\mu\text{m}$	SR	0.8 - 6.4
6	Pressure drop	kPad	PD	206.8 – 482.6
7	Offset	mm	OF	0 - 0.2
8	Mismatch	$^\circ$	MI	0 - 0.6

**Table 6.2: Parameters of screening experiments with levels.**

Exp. No.	SD [mm]	CW [mm]	GP [mm]	ST [mm]	SR [ $\mu\text{m}$ ]	PD [kPad]	OF [mm]	MI [ $^\circ$ ]
1	32	22	4	0.254	0.8	206.8	0	0
2	36	22	4	0.254	0.8	482.6	0.2	0.6
3	32	26	4	0.254	6.4	206.8	0.2	0.6
4	36	26	4	0.254	6.4	482.6	0	0
5	32	22	8	0.254	6.4	482.6	0.2	0

6	36	22	8	0.254	6.4	206.8	0	0.6
7	32	26	8	0.254	0.8	482.6	0	0.6
8	36	26	8	0.254	0.8	206.8	0.2	0
9	32	22	4	0.508	6.4	482.6	0	0.6
10	36	22	4	0.508	6.4	206.8	0.2	0
11	32	26	4	0.508	0.8	482.6	0.2	0
12	36	26	4	0.508	0.8	206.8	0	0.6
13	32	22	8	0.508	0.8	206.8	0.2	0.6
14	36	22	8	0.508	0.8	482.6	0	0
15	32	26	8	0.508	6.4	206.8	0	0
16	36	26	8	0.508	6.4	482.6	0.2	0.6

**Table 6.3: Screening experiments.**

The high and low levels of the parameters are selected to cover typical turbine applications and pressure drop levels for common cloth seal operation ranges. The significance of parameters is analyzed with a Pareto chart. Leakage rate trends with respect to levels of each parameter are examined in an effect chart.

Similar to the previous studies [9],[10] applied, leakage rates are nondimensionalized and normalized by dividing the leakage rates with that of the rigid seal under baseline (without offset and mismatch) position at the condition that pressure drop is equal to downstream pressure ( $P_{low}/P_{high} = 0.5$ ). The parameters for the baseline rigid seal test are slot distance = 32 mm, shim width = 26 mm, gap = 4 mm, shim thickness = 0.254 mm, surface roughness = 6.4  $\mu\text{m}$ , pressure drop = 101.3 kPad, offset = 0 mm, and mismatch = 0°.

Figure 6.2 shows the relative effects of parameters in a Pareto Chart. Alpha is the statistical significance level which is the probability of the study rejecting the null hypothesis. Its value is selected as 0.05. Results show that four parameters among the others stand out. These strong parameters are pressure drop, cloth width, slot depth and offset.

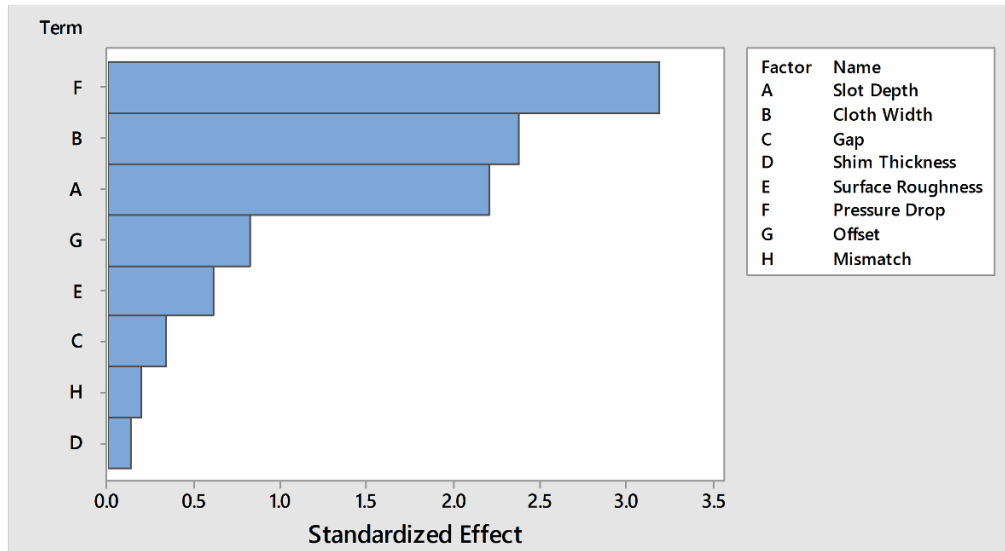


**Figure 6.2: Pareto Chart for Screening Experiments**

The main objective of the screening results is to determine strong and weak parameters and reduce the number of experiments for the main experimental study. Therefore, these four parameters are selected for detailed study in the main experiments. Surface roughness, gap, mismatch, and shim thickness appear relatively weaker parameters to influence leakage performance. As expected, pressure drop has the highest impact on leakage. The standardized effect for pressure drop is 3.186. The leakage performance is negligibly affected by shim thickness. The standardized effect is calculated as 0.133 for shim thickness.

The effect plot for leakage rate is illustrated in Figure 6.3. Eight parameters are shown with their trends. Strong parameters have higher leakage differences between high and low levels. The dimensional changes in geometric parameters are shown as diagrams in Figure 6.4.

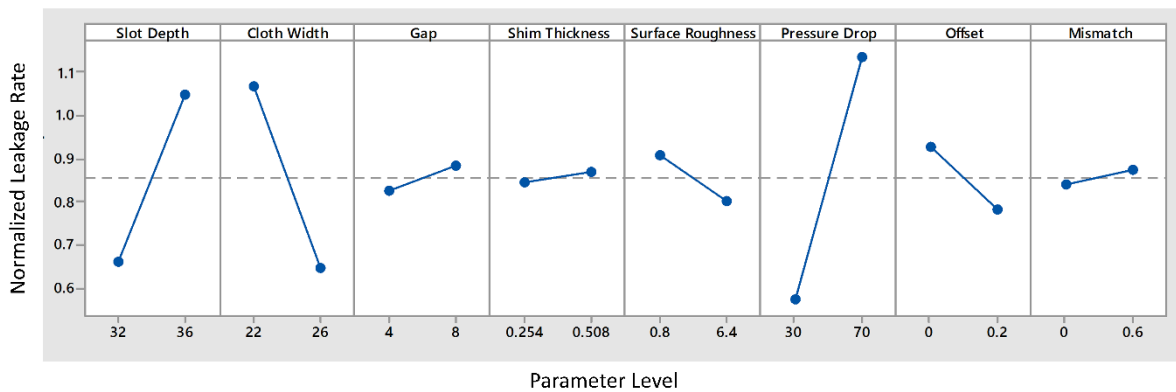


**Figure 6.3: The effect plots for normalized leakage rate (screening experiments).**

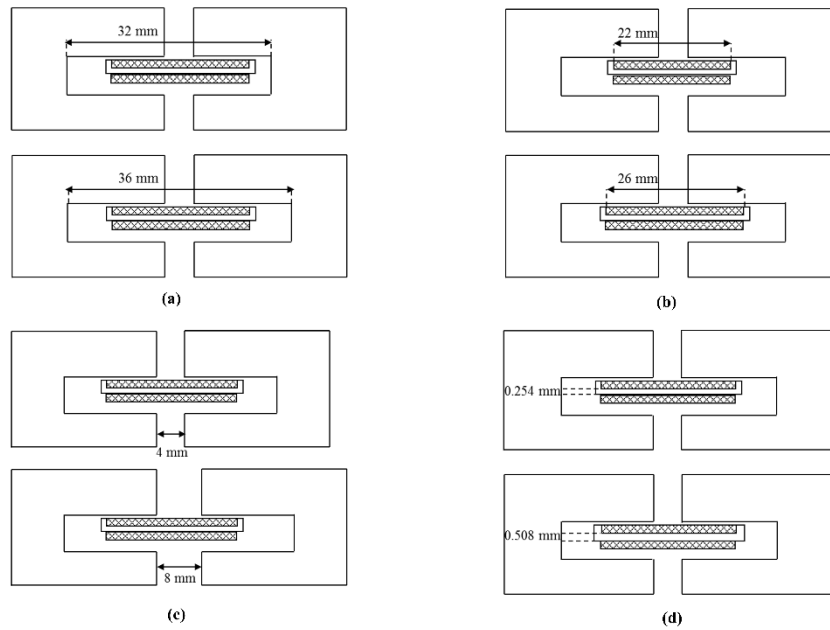


**Figure 6.4: Diagrams for dimensional changes, (a) slot depth; (b) cloth width; (c) gap; (d) shim thickness.**

As expected, the leakage rate significantly increases with a higher pressure drop. This is in line with the reports in the literature [10]. Pressure drop of 482.6 kPad (70 psid) experiments have approximately double of mean leakage rate compared to pressure drop of 206.8 kPad (30 psid).

The reducing cloth width increases leakage rate by two-thirds since the area resisting the flow decreases with reducing cloth width. There is no published data about the effect of cloth width on cloth seal leakage performance. This situation also explains the leakage rise with a higher gap distance. Clearance area between the cloth seal and slot is reduced by increasing the gap value.

36 mm slot depth experiments have a 60% higher average leakage rate than those with 32 mm slot depth. There is no published data about the effect of slot depth on cloth seal leakage performance. The slot depth considerably affects the flow pattern in the zone between shim tabs and lateral slot walls. Flow is limited with narrower lateral areas; therefore, leakage is diminished by the shorter distance between slots.

Leakage rate is decreased a little with offset condition. It is thought that in offset condition, the cloth seal improves its contact at one side while another side still maintains

its contact with the seating surface without losing choking points at the tabs due to its flexibility.

The leakage rate is increased with a shallow gradient by rising shim thickness. Leakage rate of 0.508 mm shim thickness is 2.8% higher than 0.254 mm shim thickness. This is somehow expected due to the fact that thicker shim is less flexible. Aksit et. al. [9] also stated that lower shim thickness provides higher flexibility leading to slightly better performance.

Roughness has reduced effect in the working range. There is no published data about the effect of roughness on cloth seal leakage performance. This reduction may be explained as a result of higher friction losses and higher surface turbulence. Rough surface leads to the absorption of more energy from the fluid.

Figure 6.5 illustrates the normalized leakage rate of sixteen experiments which are tabulated in Table 6.3. The lowest leakage rate is obtained in Exp. No. 15 and the highest leakage rate is observed in Exp. No. 14. Figure 6.5 shows that Exp. No. 15 has an 86% lower leakage rate than Exp. No. 14. This result emphasizes that the pressure and geometric dimensions may have a big impact on leakage rate of the cloth seal.

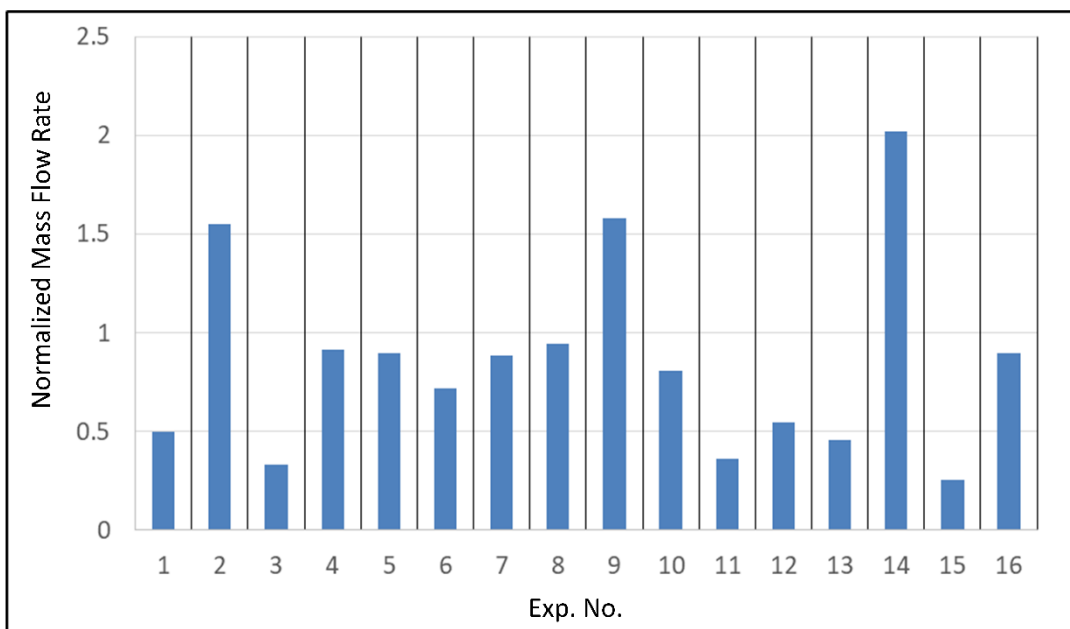


**Figure 6.5: Normalized leakage rate of experiments (screening experiments).**

The rigid seals are widely used as conventional sealing technology. Therefore, its leakage rate under nominal conditions (no offset, no mismatch) has been selected as the

baseline to normalize all other data. In Figure 6.6 and Figure 6.7, the equivalent gap rates are nondimensionalized and normalized by dividing the equivalent gap rates with that of the rigid seal under baseline (no offset, no mismatch) position and  $P_{low}/P_{high} = 0.5$  condition. To facilitate meaningful comparison, the test conditions of the rigid seal (pressure ratio, temperature, offset, and mismatch) are kept the same with the literature [9],[10]. If a cloth seal design has a normalized equivalent gap less than 1, its leakage performance is better than the baseline rigid seal.

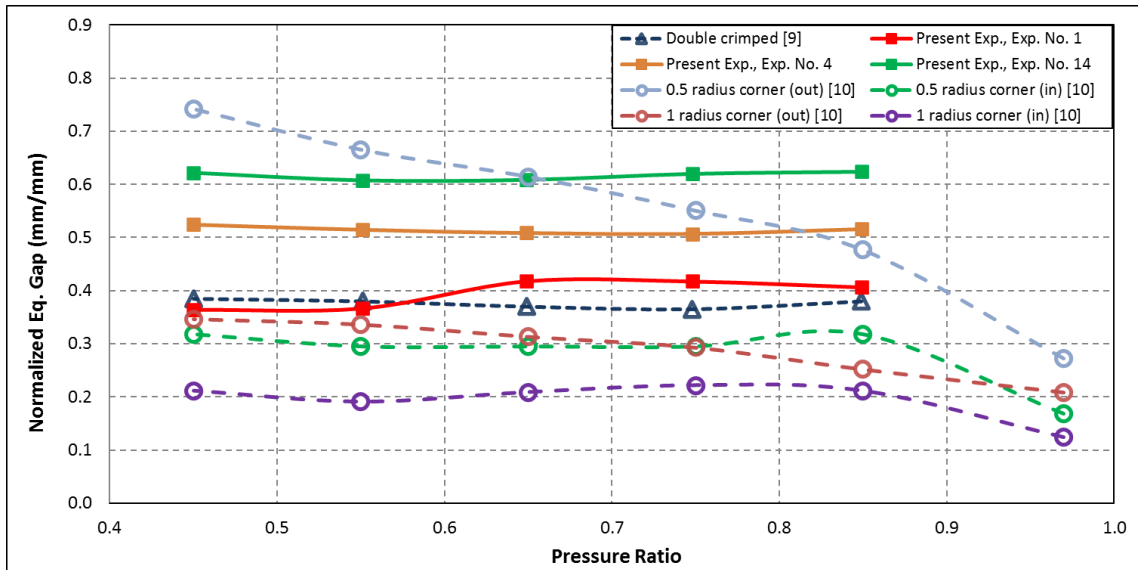


Figure 6.6: Normalized equivalent gap data (baseline condition).

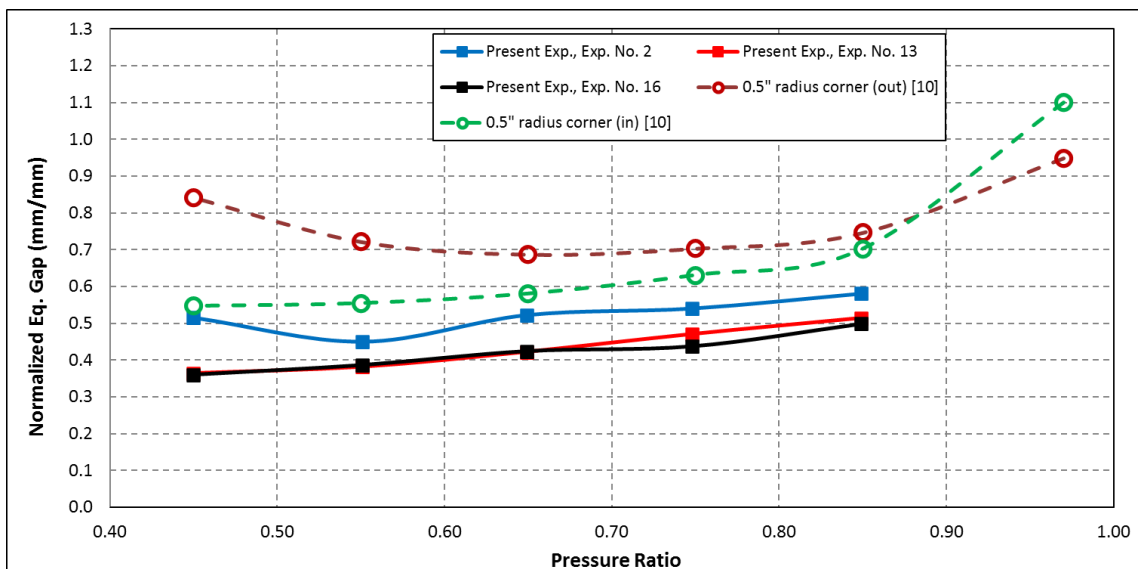


Figure 6.7: Normalized equivalent gap data (offset and mismatch condition).

Leakage performance of selected experiments in terms of the normalized equivalent gap is illustrated and compared with previous studies [9],[10] in Figure 6.6 for baseline conditions. Cloth seals in Exp. No. 1, 4, and 14 have equivalent gap approximately 62%, 49%, 39% less than the baseline rigid seal (at PR = 0.5), respectively. Equivalent gap remains almost constant with respect to pressure ratio for Exp. No. 1, 4 and 14. The results of experiments follow similar trends with reported literature data for the cloth seal with double crimped shim cloth seal [9] and with the curved cloth seal when pressure load is applied from the inside of the corner [10]. Double crimped shim cloth seal [9] has overall an 0.254 mm thickness of shim which is bent from edges to create tabs. This design is similar to the design used in the present study. Radius corner seals [10] which comprise of cloth layer around the shim, are applied to a corner region. In Figure 6.6, the test conditions of the experiments (pressure ratio, temperature, offset, and mismatch) are kept the same with the literature [9],[10]. In Figure 6.7, the present study is compared with the literature [10] in terms of leakage performance at offset and mismatch conditions. This plot presents the test results for 0.2 mm offset and 0.6° offset and mismatch conditions. The data indicate that cloth seals under offset and mismatch conditions provide better leakage performance than comparable rigid seals under nicely aligned baseline conditions at 0.5 pressure ratio. The data also indicate that the normalized equivalent gap slightly decreases with decreasing the pressure ratio ( $P_{low}/P_{high}$ ) which means higher pressure drop. It is concluded that higher pressure drop causes flexible cloth seal to conform to the slot surfaces better and reduces the equivalent sealing clearance. Offset and mismatch values are 0.762 mm and 0.9° for curved cloth seal [10], respectively. Figure 6.7 indicates that the studied seal designs show slightly better performance than 0.5 in radius corner seals reported by Aksit et al. [9] under offset and mismatch conditions.

## **6.2 Main Experiment Design**

After strong parameters are determined through screening experiments, a detailed experimental design study is conducted. In screening experiments, a two-level factorial experiment design provides a linear change between parameters and leakage rate. In this condition, the derived leakage equation will be expressed as:

$$\dot{m} = \alpha_0 + \sum_{i=1}^k \alpha_i x_i + \varepsilon \quad (6.1)$$

To observe whether a nonlinear behavior occurs in the trend, a three-level experiment design with a midpoint is required. Therefore, a Box-Behnken experiment design is selected as the methodology for the main set of experiments. The Box-Behnken experiment design is rotatable, and quadratic effects are also considered for leakage rate of the parameters. After main experiments are completed, a four-dimensional response surface can be fitted with test leakage results. Box-Behnken design provides leakage equation in the form of

$$\dot{m} = \alpha_0 + \sum_{i=1}^k \alpha_i x_i + \sum_{i=1}^k \alpha_{ii} x_i^2 + \sum_{i < j} \sum \alpha_{ij} x_i x_j + \varepsilon \quad (6.2)$$

$\dot{m}$  is leakage rate,  $x_i$  is the parameters,  $a_i$  are the coefficients and  $\varepsilon$  is the error term.

The parameters and their levels are tabulated in Table 6.4. Based on the screening experiment results, the parameters are grouped as weak and strong. Four main strong parameters which are slot depth, cloth width, pressure drop, and offset, are selected for the main experiments. The weak parameters which are gap, shim thickness, surface roughness, and mismatch are fixed to the values as shown in Table 6.4. Only strong parameters are varied in order to reduce the number of experiments to a manageable size. The minimum and maximum levels of strong parameters are the same as the levels used in the screening experiments. Twenty-seven experimental designs are tested as shown in Table 6.5.

No	Parameter Name	Unit	Abbreviation	Level
1	Slot depth	mm	SD	32–34–36
2	Cloth width	mm	CW	22–24–26
3	Gap	mm	GP	4
4	Shim thickness	mm	ST	0.254
5	Surface roughness	μm	SR	6.4
6	Pressure drop	kPad	PD	206.8–344.7–482.6
7	Offset	mm	OF	0–0.1–0.2
8	Mismatch	°	MI	0

**Table 6.4: The parameters of the main experiments with levels.**

<b>Exp. No.</b>	<b>SD [mm]</b>	<b>CW [mm]</b>	<b>GP [mm]</b>	<b>ST [mm]</b>	<b>SR [<math>\mu</math>m]</b>	<b>PD [kPad]</b>	<b>OF [mm]</b>	<b>MI [°]</b>
1	32	22	4	0.254	6.4	344.7	0.1	0
2	32	26	4	0.254	6.4	344.7	0.1	0
3	32	24	4	0.254	6.4	344.7	0	0
4	32	24	4	0.254	6.4	344.7	0.2	0
5	32	24	4	0.254	6.4	206.8	0.1	0
6	32	24	4	0.254	6.4	482.6	0.1	0
7	34	24	4	0.254	6.4	206.8	0	0
8	34	24	4	0.254	6.4	482.6	0	0
9	34	24	4	0.254	6.4	206.8	0.2	0
10	34	24	4	0.254	6.4	482.6	0.2	0
11	34	22	4	0.254	6.4	206.8	0.1	0
12	34	26	4	0.254	6.4	206.8	0.1	0
13	34	22	4	0.254	6.4	482.6	0.1	0
14	34	26	4	0.254	6.4	482.6	0.1	0
15	34	22	4	0.254	6.4	344.7	0	0
16	34	26	4	0.254	6.4	344.7	0	0
17	34	22	4	0.254	6.4	344.7	0.2	0
18	34	26	4	0.254	6.4	344.7	0.2	0
19	34	24	4	0.254	6.4	344.7	0.1	0
20	34	24	4	0.254	6.4	344.7	0.1	0
21	34	24	4	0.254	6.4	344.7	0.1	0
22	36	22	4	0.254	6.4	344.7	0.1	0
23	36	26	4	0.254	6.4	344.7	0.1	0
24	36	24	4	0.254	6.4	344.7	0	0
25	36	24	4	0.254	6.4	344.7	0.2	0
26	36	24	4	0.254	6.4	206.8	0.1	0
27	36	24	4	0.254	6.4	482.6	0.1	0

**Table 6.5: Main experiments.**

The impact of parameters on the leakage performance is investigated with sensor measurements in the test rig. Leakage rates and pressure drop are measured for each set of experiments. No damage occurred in the cloth seal designs due to wear, pressure drop, offset, and mismatch conditions. Manufactured cloth seals perfectly handle stresses result from offset&mismatch and applied pressure.

After the experiments are completed, cloth seal leakage performance is evaluated as a function of pressure and geometric dimensions. Leakage rate is selected as the objective to plot the Pareto Chart and the Main Effect Plot. Various graphs are plotted to illustrate the effects of parameters on the leakage performance.

The main experiment combinations are selected based on the Box-Behnken experiment design. Twenty-seven experiments are conducted to generate the experimental data set to fit a closed-form equation. In order to check the validity and accuracy of the derived equation under different conditions, eight different combinations

have been used for confirmation experiments. Confirmation experiment combinations are selected so that none of them match the main experiments. Results of the main experiments are used for curve fit purposes. Once an equation has been fit, leakage (flow) rate estimates of this equation are compared with the actual test results obtained in the main experiments. The obtained equation is also applied for the confirmation experiments, and predictions of the fit equation are also compared with the confirmation test results. Table 6.6 compares the results for both main and confirmation experiments. It shows the error in terms of leakage rate between the closed-form equation predictions and experimental results. To improve the accuracy of the fit, equation fit has been repeated by selectively excluding outlier experiments. The row labeled as ‘without outlier’ presents the case, where all of the twenty-seven experiments are included in the fit to obtain the closed-form equation. Once the equation is derived, calculated leakage rates are compared with each of the twenty-seven main experiment results as well as the eight confirmation experiment results. The reported maximum error values are tabulated for the experiments with the maximum fit error among twenty-seven main experiments and eight confirmation experiments in separate columns. The initial fit including all data points resulted in a poor fit with 53% maximum error. In order to improve the accuracy of the fit, it has been decided to exclude outliers from the fit selectively. A systematic approach has been adapted by excluding each run combination one by one and repeating the curve fit to identify the best fit providing the minimum error for all the experiments. After identifying the outlier experiments that provide the fittest improvement, the combinations of these experiments have been excluded to achieve a better fit. Four outlier experiments are identified as combinations numbered 3, 6, 17, and 20. These four outlier experiments are gradually excluded from the derivation of the closed-form equation. For the cases labeled as “one outlier excluded”, each one of the identified outlier experiments is excluded from the equation fit process systematically one at a time. Four different equations have been derived for each case. Calculated leakage rates using these equations are compared with the experimental data from both all main experiments and confirmation experiments. The closed-form equation, where outlier combination #17 is excluded from the fit, yielded the lowest “max error” when compared to the leakage data from the main experiments. However, this error was still too high with the rate of 45%. On the other hand, the closed-form equation, where outlier combination #3 is excluded from the fit, yielded the lowest “max error” when compared to the leakage data from the confirmation experiments. Again, this error was also very high with the rate of 38%.

Therefore, it has been decided to proceed with the selective outlier exclusion process by conducting exclusions two at a time, then three at a time, and all four at once.

The selective outlier exclusion forming the equation fit process indicates that maximum error decreases when higher number of outliers are excluded. The lowest error has been achieved where all four outlier combinations are excluded from the equation fit process. The resulting equation ends up with leakage estimates with maximum 20% error when compared to each of all main experiments and confirmation experiments. Therefore, the final closed-form equation is selected by excluding experiments # 3, 6, 17, and 20 from the fit process. The final model fits the data with 95%  $R^2$  value and with 90% adjusted  $R^2$  value.

Case	Outlier No(s) (from Main Experiments)	Max Error % (Main Experiments)	Max Error % (Confirmation Experiments)
Without Outlier	-	53	53
One Outlier Excluded	3	56	38
	6	55	49
	17	45	41
	20	53	53
Two Outliers Excluded	3,6	58	26
	3,17	33	40
	3,20	43	50
	6,17	35	29
	6,20	30	37
Three Outliers Excluded	17,20	47	43
	3,6,17	35	33
	3,6,20	39	44
	3,17,20	36	38
Four Outliers Excluded	6,17,20	39	33
	3,6,17,20	20	20

**Table 6.6: Leakage rate error between experiments and closed-form equation.**

The final closed-form equation defining the relationship between the strong parameters and normalized leakage rate is presented as:

$$\text{Normalized Leakage} = -65.98 + 1.454 \text{ SD} + 3.349 \text{ CW} + 0.01393 \text{ PD} + 9.9 \text{ OF} + 0.0083 \text{ SD}^2 - 0.0132 \text{ CW}^2 + 0.000003 \text{ PD}^2 + 4.92 \text{ OF}^2 - 0.0797 \text{ SD} \cdot \text{CW} - 0.000114 \text{ SD} \cdot \text{PD} - 0.195 \text{ SD} \cdot \text{OF} - 0.000417 \text{ CW} \cdot \text{PD} - 0.205 \text{ CW} \cdot \text{OF} - 0.00785 \text{ PD} \cdot \text{OF} \quad (6.3)$$

Calculated leakage rates are compared with the test data from eight confirmation experiments and tabulated in Table 6.7. There is no observed correlation between error rate and levels of the parameters. However, the error can be as high as 20% for the estimates of the derived equation. In order to understand whether fit accuracy deteriorates further for other design combinations, it has been decided to use more test data. Therefore, additional eight experiments other than the previously tested combinations (twenty-seven main experiments and eight first confirmation experiments performed earlier) have been conducted. The results of the second confirmation runs are presented in Table 6.8. As the results indicate that all of the error levels are also below 20% in the second run of confirmation experiments. More than half of the experiments have less than 10% error as presented in Table 6.8.

Exp. No.	SD [mm]	CW [mm]	GP [mm]	ST [mm]	SR [μm]	PD [kPad]	OF [mm]	MI [°]	Norm. Leak. (Eq.)	Norm. Leak. (Exp.)	Error
1	32	22	4	0.254	6.4	206.8	0.1	0	0.3869	0.3306	15%
2	32	24	4	0.254	6.4	206.8	0.2	0	0.4155	0.3339	19%
3	32	24	4	0.254	6.4	344.7	0.1	0	0.7139	0.6651	7%
4	34	22	4	0.254	6.4	344.7	0.1	0	1.0388	1.1325	9%
5	34	26	4	0.254	6.4	344.7	0.1	0	0.4042	0.4850	20%
6	34	22	4	0.254	6.4	206.8	0.2	0	0.6588	0.5273	20%
7	34	24	4	0.254	6.4	206.8	0.1	0	0.6481	0.6007	7%
8	36	24	4	0.254	6.4	206.8	0	0	1.1235	1.0195	9%

**Table 6.7: Leakage rate error between confirmation experiments and closed-form equation**

Exp. No.	SD [mm]	CW [mm]	GP [mm]	ST [mm]	SR [μm]	PD [kPad]	OF [mm]	MI [°]	Norm. Leak. (Eq.)	Norm. Leak. (Exp.)	Error
1	32	22	4	0.254	6.4	482.6	0.1	0	1.0464	1.0196	3%
2	32	24	4	0.254	6.4	482.6	0.2	0	0.6285	0.6654	6%
3	34	24	4	0.254	6.4	344.7	0.2	0	0.4863	0.5188	7%
4	34	26	4	0.254	6.4	482.6	0	0	1.0652	0.9064	15%
5	34	22	4	0.254	6.4	482.6	0.2	0	1.0389	0.9112	12%
6	34	24	4	0.254	6.4	482.6	0.1	0	1.0147	0.9193	9%
7	36	24	4	0.254	6.4	482.6	0	0	1.6437	1.7629	7%
8	36	24	4	0.254	6.4	482.6	0.2	0	0.6748	0.7511	11%

**Table 6.8: Leakage rate error between additional confirmation experiments and closed-form equation**

Figure 6.8 illustrates the variation trend of the normalized leakage rate with respect to four strong parameters. The parameters show nonlinear behaviors that cannot be detected in two-level screening experiments. It is also observed during screening experiments that leakage flow becomes higher with an increase in slot depth and leakage rate decreases with an increase in cloth width. As expected, leakage increases with a higher pressure drop.

All trends obtained from main experiments are compatible with the ‘Effect Plot’ of screening experiments in Figure 6.3.

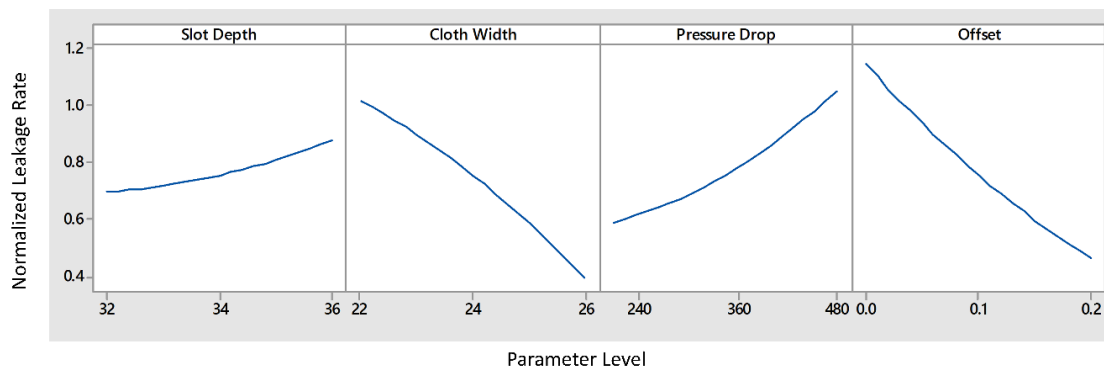


**Figure 6.8: The effect plots for normalized leakage rate (Box-Behnken designs with four outliers)**

In the literature [9], [10], the leakage rate is usually constant or increasing with offset&mismatch conditions. In this study, leakage rate is decreasing with a higher offset level. The trend function of offset parameter is convex. Therefore, this trend may diminish or even reverse for higher offset levels.

## 7 CONCLUSION

Gas turbines are demanded to operate with more efficient sealing. Cloth seals provide a good alternative to metal shim seals to reduce leakage rate and increase wear life.

A test setup is used to calculate the leakage rate of cloth weave in warp, shute, diagonal, and out-of-plane directions. Test results are matched with CFD analysis to obtain flow resistance coefficients in warp, shute, diagonal, and out-of-plane directions. Cloth seal CFD analyses are conducted with calibrated resistance coefficients. The leakage rates in CFD analyses are matched with cloth seal tests by calibrating operating clearances. The CFD models with calibrated resistance coefficients and operating clearances are analyzed in turbine operating conditions. This methodology provides an estimation of the leakage performance of cloth seals in turbine operating conditions.

The leakage performance of the cloth seal is correlated with operating conditions and geometric parameters. In this thesis, geometric parameters and pressure load of the cloth seal are investigated in terms of sealing performance. Another experimental test setup is established to measure leakage rate through cloth seals with various geometric dimensions under varying pressure load. A design of experiments (DoE) study is performed to understand the influence of cloth seal parameters on leakage performance. A closed-form equation is derived based on the leakage results of experimental designs.

Some outlines are explained in the following subsections.

### 7.1 Cloth Weave

Cloth weave leakage tests are carried out at four weave directions of warp, shute, diagonal, and cross. Flow resistance coefficients for flow within the porous cloth weave are calculated and calibrated by using the Sutherland-ideal gas approach. A CFD model is built for four weave directions and analyses are run to determine the best set of flow resistance coefficients. All these works are performed for Dutch twill type cloth weave with 30x250 weave density per inch. The conclusions for the cloth weave study are summarized below.

**Leakage tests:**

Leakage tests show that cloth weave leakage is a linear function of pressure load for all directions.

The best-worst order of leakage performance in terms of normalized equivalent gap has occurred in the order of warp, diagonal, shute and cross directions.

Out-of-plane direction has the highest normalized equivalent gap, therefore, it is the worst direction in terms of leakage performance. Normalized equivalent gap for cross direction is 2-4 times higher than in-plane directions (warp, shute, diagonal).

As a result, leakage rate is minimum if the flow is in the warp direction. Leakage test results point out that, for the best sealing practices, the cloth weave in cloth seal geometry should be aligned in such a way that flow direction would be in the warp direction. The weave alignment depends on the engine location and working conditions that dictate the flow over the cloth seal.

**Cloth weave flow resistance coefficients:**

In order to determine the cloth weave flow resistance coefficients that match with test leakage, cloth weave CFD models are built for each direction of warp, shute, diagonal, and cross. For each direction, CFD analyses are performed with weave flow resistance coefficients calculated by using Sutherland-ideal gas approach and test data.

Flow resistance coefficients depend on evaluation of pressure level that changes over the weave flow thickness. This is represented with pressure constant ( $C_{down}$ ). Therefore, CFD analyses are repeated for a range of pressure constant  $C_{down}=0.5-1.0$  for in-plane directions and  $C_{down}=0.0-1.0$  for cross direction with 0.1 increments to determine the best leakage match with test data.

For warp and shute directions, the best match between test and CFD leakages is obtained for  $C_{down}=0.9$  at which leakage difference between test and CFD is less than 10% for all pressure loads of  $\Delta P=137.9-689.5$  kPad (20-100 psid).

For diagonal direction,  $C_{down}=0.7$  gives the minimum leakage difference of 10%.

For cross direction,  $C_{\text{down}}=0.0$  provides the best leakage agreement with tests yielding 0.03% difference.

Thus, the best  $C_{\text{down}}$  values are listed below:

- warp: 0.9
- shute: 0.9
- diagonal: 0.7
- cross: 0.0

### **Flow behavior:**

Flow formations within the weave are visualized by plotting pressure and velocity fields. The pressure gradually drops over the weave thickness. The pressure variation with the weave thickness is well represented with a polynomial function at least in the second order. Most of the pressure drop occurs at the downstream side.

The flow property plots show that the flow was smoothly directed through the region of metallic-cloth fibers from the upstream side for the in-plane directions. The flow velocity reached its maximum value at the downstream side due to expansion.

## **7.2 Cloth Seal**

In this study, CFD analyses of cloth seal design have been performed in both test and turbine conditions for baseline and offset positions. The effect of geometric parameters under varying pressure load on the cloth seal leakage performance has been investigated. An experimental test setup has been established to measure leakage rate through cloth seals with various geometric dimensions under varying pressure load. Some outlines are presented below.

### **Cloth seal CFD analyses:**

After calibrating flow resistance coefficients for different directions and pressure load, cloth seal CFD analyses are conducted in test conditions. The operating clearance is changed iteratively to match leakage rate of test and CFD analysis. CFD models are analyzed in turbine operating conditions with calibrated resistance coefficients and

operating clearances. Such a systematic approach provides a methodology to estimate leakage performance of cloth seals in turbine operating conditions.

### **Screening experiments:**

Eighteen parameters have been identified in terms of wear, compliancy, leakage, and structural performance. Based on general industrial practice and typical operational range, ten of these parameters have been set at the levels in order to reduce the problem size. The remaining eight parameters have been selected for further study through screening experiments. Sixteen combinations have been tested following two-level Resolution IV fractional factorial experiment design.

In the cloth seal design stages, it is important to determine the seal leakage performance depending on design parameters. The results show that pressure drop, cloth width, slot depth, and relative offset position of mating slot surfaces are determined as strong parameters with the highest influence on cloth seal leakage rate. These parameters need to be carefully determined in order to improve leakage performance. The results show that increasing cloth width and reducing slot depth are the most effective way to reduce leakage flow rate apart from reducing pressure drop. Shim thickness has the lowest impact. On average, experiments with  $\Delta P = 482.6$  kPa (70 psi) have two-fold leakage rates in comparison to experiments under  $\Delta P = 206.8$  kPa (30 psi) pressure load. Leakage increase is observed with a higher slot depth between lateral surfaces of the slot. When all other parameters are the same, higher slot depth experiments have a higher distance between lateral surface and shim tab as well. 36 mm slot depth experiments have higher leakage rates compared to 32 mm slot depth experiments. Small cloth width and large sealing gap between adjacent slots reduce seal seating surface area; therefore, flow is exposed to less resistance. It has been observed that leakage performance improves with a 0.2 mm offset in comparison to no offset condition.

Surface roughness, gap, mismatch position of mating surfaces, and shim thickness have been identified to have relatively less impact on leakage rate of cloth seals. Leakage rate increases with mismatch condition. Higher shim thickness causing higher stiffness raises leakage rate slightly. Rough surfaces are considered to promote better cloth interlocking at the mating surface resulting in slightly better sealing efficiency.

The observed equivalent gap performance rates provide a similar trend with experimental data published in the literature [9], [10]. For baseline condition experiments, the normalized equivalent gap remains almost constant with respect to different pressure drop levels. For offset and mismatch condition experiments, a slight decrease in normalized equivalent gap occurs with increasing pressure drop. This may be an indication of slight shape change and slot conformance under more pressure due to the flexible nature of the cloth seals. For screening experiments, the experiment with minimum flow rate has 86% lower leakage rate than the experiment with maximum flow rate. This result explains that geometric dimensions and pressure can significantly affect leakage rate through the cloth seal.

### **Main and confirmation experiments:**

Four strong parameters are selected for the detailed investigation and used in the main experiments. Once the experiments have been conducted and a representative equation has been fit based on the main experiment results, four experiments have been identified as outliers. These four outlier combinations have been excluded during a final closed-form equation fit. The resulting equation predicts leakage rates with maximum 20% error when compared to main experiment tests and sixteen different confirmation experiments all of which have different parameter combinations than the main experiments. The observed effect trends of the parameters in the main experiments are compatible with the results of screening experiments. Through the use of multilevel main experiment design, nonlinear trends between parameters and leakage rates are also detected. As a result of this, although leakage performance becomes better with an increase in offset level, this benefit may diminish and even disappear with an extreme offset level.

### **7.3 Contributions**

The contributions of this thesis are important in estimating cloth seal leakage performance and designing cloth seals. The contributions and conclusions are summarized in the following items.

- **Analytical Studies**
  - Cloth seal flow resistance coefficients have been expressed in non-Darcian porous model.
  - Sutherland-ideal gas approach has been developed for calibrating flow resistance coefficients. With this approach, the leakage difference between the test and CFD is less than 10% for all pressure loads of Dutch twill cloth weave.
  - A porosity calculation method has been developed for plain and twill woven fibers.
- **Cloth Seal Manufacturing and Test Rig Designs**
  - Cloth weave has been selected as Dutch Twill (30x250 mesh density) and ordered.
  - Several cloth seal designs have been manufactured after cutting, bending, welding and final cutting processes.
  - Two different test systems have been designed and established for cloth weave tests. In-plane cloth weave test system has been established for leakage tests of warp, shute and diagonal directions. Out-of-plane test setup has been designed for leakage tests of out-of-plane direction.
  - Cloth seal leakage test rig has been designed and set up to measure leakage rate through cloth seal at various geometric dimensions and pressure load.
- **CFD Analyses and Correlation with Tests**
  - Several analytical approaches have been developed to determine a relation between pressure drop and leakage as a function of effective parameters, especially pressure and temperature level, fluid properties, and porous medium geometry. Sutherland-ideal gas approach provides the best correlation with test results.
  - Depending on the value of  $C_{down}$ , the inertial/viscous flow resistance coefficients are calculated by using Sutherland-ideal gas approach and test data for each direction of warp, shute, diagonal, and cross.
  - For warp and shute directions, the best match between test and CFD leakages is obtained for  $C_{down}=0.9$  at which leakage difference between test and CFD is less than 10% for all pressure loads of  $\Delta P=137.9-689.5$  kPad (20-100 psid).
  - For diagonal direction,  $C_{down}=0.7$  gives the minimum leakage difference of 10%.

- For cross direction,  $C_{down}=0.0$  provides the best leakage agreement with tests yielding 0.03% difference
  - Reynolds Averaged Navier-Stokes equations for k- $\epsilon$  turbulence model are conducted with CFD analysis. Porous medium approach with derived porosity equation is added to RANS k-  $\epsilon$  equations in order to solve cloth weave region.
  - CFD analyses and test results of cloth weave have been successfully conducted with close leakage rate values.
  - Porous medium approach has been successfully applied in CFD models.
  - Pressure contours, velocity magnitude, streamlines, and vectors have been illustrated for warp, shute, diagonal, and out-of-plane directions.
  - Cloth seal CFD analyses are conducted with leakage test results to calculate operating clearance. Then, the performance of the cloth seal is illustrated in turbine operating conditions.
- **Design Optimization Based on Experiments**
    - Eighteen candidate parameters that may affect the leakage performance have been detected. In order to reduce the problem to a manageable size, some of the candidate parameters have been fixed based on literature data and industrial experience.
    - Screening experiment designs have been performed to investigate the effect of adjacent cavity distance, cloth seal length, gap, shim thickness, surface roughness, pressure. The screening experiment study has been conducted with Fractional Factorial designs.
    - As a new knowledge, the trend of leakage performance with respect to eight parameters has been illustrated with Pareto chart and Main effect plot.
    - Screening experiment results show that slot distance, cloth width, pressure drop, and offset have a strong impact on leakage performance of cloth seal at specified operating conditions. Therefore, these parameters have been selected for the main experiment design study.
    - The main experiment study has been conducted with Box-Behnken designs. Twenty-seven experiments have been completed to obtain a closed-form equation. Sixteen confirmation experiments have been performed to compare the leakage rate obtained from experiments and calculated by closed-form equation. The differences have been shown as leakage rate error.

- A systematic approach has been adapted by excluding each run combination one by one and repeating the curve fit to identify the best fit providing the minimum error for all the experiments. After identifying the outlier experiments that provide the most fit improvement, the combinations of these experiments have been excluded to achieve a better fit. The leakage rate error has been obtained less than %20 for all cases.
- For main experiments, pareto chart plot has been illustrated to show nonlinear trends between parameters and leakage rate.
- All trends obtained from main experiments are compatible with the results of screening experiments.
- Leakage rate is decreasing with a higher offset level. This result conflicts with previous knowledge. In main experiments, the trend function of offset parameter is convex, In order to understand the trend of leakage rate with respect to higher offset levels, a set of experiments are conducted. The experimental result shows that this trend is diminish or even reverse for extreme offset levels. To obtain minimum leakage rate, an equation is derived to determine optimum offset level with respect to strong parameters.
- Screening Exp. #1 which provides the best leakage result in baseline condition, has a leakage rate approximately 62% less than the baseline rigid seal. The experiment with 0.3 mm offset level gives best leakage results in all tested cloth seal designs. It provides approximately %81 better than rigid seal leakage performance.

#### **7.4 Future Work**

In this study, the flow behaviors of cloth weave and cloth seal are investigated with theoretical models, experiments and CFD analyses. Further studies need to be conducted to answer the questions.

The porous medium approach for metallic-cloth fibers represents a good correlation when the flow resistance coefficients are calibrated. Further improvements are needed to investigate and correlate the flow resistance coefficients as a function of weave geometry (warp diameter, shute diameter, and weave density) by performing additional tests and analyses. One limitation of this study is that the test rig was not designed to

change the operating temperature. In addition, the flow resistance coefficients of the cloth weave can be calibrated with respect to the porosity and length of the weave by using Ergun's equation [55] if the equivalent spherical diameter is determined.

A fully coupled solution of flow and structural equations are a challenge for cloth seal due to the complex structure and slot positions.

Cloth seal CFD analyses provide the leakage rate in turbine operating conditions with calibrated flow resistance coefficients and operating clearance. In order to obtain the increase of overall power output with cloth seal application, a system-level analysis of the gas turbine needs to be performed. Several pressure and temperature measurements and geometric dimensions are required from a gas turbine for a system-level analysis.

## 8 REFERENCES

- [1] Dogu, Y., Aksit, M.F., Bagepalli, B., Burns, J., Sexton, B., Kellock, I., “Thermal and flow analysis of cloth-seal in slot for gas turbine shroud applications”, 34th AIAA/ASME/SAE/ASEE Joint Propulsion Conference and Exhibit, Cleveland, OH, U.S.A, (1998).
- [2] Duran, E.T., “Stiffness and Friction Characterization of Brush Seals”, Thesis Project for Doctor of Philosophy, Sabanci University, Istanbul, (2013).
- [3] Aksit, M.F., Bagepalli, B.S., Aslam, S., “High Performance Combustor Cloth Seals”, 36th AIAA/ASME/SAE/ASEE Joint Propulsion Conference & Exhibit, July 2000, AL, U.S.A.
- [4] Pastrana, M.R., Wolfe, C.E., Turnquis, N.A. and Burnett, M.E., “Improved Steam Turbine Leakage Control with a Brush Seal Design”, Proceedings of the 30th Turbomachinery Symposium, 33-38, (2001).
- [5] Turnquist, N., Chupp, R., Baily, F., Burnett, M., Rivas, F., Bowsher, A. and Crudgington, P., “Brush Seals for Improved Steam Turbine Performance”, NASA Seals Workshop, NASA/CP-2006-214383/VOL1, 107-127, (2006).
- [6] Aksit M.F., “Seeking Design Solutions Through Decoupling Problems – A Global Engineering Example”, ME Today, ASME International, Online Journal, Academic/Industry Perspectives, Vol.11, March issue (2010).
- [7] Dinc, O.S., B.S. Bagepalli, C. Wolfe, M.F. Aksit, and S. Calabrese, “A New Metal Cloth Stationary Seal for Gas Turbine Applications,” Proc. 33rd AIAA/ASME/SAE/ASEE Joint Propulsion Conference, Seattle, Washington, AIAA Paper 97-2732, (1997).
- [8] Chupp, R.E., Hendricks, R.C., Lattime S.B., Steinetz, B.M., “Sealing in Turbomachinery”, NASA/TM-2006-214341, Cleveland, Ohio, USA, (2006).

- [9] Aksit, M.F., Bagepalli, B.S., Demiroglu, M., Dinc, O.S., Kellock, I., Farrell, T., “Advanced Flexible Seals for Gas Turbine Shroud Applications”, 35th AIAA/ASME/SAE/ASEE Joint Propulsion Conference & Exhibit, June 1999, CA, U.S.A.
- [10] Aksit, M.F, Bagepalli, B.S., Burns, J., Stevens, P., Vehr, J., “Parasitic Corner Leakage Reduction in Gas Turbine Nozzle-Shroud Inter-Segment Locations”, 37th AIAA/ASME/SAE/ASEE Joint Propulsion Conference & Exhibit, July 2001, Utah, U.S.A.
- [11] Chupp, R.E, Hendricks, R.C., Lattime, S.B., Steinetz, B.M., Aksit, M.F., “Turbomachinery Clearance Control. Turbine Aerodynamics, Heat Transfer, Materials, and Mechanics”, Turbine Aerodynamics, Heat Transfer, Materials, and Mechanics; AIAA: VA, USA, pp. 61–188, (2007).
- [12] Patent No: US6599089 B2, “Supplemental Seal for the Chordal Hinge Seal in a Gas Turbine”.
- [13][https://www.haynesintl.com/alloys/alloy-portfolio\\_/High-temperature-Alloys/haynes-25-alloy/principle-features](https://www.haynesintl.com/alloys/alloy-portfolio_/High-temperature-Alloys/haynes-25-alloy/principle-features)
- [14] Patent No: US8613451 B2, “Cloth Seal for Turbo-machinery”.
- [15] Patent No: US 8696309 B2, “Brazed Turbine Seal”.
- [16] R. Ongun, M. F. Aksit, and G. Goktug, “A simple Model for Wear of Metal Cloth Seals”, presented at 40th AIAA/SAE/ASME/ASEE Joint Propulsion Conference & Exhibit, AIAA-2004-3892, Fort Lauderdale, Florida, (2004).
- [17] Archard, J.F., “Contact and Rubbing of Flat Surfaces,” J. Applied Phys., 24. (8), pp. 981, (1953).
- [18] Archard, J.F. and Hirst, W., “The Wear of Metals Under Unlubricated Conditions”, Proc. Roy. Soc., 236, 397-410, (1956).

- [19] Amaki, K., T. Hasegawa and T. Narumi; “Drag Reduction in the Flow of Aqueous Solutions of Detergent Through Mesh Screens,” *Nihon Reoroji Gakkaishi*, 36, 125–131, (2008).
- [20] Osaka, H., H. Yamada, S. Hano and Y. Kageyama; “Fluid Flow through Plain Square Screens,” *Trans. Jpn. Soc. Mech. Eng. (B)*, 52, 312–317, (1986).
- [21] Takahashi, Y.; “Pressure Drop Coefficient of Screens,” *Research Report of Takamatsu National College of Technology*, 16, 25–33, (1980).
- [22] Wiegardt, K. E. G.; “On the Resistance of Screens,” *Aeronaut. Q.*, 4, 186–192, (1953).
- [23] Kolodziej, A. and J. Lojewska; “Experimental and Modelling Study on Flow Resistance of Wire Gauzes,” *Chem. Eng. Process.*, 48, 816–822, (2009).
- [24] Patent No: US8118549, “Gas Turbine Transition Duct Apparatus”.
- [25] Patent No: US7901186, “Seal Assembly”.
- [26] Patent No: US8684673 B2, “Static Seal for Turbine Engine”.
- [27] Patent No: US4537024, “Turbine Engines”.
- [28] Patent No: US5975844, “Sealing Element for Sealing a Gap and Gas Turbine Plant”.
- [29] Patent No: US5125796, “Transition Piece Seal Spring for a Gas Turbine”.
- [30] Patent No: US 5154577, “Flexible Three-Piece Seal Assembly”.
- [31] Patent No: US5934687, “Gas-Path Leakage Seal for a Turbine”.
- [32] Patent No: US6733234, “Biased Wear Resistant Turbine Seal Assembly”.
- [33] Patent No: US8398090, “Spring Loaded Seal Assembly for Turbines”.
- [34] Patent No: US8678754, “Assembly for Preventing Fluid Flow”.

[35] Patent No: US9188228 B2, "Layered Seal for Turbomachinery".

[36] Patent No: US5657998, "Gas Path Leakage Seal for a Gas Turbine".

[37] Patent No: US5509669, "Gas-path Leakage Seal for a Gas Turbine".

[38] Patent No: US5586773, "Gas-path Leakage Seal for a Gas Turbine Made from Metallic Mesh".

[39] Patent No: US6547256 B2, "Cloth Ring Seal".

[40] Patent No: US6609886 B2, "Composite Tubular Woven Seal for Gas Turbine Nozzle and Shroud Interface".

[41] Patent No: US6655913 B2, "Composite Tubular Woven Seal for An Inner Compressor Discharge Case".

[42] Patent No: US7389991 B2, "Leakage Seal for Gas Path of Gas Turbine".

[43] Patent No: US 2004/0013522 A1, "Endface Gap Sealing of Steam Turbine Packing Seal Segments and Retrofitting Thereof".

[44] Patent No: US 2014/0062034 A1, "Gas Path Leakage Seal for a Turbine".

[45] Patent No: EP 0 903 519 A1, "Flexible Cloth Seal Assembly".

[46] Patent No: US 6547257 B2, "Combination Transition Piece Floating Cloth Seal and Stage 1 Turbine Nozzle Sealing Element".

[47] Patent No: US 6203025 B1 "Seal".

[48] Patent No: US 2013/0115048 A1, "Convolution Seal for Transition Duct in Turbine System".

[49] Patent No: US 2003/0039542 A1, "Transition Piece Side Sealing Element and Turbine Assembly Containing Such Seal".

- [50] Patent No: US 6502825 B2, "Pressure Activated Cloth Seal".
- [51] Dogu, Y., 2003, "Investigation of Brush Seal Flow Characteristics Using Bulk Porous Medium Approach," ASME Paper No. GT-2003-38970, (2003).
- [52] ANSYS. ANSYS CFX-Solver Theory Guide, Version 14; ANSYS: Canonsburg, PA, USA, (2011).
- [53] <https://thesteveportal.plm.automation.siemens.com/>
- [54] Sutherland, W., "The viscosity of gases and molecular force", *Philosophical Magazine*, S. 5, 36, pp. 507-531, (1893).
- [55] Ergun, S., "Fluid flow through packed columns" *Chem. Eng. Prog.*, 48, (1952)
- [56] Akgiray, O., Saatci, A. M., "A New Look at Filter Backwash Hydraulics", *Water Science and Technology: Water Supply*, Vol:1, Issue:2, pp.65-72, (2001).
- [57] Wu, W. T., J. F. Liu, W. J. Li and W. H. Hsieh; "Measurement and Correlation of Hydraulic Resistance of Flow through Woven Metal Screens," *Int. J. Heat Mass Transfer*, 48, 3008–3017, (2005)
- [58] Yamamoto, H., R. Utsumi and A. Kushida; "Aperture Size in a Screen of Plain Dutch Weaves," *Kagaku Kogaku Ronbunshu*, 12, 635–639, (1986)
- [59] Kobayashi, T., J. Mitani and Y. Ishikawa; "A Proposal of a Calculation Tool for Filtration Performance of Dutch Weave", *Trans. Jpn. Soc. Mech. Eng. (A)*, 78, 179–189, (2012)
- [60] Yoshida, Y., Inoue, Y., Shimosaka, A., Shirakawa, Y., Hidaka, J., "Effect of Aperture Structure of Dutch Weave Mesh on Flow Resistivity", *Journal of Chemical Engineering of Japan*, Vol. 48, No. 9, pp. 730–741, (2015).
- [61] Yu, B.M., Li, J.-H., "A geometry model for tortuosity of flow path in porous media." *Chin. Phys. Lett.* 21:1569–1571, (2004).

- [62] Lanfrey, P. Y., Kuzeljevic, Z.V., Dudukovic M.P., “Tortuosity model for fixed beds randomly packed with identical particles”, Chem. Eng. Sci. 65:1891–1896, (2010).
- [63] Armour, J. C., Cannon, J.N., “Fluid Flow Through Woven Screens”, AIChE Journal, Vol 14, No.3, (1968).
- [64] Crudginton, P.F. “Brush Seal Performance Evaluation”, In Proceedings of the 34th AIAA/ASME/SAE/ASEE Joint Propulsion Conference and Exhibit, Cleveland, OH, USA, 13–15 July 1998.
- [65] Chen, L. H., Wood, P. E., Jones, T. V., and Chew, J. W., “An Iterative CFD and Mechanical Brush Seal Model and Comparison with Experimental Results,” ASME paper no. 98-GT-372, (1998).
- [66] <https://engineersfield.com/preload-force-ad-tightening-torque/>
- [67] <https://www.enggyclopedia.com/2011/09/air-compressibility-factor-table/>
- [68] Aksit, M.F., Chupp, R.E., Dinc, O.S., Demiroglu, M., “Advanced Seals for Industrial Turbine Applications: Design Approach and Static Seal Development”, Journal of Propulsion and Power, Vol 18, No.6, (2002).

## APPENDIX A: CLOTH SEAL GEOMETRIC GAP VS PRESSURE RATIO

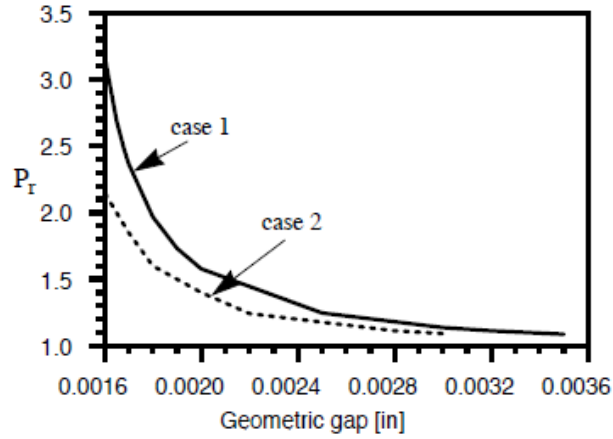


Figure A.1: Change of cloth seal operating clearance versus pressure ratio [1]

## APPENDIX B: PRELOAD FORCE AND TIGHTENING TORQUE

Dimensions	Preload force			Tightening torque		
	$F_v$			$M_A$		
	N			Nm		
	8.8	10.9	12.9	8.8	10.9	12.9
<b>Coarse pitch thread</b>						
M4	3750	5 500	6 450	3.2	4.7	5.5
M5	6 100	9000	10 500	6.4	9.3	11
M6	8 650	12700	14 800	11	16	19
M8	15 900	23 300	27 300	27	39	46
M10	25 300	37 100	43 400	53	78	91
M22	36 800	54 000	63 500	92	135	155
M14	55 500	74 500	87 000	145	215	250
M16	69 500	102 000	120 000	230	335	390
M18	87 500	124 000	145 000	325	465	540
M20	112 000	160 000	187 000	460	660	770
M22	140 000	200 000	234 000	620	890	1050
M24	162 000	230 000	269 000	790	1150	1300
M27	213 000	303 000	355 000	1150	1650	1950
M30	259 000	369 000	431 000	1600	2250	2650
<b>Fine pitch thread</b>						
M8*1	17 400	25 600	29 900	29	43	50
M10*1.25	27 200	40 000	46 800	56	83	97
M12*1.25	41 600	61 000	71 500	100	150	175
M12*1.5	39 200	57 500	67 500	96	140	165
M16*1.5	56 000	82 500	96 500	160	235	275
	76 000	112 000	131 000	245	360	425
M18*1.5	102 000	163 000	171 000	370	530	620
M20*1.5	129 000	206 000	216 000	520	740	860
M22*1.5	159 000	253 000	266 000	690	990	1150

Figure B.1: Preload force and tightening torque for hexagon head screws [66]

## APPENDIX C: COMPRESSIBILITY FACTORS FOR AIR

Temp, K	Pressure, bar (absolute)						
	1	5	10	20	40	60	80
75	0.0052	0.0260	0.0519	0.1036	0.2063	0.3082	0.4094
80		0.0250	0.0499	0.0995	0.1981	0.2958	0.3927
90	0.9764	0.0236	0.0453	0.0940	0.1866	0.2781	0.3686
100	0.9797	0.8872	0.0453	0.0900	0.1782	0.2635	0.3498
120	0.9880	0.9373	0.8860	0.6730	0.1778	0.2557	0.3371
140	0.9927	0.9614	0.9205	0.8297	0.5856	0.3313	0.3737
160	0.9951	0.9748	0.9489	0.8954	0.7803	0.6603	0.5696
180	0.9967	0.9832	0.9660	0.9314	0.8625	0.7977	0.7432
200	0.9978	0.9886	0.9767	0.9539	0.9100	0.8701	0.8374
250	0.9992	0.9957	0.9911	0.9822	0.9671	0.9549	0.9463
300	0.9999	0.9987	0.9974	0.9950	0.9917	0.9901	0.9903
350	1.0000	1.0002	1.0004	1.0014	1.0038	1.0075	1.0121
400	1.0002	1.0012	1.0025	1.0046	1.0100	1.0159	1.0229
450	1.0003	1.0016	1.0034	1.0063	1.0133	1.0210	1.0287
500	1.0003	1.0020	1.0034	1.0074	1.0151	1.0234	1.0323
600	1.0004	1.0022	1.0039	1.0081	1.0164	1.0253	1.0340
800	1.0004	1.0020	1.0038	1.0077	1.0157	1.0240	1.0321

**Figure C.1: Compressibility factors for air at different temperature and pressure conditions [67]**

APPENDIX D: GAS TURBINE SYSTEM LEVEL SECONDARY  
FLOW/PERFORMANCE ANALYSIS

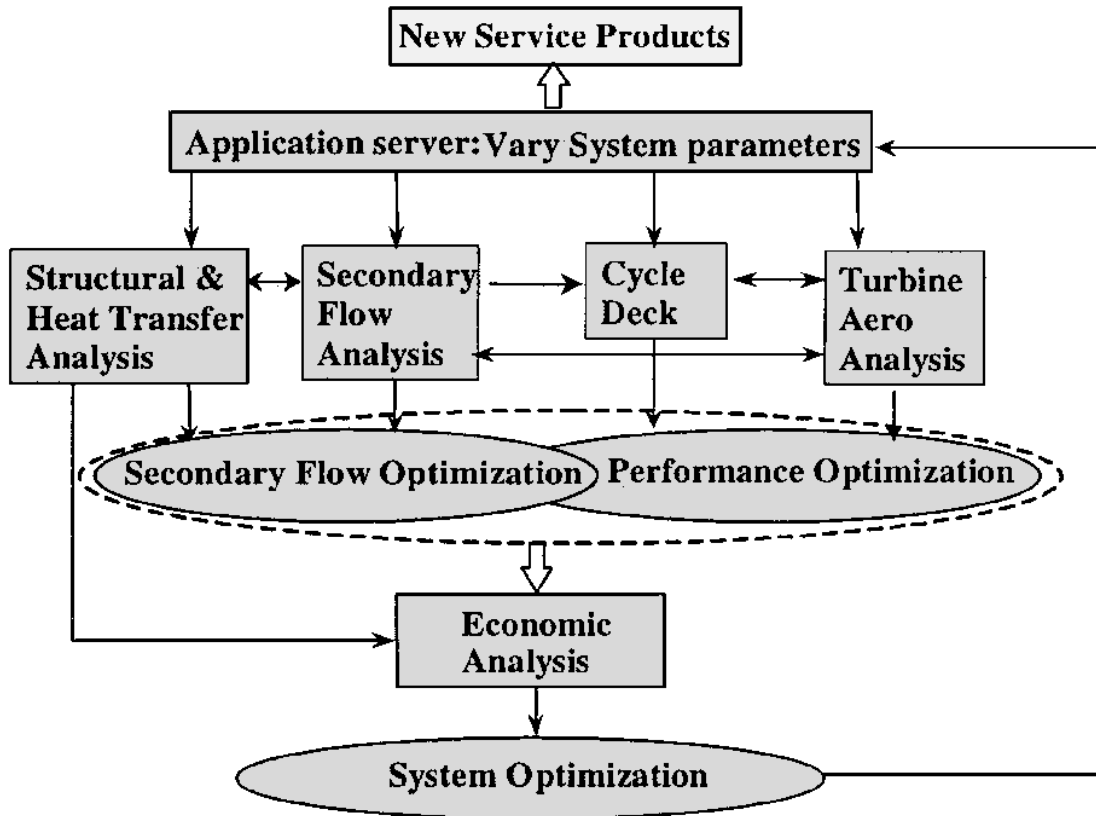


Figure D.1: Gas-turbine system-level assessment of design mods. [68]